Large-eddy simulation of the atmospheric boundary layer: Influence of unsteady forcing, baroclinicity, inversion strength and stability on the wind profile

Pedersen, Jesper Grønnegaard

Publication date:
2013

Document Version
Publisher's PDF, also known as Version of record

Large-eddy simulation of the atmospheric boundary layer: Influence of unsteady forcing, baroclinicity, inversion strength and stability on the wind profile

Jesper Grønnegaard Pedersen
DTU Wind Energy PhD-0032 (EN)
November 2013

DTU Wind Energy
Department of Wind Energy

Author: Jesper Grønnegaard Pedersen
Title: Large-eddy simulation of the atmospheric boundary layer: Influence of unsteady forcing, baroclinicity, inversion strength and stability on the wind profile
Department: Department of Wind Energy

Abstract:
The largest wind turbines today often reach heights where traditional models of the wind speed and how it varies with height no longer can be expected to apply. For accurate assessment of wind energy resources and loads on wind turbines, there is a need for better understanding of the flow of air above the atmospheric surface layer. Continuous and detailed measurements of mean winds and turbulence above the surface layer are expensive and difficult to obtain. Computational fluid dynamics modelling of the atmospheric flow can be an attractive alternative or supplement to field experiments.
In this study, the method of large-eddy simulation (LES) is applied to gain improved insight on the flow in the atmospheric boundary layer (ABL). The primary motivation behind the study has been to facilitate improvement of analytical wind profile models valid above the surface layer, however, the prospect of using LES more directly in applications such as short-term forecasting of the turbulent flow at e.g. wind farm sites is also considered.
Two case studies based on measurements from the rural site of Høvsøre, Denmark and a suburban site in Hamburg, Germany demonstrate the need for accurate specification of the large-scale pressure forcing, when using LES for prediction of real-world wind profiles. In the Høvsøre case study, simulated wind speeds agree well with measurements throughout the ABL, but only when the applied forcing follows a height- and time-dependent pressure gradient estimated from continuous LIDAR measurements of the wind speed above the ABL. Including unsteadiness and baroclinic effects in the forcing also improves agreement with measurements in the Hamburg case study, but not as unambiguously as in the Høvsøre case study. It is concluded that the measurements available at and around the site in Hamburg are insufficient for accurate estimation of the driving pressure gradient, and that phenomena such as large-scale subsidence and advection also should be included in the LES for accurate wind profile prediction.
A range of simulations of more idealized conditions are performed to study the influence of the free atmosphere Brunt Vaisala frequency and baroclinicity on the development and steady-state structure of neutral and near-neutral ABLs. It is found that an adjustment time of at least 16 hours is needed for the simulated flow to reach a quasi-steady state. The highly idealized conditions facilitate the formation of a super-geostrophic jet near the top of the ABL. It is considered to be a rare phenomena in the real-world ABL, and is not accounted for by the analytical models of the wind shear included in this study. It is furthermore shown that the considered wind profile model can be improved by appropriately accounting for the wind shear due to the free atmosphere Brunt Vaisala frequency and baroclinicity.

The thesis is submitted to the Danish Technical University in partial fulfilment of the requirements for the PhD degree.

2013

Project Period:
14.10.2010 – 14.11.2013

Degree:
PhD

Field:
Wind Energy

Supervisors:
Sven-Erik Gryning
Mark Kelly

Sponsorship:
Danish Research Agency
Strategic Research Council
Sagsnummer 2104-08-0025
"Tall wind" project

Frontpage:
Photo from Kalveboderne in Copenhagen, courtesy of Peter Bo Forsberg.

Pages: 81 (including appendices)
Tables: 1
References: 49

Technical University of Denmark
DTU Wind Energy
Nils Koppels Allé
Building 403
2800 Kgs. Lyngby

www.vindenergi.dtu.dk

DANISH ABSTRACT (DANSK RESUMÉ)

De største vindmøller i dag når ofte højder, hvor traditionelle modeller for vindhastigheden og dens højdeafhængighed ikke længere kan forventes at gælde. Nøjagtig vurdering af vindenergi-ressourcer og belastninger på vindmøller kræver bedre forståelse af vinden over luftlaget nærmest jordoverfladen (overfladelaget). Kontinuerlige og detaljerede målinger af middelvind og turbulens i sådanne højder er bekostelige og vanskelige at udføre. Computer-simulering af atmosfæriske luftstrømme kan være et attraktivt alternativ eller supplement til virkelige fuldskala eksperimenter.
Metoden "large eddy simulation" (LES) bruges her til at opnå en bedre forståelse af luftstrømmen i det atmosfæriske grænselag. Den primære motivation er at muliggøre forbedring af eksisterende modeller for vindhastigheden over overfladelaget. Den potentielle brug af LES direkte i forbindelse med eksempelvis forudsigelse på kort sigt af vind og turbulens i og omkring vindmølleparker bliver imidlertid også taget i betragtning.
To simuleringseksempler baseret på målinger fra et fladt landbrugsområde ved Høvsøre i Danmark og et bebygget område uden for den centrale del af Hamborg i Tyskland viser nødvendigheden af nøjagtig specifikation af den trykgradient, der driver vinden, når LES bruges til forudsigelse af vindprofiler i den virkelige verden. Høvsøre-eksemplet viser god overensstemmelse mellem simulerede og målte vindhastigheder gennem hele det atmosfæriske grænselag, men kun når den påførte kraft følger en højde- og tidsafhængig trykgradient bestemt på grundlag af kontinuerlige LIDAR målinger af vindhastigheden over det atmosfæriske grænselag. Inkludering af trykgradientens tidsafhængighed og baroklinitet (udtryk for en horisontal temperaturgradient) forbedrer også overensstemmelsen mellem målinger og simulering i Hamborg-eksemplet, men ikke ligeså entydigt som i Høvsøre-eksemplet. Det konkluderes at de tilgængelige målinger ikke er tilstrækkelige til nøjagtig bestemmelse af trykgradienten, og at fænomener så som synkende luftmasser og stor-skala advektion også bør inkluderes i simuleringer, hvor målet er at opnå overensstemmelse med målte vindprofiler.
En række simuleringer af i højere grad idealiserede forhold er blevet udført med henblik på at undersøge indflydelsen af Brunt Vaisala frekvensen (udtryk for en vertikal temperaturgradient) i den fri atmosfære og baroklinitet på udviklingen og ligevægtstilstanden af neutrale og nær-neutrale atmosfæriske grænselag. En justeringstid på mindst 16 timer findes nødvendig for at opnå en tilnærmelsesvis ligevægtstilstand. De meget idealiserede forhold tillader udviklingen af et lag nær toppen af det atmosfæriske grænselag, hvori vindhastigheden overstiger hastigheden af geostrofvinden. Dette antages at være et sjældent fænomen i den virkelige verden, og der bliver ikke taget højde for det i de modeller af vindhastighedens vertikale gradient, som er inkluderet i denne undersøgelse. Det vises at den vindprofil-model, som indgår i undersøgelsen, kan forbedres ved på passende vis at inkludere den højdeafhængighed af vinden som stammer fra Brunt Vaisala frekvensen i den fri atmosfære og baroklinitet.

Contents

ACKNOWLEDGEMENTS

First and foremost, I would like to thank Sven-Erik Gryning and Mark Kelly for their dedicated support and guidance. I feel very fortunate to have had the chance to work with two such competent, enthusiastic and helpful supervisors.
I would also like to thank Ekaterina Batchvarova for her contribution to the project and Branko Kosović for hosting a very enjoyable stay at NCAR from which I learned a lot.
Thanks to everyone at DTU Wind Energy for making it an inspiring and pleasant place to work. A special thanks goes to my fellow PhD students for their good company and for always being ready to help.
Finally, I would like to express my deepest gratitude to my parents and my sister for their encouragement, care and support.

1

INTRODUCTION

Accurate knowledge about mean wind speed and turbulence is essential for assessment of wind energy resources and loads on wind turbines. The aim of the study presented here is to improve understanding of the flow of air in the atmospheric boundary layer (ABL) through use of computational fluid dynamics (CFD), with specific focus on how the wind speed changes with height above the surface layer. Results from large-eddy simulation (LES) of the ABL are analysed and compared to tower-based measurements, LIDAR data, and analytical models.

In recent years human-induced climate change has increased interest in renewable sources of energy. In 2011 the share of renewable energy in the gross final energy consumption across the European Union (EU) reached 13%, and the member states have a agreed upon a mandatory target of 20% by 2020 (Eurostat, 2013). Wind energy is expected to play an important role in the pursuit of this target, and 26.5% of the total power capacity installations in the EU during 2012 was accounted for by wind power (EWEA, 2013). Worldwide there was a growth in the installed wind power capacity of about 19% (GWEC, 2013).

The production capacity of a wind turbine increases with the swept area of its blades, and larger wind turbines tend to be more cost-effective than smaller ones. Today the largest wind turbines have a capacity of approximately 7 MW and rotor diameters of approximately 150 m. When installed, the hub and the upper half of the rotor will often reach heights where well-established models of the near-surface wind speed based on Monin-Obukhov (MO) similarity (e.g. Businger et al., 1971; Dyer, 1974) no longer can be expected to apply. Future wind turbines will most likely extend even higher into the atmosphere, hence the need for a better understanding of the flow above the surface layer.

CFD modelling allows us to simulate and study the flow in the ABL in a controlled "environment" providing information not easily obtained from field experiments. With complete control of the parameters influencing the flow, the effect of changing one or more of these can readily be observed. Furthermore, the often high cost of performing field experiments is avoided.

Continuous measurements of mean wind speed and turbulence at high altitudes are expensive due to the need of erecting tall meteorological masts. Modern remote sensing LIDAR systems can, under favourable conditions, provide accurate wind speed measurements up to a few kilometres (Floors et al., 2013); but the instruments are still expensive, and second-order moments (turbulence) are generally underestimated due to the spatial

averaging implicit in the measuring method (Sathe et al., 2011). Thus with the power of modern computer clusters making way for high-accuracy ABL simulations, CFD modelling is seen as an attractive supplement to field measurements. LES in particular has the potential to provide highly detailed information about the unsteady turbulent flow of the ABL.
This thesis is based on two papers on the topic of LES of the ABL. The first of these is a study of the ability of the applied LES code to predict real-world wind profiles:

I "The effect of unsteady and baroclinic forcing on predicted wind profiles in Large Eddy Simulations: Two case studies of the daytime atmospheric boundary layer". Accepted for publication in Meteorologische Zeitschrift.

The second of the two papers is aimed at improved understanding of the structure of neutral and near-neutral ABLs, especially the upper part, through use of LES:

II "On the structure and development of inversion-capped neutral atmospheric boundary layers: A large-eddy simulation study".
Submitted to Boundary-Layer Meteorology.

Additional details regarding paper I and paper II are provided in chapter 3. Chapter 2 provides a general introduction to the ABL and models used to describe it (analytical and numerical). General conclusions are given in chapter 4. The two papers are attached as appendices.

2

BACKGROUND

2.1 The atmospheric boundary layer

The ABL is the lowest part of the atmosphere where the flow of air is directly influenced by the surface of the Earth. Its top – often defined as the height where the flow ceases to be turbulent – can vary between tens of meters to a few kilometres, depending among other factors on atmospheric stability. Figure 2.1 shows wind speeds from a large-eddy simulation of the flow over a flat homogeneous surface with a small positive heat flux. The boundary layer extending up to approximately 800 m in this case, is characterized by highly varying wind speeds and is clearly distinguished from the free atmosphere above where the flow is much more uniform. Details about the simulation are provided in Paper II, in which it is referred to as simulation n_{07}.

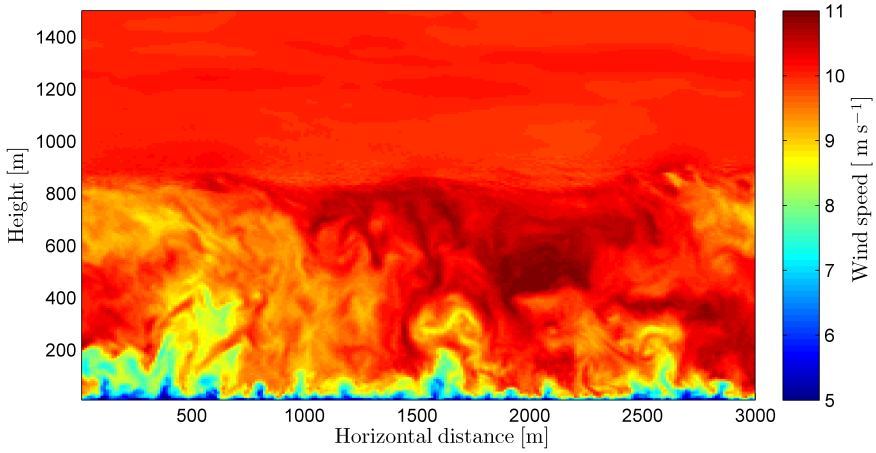

Figure 2.1: Wind speeds from an LES of the flow over a flat homogeneous surface.

The ABL height is often subject to large diurnal variation, especially over land. During the day solar radiation heats the surface of the Earth and both buoyancy and mean wind shear contribute to the production of turbulent kinetic energy (TKE) (Batchvarova and Gryning, 1991). This leads to a relatively deep ABL – potentially extending up to a few kilometres in the afternoon where it reaches its maximum height (Stull, 2009). Around

sunset buoyant production of TKE ceases, the daytime ABL collapses and a shallower ABL characterized by turbulence generated by wind shear develops. Surface cooling and the associated buoyant destruction of TKE typically inhibits the growth of the night-time ABL.

Traditional stability classification of ABLs is based on the sign of the surface heat flux (Zilitinkevich et al., 2012), and the terms "neutral", "stable" and "unstable" refer to ABLs with zero, negative (downwards) and positive (upwards) surface heat fluxes. Zilitinkevich and Esau (2005) pointed out that this surface-based classification is often insufficient and proposed new definitions which also account for the stability of the air above the ABL. In this new framework the neutral ABL can be classified as either truly neutral (TN) or conventionally neutral (CN), and the stable ABL as either nocturnal or long-lived. In the case of TN and nocturnally stable conditions, the potential temperature above the ABL is constant with height (i.e. neutrally stratified), whereas the CN and the long-lived stable ABL borders directly on a stably-stratified free atmosphere characterized by a potential temperature increasing with height.

As the name implies, nocturnally stable conditions are characteristic of the night-time ABL, which develops beneath the typically neutrally stratified residual layer (i.e. the remains of the daytime ABL). Long-lived stable and conventionally neutral conditions are most likely to occur over oceans and in polar regions, where there is generally less diurnal variation of the surface heat flux than over land and outside the polar regions. However, since the surface heat flux is rarely exactly zero, strictly CN and TN conditions cannot be expected to occur very often. Paper II includes a further discussion on this issue in terms of LES.

The mean horizontal flow of air in the ABL is to a first approximation driven by pressure gradients associated with synoptic-scale high- and low-pressure systems, i.e. flow structures with length scales on the order of 1000 km (Holton, 1992). More locally however, meso-scale phenomena such as sea breezes, caused by pressure variations over distances on the order of 10-100 km (Stull, 2009) can become dominant. Paper I describes (i) how the pressure gradient driving the ABL flow can be estimated from various types of measurements, and (ii) the effect on the predicted wind speed of applying a realistic time- and height-dependent driving pressure gradient in LES of the daytime ABL.

As the air moves over the surface of the Earth, the imposed drag tends to decrease the near-surface velocity. Analytical models for determining the associated vertical gradient of the velocity, i.e. the wind shear, are described in section 2.2. Knowledge of how the wind speed changes with height is often required for wind energy resource assessment, primarily because wind speed measurements at the hub-height of modern wind turbines are rarely available and extrapolation from measurements closer to the surface is needed.

2.2 Analytical models of the wind profile

In the surface layer (typically the lowest ∼10% of the ABL) the dimensionless wind shear is well-described by MO similarity, i.e. as a function (ϕ) of just z/L:

$$\frac{\partial |\mathbf{u}|}{\partial z} \frac{z\kappa}{u_{*0}} = \phi(z/L), \tag{2.1}$$

where $|\mathbf{u}|$ is the mean wind speed, z is the height above the surface, u_{*0} is the surface friction velocity representing the surface shear stress and κ is the von Karman constant. L is the Obukhov length reflecting the stability of the surface layer:

$$L = -\frac{u_{*0}^3}{\kappa(g/T)\left\langle w'\theta' \right\rangle_s}, \tag{2.2}$$

where g is acceleration due to gravity, T is the temperature of the air near the surface and $\left\langle w'\theta' \right\rangle_s$ is the surface heat flux. In neutral conditions (both TN and CN), $L^{-1} = 0$ and $\phi = 1$, and integration of equation 2.1 yields the logarithmic "law-of-the-wall" wind profile. Based on surface layer measurements, Businger et al. (1971), Dyer (1974) and Carl et al. (1973) presented now widely accepted functional forms of the ϕ-function for both stable $(L > 0)$ and unstable conditions $(L < 0)$. In non-neutral (diabatic) conditions integration of equation 2.1 (Paulson, 1970) leads to the logarithmic wind profile plus a stability correction (Ψ) depending on z/L:

$$|\mathbf{u}| = \frac{u_{*0}}{\kappa}\left[\ln\left(\frac{z}{z_0}\right) + \Psi(z/L)\right], \tag{2.3}$$

where z_0 is the roughness length of the surface.
Using data from a 213 m meteorological tower at Cabauw in the Netherlands, Holtslag (1984) found good agreement between equation 2.3 (using the Businger-Dyer relationships (Businger et al., 1971; Dyer, 1974)) and measured wind profiles, in unstable conditions up to 200 m and in moderately stable conditions up to 100 m. In neutral/near-neutral conditions equation 2.3 seems to overestimate the wind speed above 80 m. More recently Gryning et al. (2007) confirmed the applicability of equation 2.3 up to 50-80 m based on measurements from Høvsøre, Denmark and Hamburg, Germany, but found it to be inaccurate above. A new model aimed to be valid throughout the entire ABL was proposed based on a relationship between the wind shear, the local friction velocity u_* and a local length scale l:

$$\frac{\partial |\mathbf{u}|}{\partial z} = \frac{u_*}{\kappa l}. \tag{2.4}$$

The length scale (equivalent to the mixing-length of Prandtl, 1925), is modelled through inverse summation of length scales representative of the surface layer (L_{SL}), the middle

part of the ABL (L_{MBL}) and the upper ABL (L_{UBL}):

$$\frac{1}{l} = \frac{1}{L_{SL}} + \frac{1}{L_{MBL}} + \frac{S}{L_{UBL}}, \tag{2.5}$$

with $S = 1$ implicit in the original formulation.
The surface layer length scale is in neutral conditions given by $L_{SL} = z$, while a stability correction following Carl et al. (1973) is included in diabatic conditions. The length scale of the middle ABL does not depend on z, but is rather a function of parameters such as baroclinic shear and the Brunt-Vaisala frequency (Gryning et al., 2007). In the proposed model, the value of L_{MBL} is determined to make the wind speed match the geostrophic wind speed $|\mathbf{G}|$ at the top of the ABL, i.e. at $z = h$. Models for determining $|\mathbf{G}|$ and the boundary layer height h are described below.
Assuming that the top of the ABL acts as lid limiting the size of the turbulent motions, Gryning et al. (2007) use $L_{UBL} = h - z$ (following Rossby and Montgomery, 1935). Kelly and Gryning (2010) let S represent the dimensionless baroclinic shear, i.e.

$$S = \kappa h \frac{\mathrm{d}|\mathbf{G}|/\mathrm{d}z}{u_{*0}}. \tag{2.6}$$

The local friction velocity u_* is assumed to decrease linearly with height throughout the ABL.With these assumptions, equation 2.4 can easily be integrated to give an expression for the wind speed as a function of height.
The geostrophic wind speed and thereby the value of L_{MBL} is often an unknown quantity, and Gryning et al. (2007) suggest to use the geostrophic drag law (Blackadar and Tennekes, 1968) for determining it:

$$\frac{|\mathbf{G}|}{u_{*0}} = \frac{1}{\kappa}\left(\left[\ln\left(\frac{u_{*0}}{f z_0}\right) - A\right]^2 + B^2\right)^{0.5}. \tag{2.7}$$

A and B are functions of the stability parameter $\mu = u_{*0}(fL)^{-1}$, and f is the Coriolis parameter. Zilitinkevich and Esau (2005) furthermore argued that A and B should depend on h and the Brunt-Vaisala frequency $N = \left(\frac{\partial\theta}{\partial z}\frac{g}{\theta}\right)^{0.5}$ above the ABL, and proposed new functional forms to include these parameters.
In truly neutral conditions the boundary layer height can be estimated as a function of the Coriolis parameter and the surface friction velocity (Rossby and Montgomery, 1935):

$$h = c_h u_{*0} f^{-1}, \tag{2.8}$$

where c_h is a dimensionless parameter often assumed to be a constant around 0.1. However, as pointed out by e.g. Zilitinkevich and Esau (2002) and Zilitinkevich et al. (2012), in conventionally neutral conditions c_h should be a function of the free atmosphere Brunt

Vaisala frequency. Stably stratified air above the ABL tends to suppress turbulence and inhibit growth of the ABL. This is discussed further in Paper II, which also includes a comparison between LES results and the wind-profile model of Gryning et al. (2007) and the wind shear model proposed in Zilitinkevich and Esau (2005).

The surface layer is generally better understood than the rest of the ABL, partly because it is easier to obtain measurements near the surface than at higher altitudes (Wyngaard, 2010). However, high-accuracy numerical modelling and remote-sensing measuring techniques (Floors et al., 2013) are providing information for improved understanding of the flow above the surface layer. The following sections introduce numerical modelling of atmospheric flows and the concept of LES used in the wind profile studies of Paper I and Paper II.

2.3 CFD modelling of the ABL

Computational fluid dynamics (CFD) modelling covers a range of numerical methods for simulating fluid flows and for solving flow-related problems. The starting point is filtered or averaged versions of the Navier-Stokes equations, i.e. equations for conservation of momentum, to which approximate solutions are found over discrete intervals and sampled at discrete points in space and time. The distance between adjacent points or the width of the applied filter is referred to as the resolution of the model.
CFD simulation of atmospheric flows is challenging, in particular due to the wide range of spatial and temporal scales of motion interacting. These include synoptic-scale weather systems characterized by variations in the flow over thousands of kilometres and temporal scales on the order of weeks at one end of the spectrum to turbulent eddies a few millimetres in size and with temporal scales on the order of seconds at the other. With the computational resources available today it is not meaningful to perform numerical simulations which cover the largest flow structures and at the same time resolve the smallest scales. Thus, it is common practice to leave the smallest scales unresolved and use a subfilter-scale (SFS) model to account for their influence on the resolved flow. This method is applied in e.g. meso-scale simulations used for regional weather forecasts, and in research-orientated micro-scale simulations such as the large-eddy simulations presented in Paper I and Paper II. A main difference between the two types of simulations is the range of scales left unresolved. The spatial resolution of meso-scale simulations is in most cases on the order of 1 km or more in the horizontal directions and no turbulence is resolved by the model, whereas the resolution in LES is $\sim$30 m or less and the part of the turbulence accounting for most of the kinetic energy is resolved (Wyngaard, 2004). A more detailed introduction to LES, and in particular the code used in the present study is given in section 2.4.
In both types of simulations (meso- and micro-scale), the computational domain is typically smaller than the largest structures of the actual flow (i.e. synoptic- and possibly

meso-scale structures). In such cases the influence of these is normally included through boundary conditions or simply neglected. The latter option can be justified if the simulation period is short and the domain sufficiently small compared to the temporal and spatial scales of the neglected variations in the flow.
Methods such as LES and in particular direct numerical simulation (DNS) which requires even finer resolution (down to the Kolmogorov microscale), are expensive in terms of computational resources. However, due to their potentially high accuracy they can be used in the development of less expensive analytical or numerical models (e.g. Zilitinkevich and Esau, 2005; Brown et al., 2006). One objective of the LES study presented in Paper II is improvement of existing analytical models of the wind profile by inclusion of the influence of the temperature gradient above the ABL.

2.4 The NCAR LES code

The purpose of this section is to outline the concept of LES and to introduce the NCAR LES code (based on Moeng, 1984; Sullivan et al., 1994; Sullivan and Patton, 2011) used in this thesis.

2.4.1 Governing equations

The starting point is the equations for conservation of momentum and potential temperature in a Cartesian coordinate system moving with the Earth:

$$\frac{\partial u_i}{\partial t} + \frac{\partial u_j u_i}{\partial x_j} = \underbrace{-\frac{1}{\rho}\frac{\partial p}{\partial x_i}}_{\text{I}} \underbrace{+\varepsilon_{ij3} 2\Omega \sin(\varphi) u_j}_{\text{II}} \underbrace{+\varepsilon_{ij2} 2\Omega \cos(\varphi) u_j}_{\text{III}} \underbrace{- g\delta_{i3}}_{\text{IV}} \underbrace{+\nu \frac{\partial^2 u_i}{\partial x_j \partial x_j}}_{\text{V}} \quad (2.9)$$

and

$$\frac{\partial \theta}{\partial t} + u_i \frac{\partial \theta}{\partial x_i} = \gamma_\theta \frac{\partial^2 \theta}{\partial x_i \partial x_i}. \quad (2.10)$$

Equations 2.9 and 2.10 are written using index notation, where repeated indices indicate summation and $i, j = 1, 2$ or 3. The eastward, northward and upward (normal to the assumed flat surface of the Earth) directions are denoted by $(x_1, x_2, x_3) = (x, y, z)$ and the corresponding velocity components by $(u_1, u_2, u_3) = (u, v, w)$. The horizontal average of w is kept to zero at all times in the NCAR LES code. Time is represented by t, air density by ρ and pressure by p. Ω denotes the angular speed of rotation of the Earth, ε_{ijk} is the Levi-Civita symbol (alternating tensor), φ is the latitude, g is acceleration due to gravity, δ_{ij} is the Kronecker delta and ν is the kinematic viscosity of the air. The potential temperature θ is treated as a conserved scalar, and γ_θ represents the thermal diffusivity.

Equation 2.9 relates the total acceleration of the flow (left-hand side) to the forces acting on the flow, i.e. forces due to a pressure gradient (term I), the Coriolis effect (terms II and III), gravity (term IV) and viscous drag (term V). Term III is generally small compared to the other terms, and is often neglected which leads to:

$$\frac{\partial u_i}{\partial t} + \frac{\partial u_j u_i}{\partial x_j} = -\frac{1}{\rho}\frac{\partial p}{\partial x_i} + \varepsilon_{ij3} f u_j - g\delta_{i3} + \nu \frac{\partial^2 u_i}{\partial x_j \partial x_j} \tag{2.11}$$

with the Coriolis parameter $f = 2\Omega\sin(\varphi)$. Furthermore, by splitting the potential temperature and the density into mean and fluctuating parts ($\theta = \langle\theta\rangle + \theta'$ and $\rho = \langle\rho\rangle + \rho'$), the pressure into a mean, a fluctuating and a base state part ($p = \langle p\rangle + p' + p_0$), applying the Boussinesq approximation and assuming the mean state of the flow to be in hydrostatic balance, equation 2.11 can be written as:

$$\frac{\partial u_i}{\partial t} + \frac{\partial u_j u_i}{\partial x_j} = -\frac{1}{\langle\rho\rangle}\left(\frac{\partial p'}{\partial x_i} + \frac{\partial p_0}{\partial x_i}\right) + \varepsilon_{ij3} f u_j + g\delta_{i3}\frac{\theta'}{\langle\theta\rangle} + \nu\frac{\partial^2 u_i}{\partial x_j \partial x_j}, \tag{2.12}$$

where square brackets denote a horizontal average. In the NCAR LES code, the base state pressure p_0 varies linearly in x and y and is constant in z. The horizontal gradient $\left(\frac{\partial p_0}{\partial x}, \frac{\partial p_0}{\partial y}\right)$ is specified as an external forcing in terms of

$$\mathbf{G} = (U_g, V_g) = \left(-\frac{1}{f\langle\rho\rangle}\frac{\partial p_0}{\partial y}, \frac{1}{f\langle\rho\rangle}\frac{\partial p_0}{\partial x}\right), \tag{2.13}$$

which may be set to vary in time and height for simulation of unsteady and baroclinic conditions (as in Paper I). The vertical gradient of p_0 introduced by assuming baroclinic conditions (i.e. $\frac{\partial \mathbf{G}}{\partial z} \neq 0$) is small and can be neglected.
A filter is defined with the purpose of removing high-wavenumber fluctuations from the flow. It divides the flow variables into filtered (resolved) and high-wavenumber subfilter-scale (SFS) parts, e.g. $u_i = \overline{u_i} + u_i^{\mathrm{SFS}}$ and $\theta = \overline{\theta} + \theta^{\mathrm{SFS}}$. Overbars indicate filtered quantities. Applying the filter to equations 2.12 and 2.10 leads to:

$$\frac{\partial \overline{u_i}}{\partial t} + \frac{\partial \overline{u_j}\,\overline{u_i}}{\partial x_j} = -\frac{1}{\langle\rho\rangle}\left(\frac{\partial \overline{p'}}{\partial x_i} + \frac{\partial p_0}{\partial x_i}\right) + \varepsilon_{ij3} f \overline{u_j} + g\delta_{i3}\frac{\overline{\theta'}}{\langle\theta\rangle} - \frac{\partial \tau_{ij}}{\partial x_j} \tag{2.14}$$

and

$$\frac{\partial \overline{\theta}}{\partial t} + \overline{u_i}\frac{\partial \overline{\theta}}{\partial x_i} = -\frac{\partial \tau_{\theta i}}{\partial x_i}, \tag{2.15}$$

where

$$\tau_{ij} = \overline{u_i u_j} - \overline{u_i}\,\overline{u_j} \tag{2.16}$$

and

$$\tau_{\theta i} = \overline{\theta u_i} - \overline{\theta}\,\overline{u_i} \tag{2.17}$$

represent SFS fluxes of momentum and heat. Mean and base state quantities pass unchanged through the filter. The viscous drag term is neglected assuming that the scales of the filtered motions are much larger than the range of scales where viscous effects are significant.

In the NCAR code, the advection term of equation 2.14 is written in rotational form to ensure conservation of the volume-averaged kinetic energy (Moeng, 1984), and the SFS stress is divided into a mean normal stress $\tau^n = \frac{1}{3}\left(\overline{u_k u_k} - \overline{u_k}\,\overline{u_k}\right)$ and the deviatoric stress tensor $\tau^d_{ij} = \overline{u_i u_j} - \overline{u_i}\,\overline{u_j} - \delta_{ij}\tau^n$. The mean normal stress is included in the "pseudo"-pressure variable P^* together with the fluctuating pressure p' and the resolved kinetic energy $\frac{1}{2}\overline{u_i}\,\overline{u_i}$:

$$P^* = \frac{\overline{p'}}{\langle\rho\rangle} + \tau^n + \frac{1}{2}\overline{u_i}\,\overline{u_i} \tag{2.18}$$

This leads to:

$$\frac{\partial \overline{u_i}}{\partial t} + \varepsilon_{ijk}\overline{\omega_j}\,\overline{u_k} = -\frac{\partial P^*}{\partial x_i} - \frac{1}{\langle\rho\rangle}\frac{\partial p_0}{\partial x_i} + \varepsilon_{ij3} f \overline{u_j} + g\frac{\overline{\theta'}}{\langle\theta\rangle}\delta_{i3} - \frac{\partial \tau^d_{ij}}{\partial x_j}, \tag{2.19}$$

where $\omega_i = \varepsilon_{ijk}\frac{\partial u_k}{\partial x_j}$ is the vorticity.

Equations 2.15 and 2.19 are solved in a computational domain with the side lengths L_x, L_y and L_z and with N_x, N_y and N_z grid points in each of the three directions. The spatial discretization of the LES domain acts in practice as a filter on the flow variables; the shortest wavelength which can be resolved in a given direction is two times the grid spacing in that direction (Pope, 2000). This type of implied filtering is used in the vertical direction in the NCAR code (Moeng, 1984). In the horizontal directions a sharp spectral filter is applied, i.e. the flow fields are Fourier transformed and the Fourier components of wavenumbers above a specified limit are set to zero. For filtering in the x- and y-directions, the cut-off limits are given by $1/\Delta_x$ and $1/\Delta_y$. To avoid aliasing the effective grid spacings Δ_x and Δ_y are defined by $\frac{3}{2}\frac{L_x}{N_x}$ and $\frac{3}{2}\frac{L_y}{N_y}$ (Orszag, 1971). The cut-off limits and $\frac{1}{\Delta_z} = \frac{N_z}{L_z}$ should preferably be within the inertial subrange of the turbulent energy spectrum, ensuring that the most energy-containing turbulent eddies are resolved. Turbulent fluctuations within the inertial subrange are assumed to be isotropic and of universal character (Sullivan et al., 1994). These characteristics make them more suitable for a general parametrization than turbulence in the energy containing range which to a larger extent is influenced by the mean flow and the surrounding environment.

After filtering, the fields are transformed back to physical space and the simulation is moved forward to the next time step. Each time step consists of three stages following the third-order Runge Kutta integration method described by Sullivan et al. (1996).

Centred finite differencing of second order accuracy is used for determining all vertical gradients, except $\frac{\partial \overline{\theta}\,\overline{w}}{\partial z}$ which is determined using the $k = \frac{1}{3}$-scheme of Koren (1993). To facilitate this, the grid is vertically staggered with the vertical velocity w and the SFS

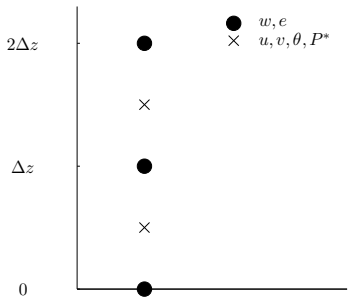

Figure 2.2: Staggered grid of the NCAR LES code.

TKE $e = \frac{3}{2}\tau^n$ defined at grid points shifted half a vertical grid spacing relative to the grid points at which u, v, θ and P^* are defined (see figure 2.2). Horizontal derivatives are calculated in spectral space (Moeng, 1984).
By taking the divergence of equation 2.19 and applying continuity $\frac{\partial u_i}{\partial x_i} = 0$, a Poisson equation for P^* is formed. It is solved using the method described in Sullivan et al. (1996).

2.4.2 Subfilter-scale model

The SFS fluxes of momentum τ_{ij}^d and heat $\tau_{\theta i}$ are unknown quantities which have to be parametrized. A common method is to relate them to gradients of the resolved fields through an eddy viscosity (ν_t) and an eddy diffusivity (ν_θ):

$$\tau_{ij}^d = -2\nu_t S_{ij} \tag{2.20}$$

and

$$\tau_{\theta i} = -\nu_\theta \frac{\partial \overline{\theta}}{\partial x_i}, \tag{2.21}$$

where $S_{ij} = \frac{1}{2}\left(\frac{\partial \overline{u_i}}{\partial x_j} + \frac{\partial \overline{u_j}}{\partial x_i}\right)$ is the strain rate tensor of the resolved flow. The SFS model of the NCAR LES code is based on the model of Deardorff (1980) in which the eddy viscosity of equation 2.20 is given by

$$\nu_t = C_k l e^{1/2}. \tag{2.22}$$

C_k is a constant and l is a characteristic length scale of the SFS fluctuations. For unstable and neutral stratification (i.e. for $\frac{\partial \overline{\theta}}{\partial z} \leq 0$) the length scale is based on the effective grid spacings:

$$l = \left(\Delta_x \Delta_y \Delta_z\right)^{1/3}. \tag{2.23}$$

In the case of stable stratification ($\frac{\partial \overline{\theta}}{\partial z} > 0$), the characteristic length scale of the unresolved turbulence could potentially become smaller than the effective grid spacing (Deardorff, 1980), and the following reduced length scale is used:

$$l = 0.76 e^{1/2} \left(\frac{g}{\theta_0} \frac{\partial \overline{\theta}}{\partial z} \right)^{-1/2}. \tag{2.24}$$

The SFS TKE is calculated through its own prognostic equation (Moeng, 1984):

$$\frac{\partial e}{\partial t} + u_i \frac{\partial e}{\partial x_i} = -\tau_{ij}^d S_{ij} + \frac{g}{\langle \theta \rangle} \tau_{\theta 3} + \frac{\partial}{\partial x_i} \left(2\nu_t \frac{\partial e}{\partial x_i} \right) - \varepsilon \tag{2.25}$$

in which the dissipation ε is modelled as:

$$\varepsilon = C_\varepsilon \frac{e^{3/2}}{l} \tag{2.26}$$

where C_ε is a constant. Finally, the eddy diffusivity of equation 2.21 is given by:

$$\nu_\theta = \left(1 + 2l \left(\Delta_x \Delta_y \Delta_z \right)^{-1/3} \right) \nu_t. \tag{2.27}$$

With these assumptions and appropriate boundary conditions, equations 2.19 and 2.15 can be solved numerically. However, as shown by e.g. Sullivan et al. (1994) results obtained with the described SFS model agrees poorly with MO similarity (e.g. equation 2.1). Near the surface, the size of the energy-containing turbulent eddies scale with z, and they inevitably become unresolved. This means that the SFS model has to account for a wider range of turbulence than it was designed for, including turbulence which is not necessarily isotropic. To alleviate this problem, Sullivan et al. (1994) proposed a modifiation to the model of Deardorff (1980) which includes the effect of the mean wind shear on the SFS turbulence:

$$\tau_{ij}^d = -2\nu_t \gamma S_{ij} - 2\nu_T \left\langle S_{ij} \right\rangle, \tag{2.28}$$

where γ is an isotropy factor, and ν_T is an eddy viscosity based on the horizontally averaged strain rate $\left\langle S_{ij} \right\rangle$ and a requirement for the mean wind speed to match MO similarity at $z = \Delta_z$. The isotropy factor is defined in such a way that it becomes small near the surface where the mean strain rate is large, and approaches unity away from the surface where ν_T is set to zero. The modified equation for τ_{ij}^d is followed by a change in the shear production term of the SFS TKE equation (2.25) which is then given by:

$$\frac{\partial e}{\partial t} + u_i \frac{\partial e}{\partial x_i} = 2\nu_t \gamma \left(S_{ij} - \left\langle S_{ij} \right\rangle \right) \left(S_{ij} - \left\langle S_{ij} \right\rangle \right) + \frac{g}{\langle \theta \rangle} \tau_{\theta 3} + \frac{\partial}{\partial x_i} \left(2\nu_t \frac{\partial e}{\partial x_i} \right) - \varepsilon. \tag{2.29}$$

Sullivan et al. (1994) showed that the proposed model (equation 2.28) gives better agreement with MO similarity than the baseline model (equation 2.20) throughout the surface

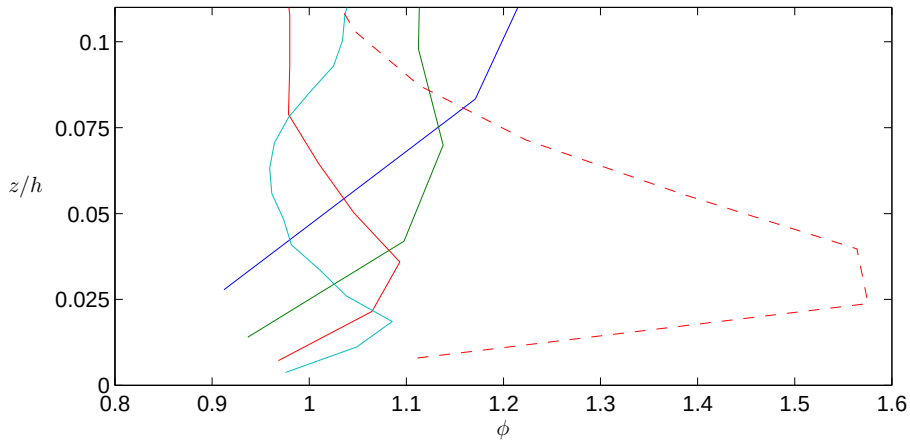

Figure 2.3: Profiles of dimensionless wind shear ϕ from simulations of the conventionally neutral ABL employing the SFS model of Sullivan et al. (1994) (solid lines) and the SFS model of Deardorff (1980) (dashed line). Blue, green, red and cyan lines represent simulations with 64^3, 128^3, 256^3, 512^3 grid points.

layer. The same is illustrated in figure 2.3, which shows profiles of the dimensionless wind shear in the surface layer from simulations of the conventionally neutral ABL employing the SFS model of Sullivan et al. (1994) (solid lines) and the SFS model of Deardorff (1980) (dashed line). Blue, green, red and cyan lines represent simulations with 64^3, 128^3, 256^3, 512^3 grid points. More detailed information about the simulations are provided in Paper II. The simulated dimensionless wind shear is generally too high near the surface compared to MO similarity with $\phi = 1$. The "overshoot" is however much more pronounced in the simulation using the SFS model of Deardorff (1980) than any of the simulations using the the SFS model of Sullivan et al. (1994). Increasing the number of grid points decreases the overshoot and moves it closer to the surface, as also described by Brasseur and Wei (2010).

2.4.3 Boundary conditions

With the spectral method used in the NCAR LES code for calculating horizontal derivatives, there is no need to explicitly specify boundary conditions at the side walls of the computational domain; periodicity is implied.

At the lower boundary, i.e. at $z = 0$, a surface roughness length z_0 and a horizontal-average surface heat flux $\langle w'\theta' \rangle_s$ are specified to account for the interaction between the surface of the Earth and the flow above. All three velocity components are set to

zero, and a surface friction velocity u_{*0} is determined through MO similarity, the surface roughness and the horizontally averaged wind speed $|\mathbf{u}_1| = \left(u_1^2 + v_1^2\right)^{1/2}$ at $z = z_1 = \Delta z/2$. Following Moeng (1984), the local vertical SFS surface momentum fluxes are given by:

$$\tau_{xz0} = -u_{*0}^2 \frac{\langle |\mathbf{u}_1| \rangle \left(u_1 - \langle u_1 \rangle\right) + |\mathbf{u}_1| \langle u_1 \rangle}{\langle |\mathbf{u}_1| \rangle \left(\langle u_1 \rangle^2 + \langle v_1 \rangle^2\right)^{1/2}} \tag{2.30}$$

and

$$\tau_{yz0} = -u_{*0}^2 \frac{\langle |\mathbf{u}_1| \rangle \left(v_1 - \langle v_1 \rangle\right) + |\mathbf{u}_1| \langle v_1 \rangle}{\langle |\mathbf{u}_1| \rangle \left(\langle u_1 \rangle^2 + \langle v_1 \rangle^2\right)^{1/2}} \tag{2.31}$$

Similarly, for the local vertical SFS heat flux:

$$\tau_{\theta z0} = \left\langle w'\theta' \right\rangle_s \frac{\langle |\mathbf{u}_1| \rangle \left(\theta_1 - \langle \theta_1 \rangle\right) + |\mathbf{u}_1| \left(\langle \theta_1 \rangle - \langle \theta_0 \rangle\right)}{\langle |\mathbf{u}_1| \rangle \left\langle \langle \theta_1 \rangle - \langle \theta_0 \rangle \right\rangle} \tag{2.32}$$

where the average surface temperature $\langle \theta_0 \rangle$ is determined from MO similarity, the surface heat flux $\left\langle w'\theta' \right\rangle_s$ and the temperature at z_1 $\langle \theta_1 \rangle$.
At the top boundary, the vertical gradients of the horizontal wind speed components follow the specified gradients of U_g and V_g, and the vertical gradient of θ is set to a constant. The fluctuations of vertical velocity and pressure follow the radiation boundary condition of Klemp and Durran (1983).

3

DISCUSSION – PAPER I AND PAPER II

The purpose of the this chapter is to elaborate on topics, results and discussions presented in Paper I and Paper II, and to highlight links between the two papers.

3.1 Realistic forcing

The two case studies in Paper I (Høvsøre and Hamburg) demonstrate the need for accurate specification of the driving pressure gradient when using LES for prediction of wind speeds in the real-world ABL. The paper falls within a range of recent studies (e.g. Moeng et al., 2007; Basu et al., 2008; Kumar et al., 2010; Liu et al., 2011; Talbot et al., 2012; Mirocha et al., 2013; Rizza et al., 2013) aiming at using LES for simulation of more realistic conditions than what have been the norm so far. The motivation behind a majority of these studies is to explore methods for nesting LES domains within larger meso- and/or synoptic-scale simulation domains, facilitating coupling between the turbulent eddies resolved by the LES and the larger-scale phenomena covered by the outer domains. Potential future applications of such a methodology include forecasting of the local terrain-dependent turbulent flow at sites of existing or planned wind farms. There are, however, still many issues to be solved, including how to handle the abrupt changes in grid resolution between mesoscale and LES domains and the transition from a flow where in principal no turbulence is resolved to a flow where most of the turbulence is resolved (Mirocha et al., 2013). The use of intermediate domains with resolutions finer than in typical mesoscale simulations and coarser than in typical LES is discussed by Wyngaard (2004) who points out that traditional SFS models cannot be expected to perform well in simulations of such intermediate resolution.

The simulations presented in Paper I are of relatively high resolution, and the applied pressure gradients are based purely on measurements. In this sense, the Høvsøre and Hamburg case studies are more fundamental tests of the LES model than the studies involving mesoscale modelling and nested domains. The purpose is to verify that the model can reproduce real-world wind profiles, and to identify what type of external forcing is needed to make it do so.

The two case studies indicate that at least accurate specification of the height- and time-dependence of the pressure forcing is required to obtain wind profiles which agree with measurements. The Hamburg case study furthermore suggests that inclusion of phenomena such as large scale height-dependent advection and subsidence influencing the temperature profile and the boundary layer height, can be necessary for accurate wind

speed predictions.
However, as also illustrated by the two case studies, accurate specification of the driving pressure gradient requires measurements which are rarely available; ideally measurements of the pressure and/or the temperature at several locations and at several heights throughout the ABL, or as in the Høvsøre case, continuous measurements of the wind speed above the ABL.
The Hamburg case study is in particular interesting because the time-dependent surface pressure gradient across the city is actually available. It is estimated from measurements of the surface pressure at the three locations around the city shown in figure 3.1, i.e. at Wettermast-Hamburg (the site of the meteorological mast, TV tower and LIDAR), Borstel-Hohenraden and Stuvenborn.

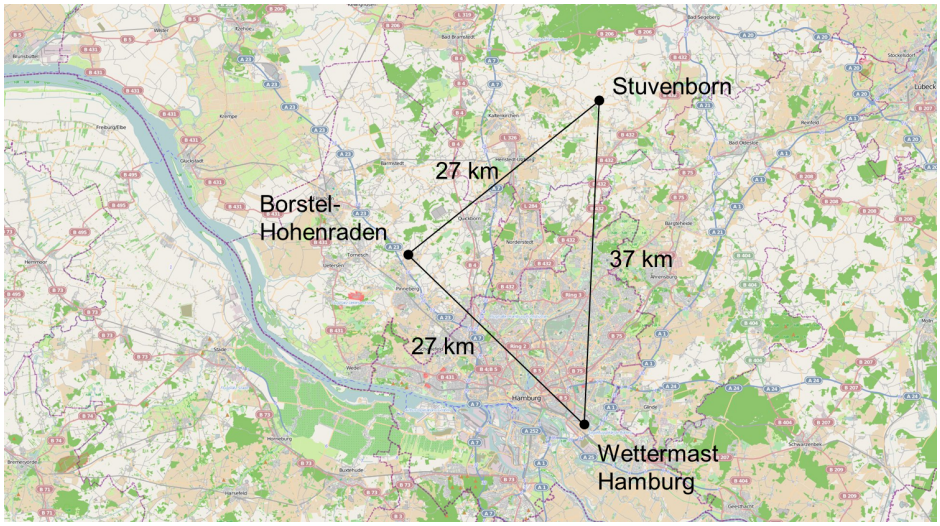

Figure 3.1: Locations of pressure measurements around Hamburg

The pressure measured at 2, 16 and 29 m above sea-level at the three locations, is brought to the sea-level values p_1, p_2 and p_3 using the hypsometric equation. From the sea-level pressures an effective pressure gradient is calculated based on the method described in Kristensen and Jensen (1999). Representing the three locations by the coordinates (x_1, y_1), (x_2, y_2) and (x_3, y_3), and assuming the pressure to vary linearly inside the trian-

gle made up of these coordinates, the three equations

$$\begin{aligned} p_1 &= p_0 + x_1 \frac{\partial p}{\partial x} + y_1 \frac{\partial p}{\partial y} \\ p_2 &= p_0 + x_2 \frac{\partial p}{\partial x} + y_2 \frac{\partial p}{\partial y} \\ p_3 &= p_0 + x_3 \frac{\partial p}{\partial x} + y_3 \frac{\partial p}{\partial y} \end{aligned} \tag{3.1}$$

can be solved for the unknowns, $\frac{\partial p}{\partial x}$, $\frac{\partial p}{\partial y}$ and p_0 representing the two horizontal components of the pressure gradient and the pressure at $(x_0, y_0) = (0,0)$ inside the triangle.
The derived pressure gradient (shown in figure 3.2) is assumed to be a fair approximation of the pressure gradient actually driving the surface flow at the Hamburg site. Nevertheless, the simulations in which U_g and V_g are specified to follow the observed gradient (i.e. $\mathrm{Ha_t}$ and $\mathrm{Ha_{t+z}}$), tend to overestimate the wind speed in the lower part of the ABL between 10:00 and 13:00 CET (the simulated period is from 9:00 to 15:30 – more details can be found in Paper I). In this 3-hour period the observed wind at 10 m is from the south, and it is possible that the pressure measured at the site of the TV tower at the southern edge of the city was influenced by city-induced stagnation of the approaching flow. This would in turn cause an overestimation of the magnitude of the driving pressure gradient and thereby also of the wind speed as observed. After 13:00 the observed wind direction becomes more westerly making this source of error less relevant.
As concluded in Paper I, the measurements available in the Hamburg case study are insufficient to accurately determine the height dependence of the driving pressure gradient. The simulated wind profiles in figure 7(b) of Paper I indicate that the pressure gradient applied in simulation $\mathrm{Ha_{t+z}}$ increases too rapidly with height near the surface, where simulation $\mathrm{Ha_t}$ with $\frac{\partial U_g}{\partial z} = \frac{\partial V_g}{\partial z} = 0$ shows better agreement with the measured wind profiles.
With the difficulties in obtaining an accurate pressure gradient from measurements, the approach of using results from a mesoscale simulation to drive the LES appears as an attractive alternative. As discussed briefly in Paper I, it was considered to use pressure fields from an already available WRF forecast focused on the Hamburg area, but the derived surface pressure gradient was found to agree poorly with the pressure gradient derived from the measured pressures. A thorough analysis of the reason behind the observed disagreement is considered to be beyond the scope of this study. The WRF pressure gradient was calculated in the same way as the one based measurements, and from pressure values at the three grid points in closest vicinity of the three locations where the measured pressure values were obtained. The components of the horizontal pressure gradients derived from measurements and the WRF forecast are shown in figure 3.2.
In the Høvsøre case study, a height- and time-dependent pressure forcing is estimated

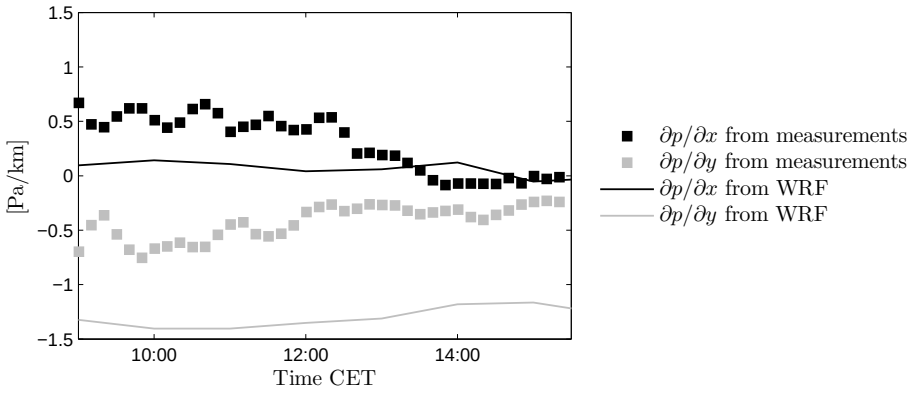

Figure 3.2: Components of the surface pressure gradient derived from measurements and a WRF forecast in the Hamburg case study.

from continuous LIDAR measurements of the wind speed above the ABL. It is applied in the simulation referred to as $\text{H}\emptyset_{\text{t+z}}$, and good agreement is found between simulated and measured wind speeds within the ABL.

3.2 Temperature effects

The simulations in Paper II represent more idealized and less realistic boundary layers than those in Paper I. The conditions are barotropic and the driving pressure gradient as well as the surface heat flux is kept constant throughout the simulation periods of 24 hours. As described in section 2.1, the surface heat flux is typically not constant during the course of the day, and constant barotropic pressure forcing over more than a few hours is also considered to be rare. Such idealized conditions are nevertheless often assumed in LES studies to facilitate investigation of specific phenomena in an undisturbed and steady-state flow, e.g. the influence of atmospheric stability (Moeng and Sullivan, 1994), entrainment (Otte and Wyngaard, 2001), the structure of the ABL (Schmidt and Schumann, 1989), or the influence of purely modelling-related parameters such as the grid resolution or different numerical schemes (Brasseur and Wei, 2010; Sullivan and Patton, 2011; Andren et al., 1994; Beare et al., 2006).

3.2.1 Brunt Vaisala frequency and surface heat flux

Paper II is a study of how changes in the temperature gradient above the ABL expressed in terms of the Brunt Vaisala frequency $N = \left(\frac{g}{\theta}\frac{\partial\theta}{\partial z}\right)^{1/2}$ and the heat flux at the surface affects the development and steady state of the simulated flow. As outlined in section 2.2, the influence of the surface heat flux on the surface layer wind profile is well described by MO-similarity through the Obukhov length L. The steady-state wind profiles from simulations n_{02}, n_{03}, n_{07}, n_{09} shown in figure 3.3 confirm this. Simulations n_{02} and n_{03} are neutral cases with no surface heat flux, while n_{07} and n_{09} are near-neutral cases with a surface heat flux of $0.005\,\mathrm{K\,m\,s^{-1}}$. The applied surface heat flux $\langle w'\theta'\rangle_s$ as well as the vertical gradient of the initial temperature profile $\frac{\partial\theta_i}{\partial z}$ and the corresponding free atmosphere Brunt Vaisala frequency of all the simulations in Paper II is provided in table 3.1.

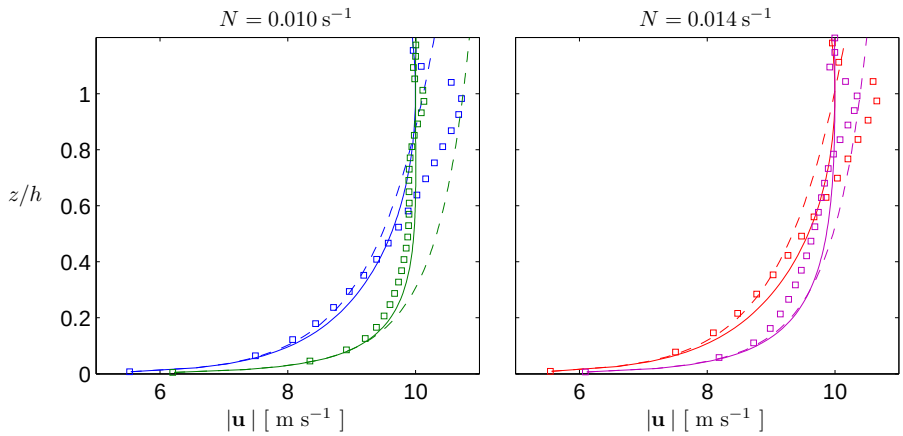

Figure 3.3: Simulated wind speeds from the neutral cases (n_{02},n_{03}) and the near-neutral cases (n_{07},n_{09}) are represented by blue, red, green and purple markers. Solid lines are wind speeds based on the model of Gryning et al. (2007), and dashed lines are based on MO-similarity

Figure 3.3 also shows that relatively small changes in the surface heat flux can significantly change the wind profile – not only in the surface layer, but throughout the ABL. The strictly conventionally neutral wind profiles (blue and red markers representing n_{02} and n_{03}) follow MO-similarity (dashed lines) up to $z/h \simeq 0.5$ and the near-neutral wind profiles (green and purple markers representing n_{07} and n_{09}) up to $z/h \simeq 0.2$. The model of Gryning et al. (2007) (solid lines) is not very different from MO-similarity in the neutral cases, but it agrees significantly better with the LES results in the near-neutral

cases than the profiles based on MO-similarity do, especially in the case of n_{07} with $N = 0.01\,s^{-1}$. However, as also indicated by figures 8 and 12 in paper II, increasing N causes an increase of the wind shear throughout most of the ABL which is not captured by the model of Gryning et al. (2007). The profiles in figure 3.3 are calculated with the value of S in equation 2.5 set to zero (in contrast to Gryning et al., 2007; Kelly and Gryning, 2010).

The analysis presented here and in Paper II indicate that a model for the wind profile above the surface layer should include the free atmosphere Brunt Vaisala frequency (N). Gryning et al. (2007) discuss the possibility of doing so, by using a geostrophic drag law formulation including N/f (e.g. Zilitinkevich and Esau, 2005) for determining L_{MBL}. However, in the cases presented here the geostrophic wind speed is a known quantity, and there is no need for a geostrophic drag law; the analytical wind profiles in figure 3.3 match exactly the geostrophic wind at $z = h$.

The simulated wind speeds are on the other hand generally super-geostrophic at $z = h$. This is, however, most likely a consequence of the highly idealized conditions of the simulations, in particular the lack of variation in the surface heat flux. As illustrated in figure 3.3 (left), the small increase in surface heat flux from 0 to $0.005\,K\,m\,s^{-1}$ is enough to make the super-geostrophic jet nearly disappear.

3.2.2 Baroclinicity

Two simulations in addition to those in Paper II were performed to investigate the effect of baroclinicity on the wind profile. The basic setup of these is similar to that of simulation n_{02}, and they are referred to as n_{02^+} and n_{02^-} (see table 3.1). U_g is in n_{02^+} set to increase from $10\,m\,s^{-1}$ at the surface to $15\,m\,s^{-1}$ at the top of the domain (at $z = 2000\,m$), and in n_{02^-} to decrease from $10\,m\,s^{-1}$ at the surface to $5\,m\,s^{-1}$ at $z = 2000\,m$. V_g is in both simulations set to zero at all heights. The resulting baroclinic shear $\frac{\partial |\mathbf{G}|}{\partial z} = \frac{\partial \left(U_g^2 + V_g^2\right)^{1/2}}{\partial z}$ is $0.0025\,s^{-1}$ in n_{02^+} and $-0.0025\,s^{-1}$ in n_{02^-}.

Wind speeds from n_{02}, n_{02^+} and n_{02^-} averaged over the period between 23 and 24 hours of simulation time are represented in figure 3.4 by the blue, red and green markers. Increasing the applied baroclinic shear decreases the size of the super-geostrophic jet and increases the simulated wind shear in the upper half of the ABL. These effects are similar to those of increasing the Brunt Vaisala frequency above the ABL (see figure 8 (a) Paper II). The increased shear can be accounted for in the model of Gryning et al. (2007) by reducing the length scale of the flow in the upper ABL; i.e. by increasing S in equation 2.5, which then should depend not only on the baroclinic shear as in equation 2.6 but also on N.

The solid lines in figure 3.4 represent profiles based on equations 2.4 and 2.5 with $S \neq 0$. In the baroclinic cases (n_{02^+} and n_{02^-}), S is set to 1.6 and -1.5 respectively, based on equation 2.6. In the barotropic case (n_{02}), S is set to 2.1 which is found to give good agreement between the analytical profile and LES. The dashed lines represent profiles

Table 3.1: Applied surface heat flux, vertical gradient of the initial temperature profile, the free atmosphere Brunt Vaisala frequency and the baroclinic shear of the performed simulations. The values of S are obtained by fitting wind profiles based on equations 2.4 and 2.5 to the simulated wind profiles.

	$\langle w'\theta' \rangle_s$ [K m s^{-1}]	$\frac{\partial \theta_i}{\partial z}$ [K m^{-1}]	N [s^{-1}]	$\frac{\partial \lvert \mathbf{G} \rvert}{\partial z}$ [s^{-1}]	S
n_{01}	0	0.001	0.006	0	1.5
n_{02}	0	0.003	0.010	0	2.1
n_{02+}	0	0.003	0.010	0.0025	–
n_{02-}	0	0.003	0.010	-0.0025	–
n_{03}	0	0.006	0.014	0	2.6
n_{04}	0	0.010	0.018	0	2.9
n_{05}	0.001	0.003	0.010	0	–
n_{06}	0.003	0.003	0.010	0	–
n_{07}	0.005	0.003	0.010	0	–
n_{08}	0.001	0.006	0.014	0	–
n_{09}	0.005	0.006	0.014	0	–
n_{10}	0.007	0.006	0.014	0	–

based on equations 2.4 and 2.5 with $S = 0$. L_{MBL} is in all cases determined to make the analytical wind profiles coincide with the simulated wind speed at $z = h$.
In the baroclinic cases, the wind shear of the analytical profiles based on $S = 1.6$ and $S = -1.5$ does not match the simulated wind shear, and including N in the formulation of S would likely improve the agreement. The exact relation between N and S is, however, not clear. In the barotropic case, $S = 2.1$ clearly gives better agreement between the analytical profile and the LES profile than $S = 0$. Similar good agreement is found with wind profiles from the other neutral barotropic simulations presented in Paper II, using the values of S given in table 3.1 based least-square fitting.

3.2.3 Case studies

In figure 3.4 is also shown the wind profile from simulation Hø_{const} (from the Høvsøre case study in Paper I) averaged over the last hour of the simulation period, i.e. between 6.5 and 7.5 hours of simulation time. With constant barotropic forcing and a free atmosphere Brunt Vaisala frequency of 0.01 s^{-1} it is comparable to simulation n_{02} (Paper II). However, with the surface heat varying around 0.075 K m s^{-1}, the conditions in the Hø_{const}-simulation are much more convective than in any of the simulations in Paper II.

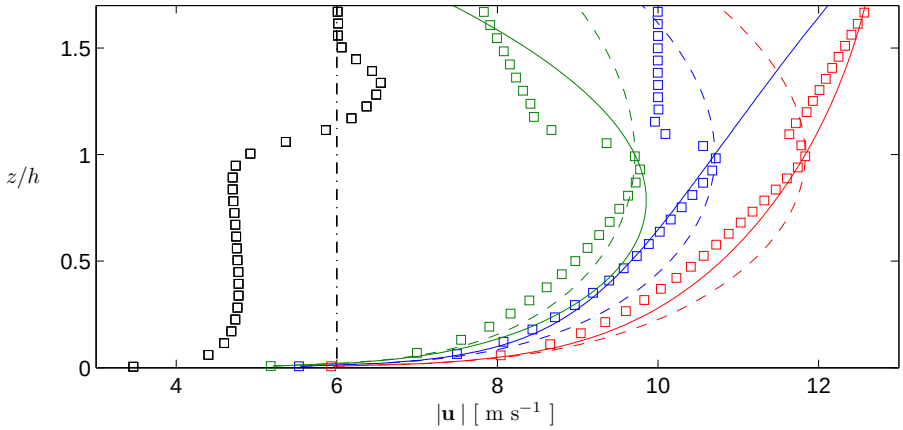

Figure 3.4: Black, blue, red and green markers represent wind speeds from simulations Hø_{const}, n_{02}, n_{02^+} and n_{02^-}. Solid and dashed lines represent wind profiles based on equations 2.4 and 2.5 with $S \neq 0$ and $S = 0$. The black dash-dot line represent the applied value of $|\mathbf{G}|$ in Hø_{const}.

As a consequence of this and the associated increase in turbulent mixing, the wind speed is nearly constant with height from the top of the surface layer to the top of the ABL. The sharp change in wind speed just above $z/h = 1$ is thought to be a consequence of the initial conditions of the simulation which include a sharp increase in the potential temperature between the free atmosphere above $z = 650$ m and a layer of constant potential temperature below $z = 550$ m. The applied capping inversion inhibits mixing of momentum between the ABL and the free atmosphere, and the wind speed in the upper part of the ABL only slowly approaches the geostrophic wind speed; after 7.5 hours of simulation time it is still increasing. The super-geostrophic part of the wind profile just above the ABL is simply due to a similar feature in the specified initial wind speed profile (see figure 3 (a) in Paper I). It is worth noting that the wind profile of simulation Hø_{const} is quite similar to the convective profile found by Moeng and Sullivan (1994), also based on a large-eddy simulation initialized with a strong capping inversion. As a contrast, each simulation in Paper II is initialized with a constant temperature gradient throughout the computational domain, and the capping inversion develops gradually as shown in figure 5 Paper II. In these simulations, the ABL wind speed adapts more smoothly to the geostrophic wind speed, at least until the super-geostrophic jet develops after approximately 9 hours of simulation time.

Unfortunately there are no measurements of the potential temperature available in the Høvsøre case study above 100 m, and the initial profile used in all three Høvsøre-

simulations is merely a rough estimate. However, the good agreement between the wind speeds of simulation $H\emptyset_{t+z}$ and measured wind speeds (figure 3 (c) in Paper I), indicates that it is not too far off.

The simulations of the Hamburg case study in Paper I are initialized to make the potential temperature after 1.5 hours of simulation time match a radio sounding started at 9:30 CET. However, despite good agreement in the morning, significant differences between simulated and measured temperature profiles are observed later in the day (figure 3.5 (left) and figures 11 (b) and (c) in Paper I). The profile obtained from a radio sounding started at 13:15 exhibits a mixed layer of constant potential temperature from the surface up to 1500 m and above that a capping inversion over approximately 400 m with a strength of $0.02\,\mathrm{K\,m^{-1}}$ as indicated by the blue dashed line in figure 3.5 (left); the corresponding Brunt Vaisala frequency is $N = 0.026\,\mathrm{s^{-1}}$. The boundary layer height estimated from ceilometer data is 1700 m. Above 1900 m the potential temperature increases at a rate of approximately $0.002\,\mathrm{K\,m^{-1}}$ corresponding to $N = 0.008\,\mathrm{s^{-1}}$. The simulated potential temperature at the corresponding time is also nearly constant with height up 1500 m, but a few degrees below the measured temperature. Above this mixed layer, it increases at a rate of $0.01\,\mathrm{K\,m^{-1}}$ $\left(N = 0.018\,\mathrm{s^{-1}}\right)$ up to approximately 2300 m as indicated by the red dashed line in figure 3.5 (left).
The difference in inversion strength is mentioned in Paper I as possible reason for the difference between simulated and measured wind speeds (figure 3.5 (right)). This hypothesis is supported by the simulations described in Paper II. Profiles of potential temperature and wind speed from simulations n_{07} and n_{09} are shown in figure 3.6. The two simulations are initiated with different temperature profiles, i.e. with $N = 0.010\,\mathrm{s^{-1}}$ and $N = 0.014\,\mathrm{s^{-1}}$ at all heights, but are otherwise similar. An inversion-capped mixed layer develops over time in both simulations, and as indicated by the dashed lines in figure 3.6 the steady-state inversion strengths are $0.01\,\mathrm{K\,m^{-1}}$ and $0.02\,\mathrm{K\,m^{-1}}$ in the two cases respectively ($N = 0.018\,\mathrm{s^{-1}}$ and $N = 0.027\,\mathrm{s^{-1}}$). The stronger inversion in simulation n_{09} causes higher wind shear throughout the ABL. This is similar to what is observed in the Hamburg case study, where the simulated inversion strength and boundary layer wind shear are low compared to the measured. Thus more accurate simulation with respect to temperature could lead to better agreement between simulated and measured wind speeds. More frequent radio soundings would facilitate this. The observed temperature difference in the Hamburg case study is assumed to be mainly due to large scale advection of warm air not included in the LES, and not related to the assumed baroclinicity.
The height dependence of U_g and V_g applied in the baroclinic simulations (Ha_{t+z}, $H\emptyset_{t+z}$, n_{02^+}, n_{02^-}) is theoretically related to horizontal and vertical temperature gradients through

the thermal wind equations:

$$\begin{aligned} \frac{\partial U_g}{\partial z} &= -\frac{g}{fT}\frac{\partial T}{\partial y} + \frac{U_g}{T}\frac{\partial T}{\partial z} \\ \frac{\partial V_g}{\partial z} &= \frac{g}{fT}\frac{\partial T}{\partial x} + \frac{V_g}{T}\frac{\partial T}{\partial z}. \end{aligned} \tag{3.2}$$

The influence of the vertical temperature gradient is small and usually neglected (Arya and Wyngaard, 1975). Furthermore, in the baroclinic simulations presented here, the influence on the wind profile of the implied horizontal temperature gradient and the associated advection was assumed to be small and not included.
The values of $\frac{\partial U_g}{\partial z}$ and $\frac{\partial V_g}{\partial z}$ applied for $z < 2000$ m in $\mathrm{Ha}_{\mathrm{t+z}}$ are $2 \cdot 10^{-3}\,\mathrm{s}^{-1}$ and $-8 \cdot 10^{-4}\,\mathrm{s}^{-1}$ respectively when averaged over the period between the radio soundings at 9:30 and 13:15. These values imply $\frac{\partial T}{\partial y} = -7 \cdot 10^{-6}\,\mathrm{K\,m}^{-1}$ and $\frac{\partial T}{\partial x} = -3 \cdot 10^{-6}\,\mathrm{K\,m}^{-1}$ on average. Over the same period the wind speed components in the x- and y-directions average to 4.3 and 3.7 $\mathrm{m\,s}^{-1}$ respectively. This leads to an estimated temperature change of $-0.5\,\mathrm{K}$ due to advection over the 3.75-hour period; a relatively small value compared to the difference between the simulated temperature and the radio sounding at 13:15, and furthermore with the opposite sign of what would bring the simulated temperature closer to the measured. The performed radio soundings are too infrequent to help determine if the observed temperature difference is due to constant or time-varying advection and how this changes with height. Including large-scale advection in the LES would require more measurements.

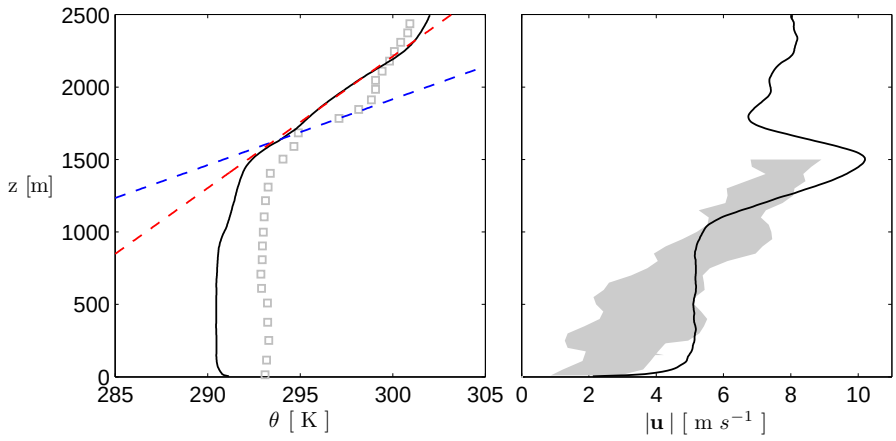

Figure 3.5: Simulated and measured potential temperatures (left) and wind speeds (right) from the Hamburg case study. Grey markers represent measurements from a radio sounding started at 13:15 and the grey area covers wind speeds measured by LIDAR and sonic anemometers between 12:30 and 13:30. Solid black lines represent results from simulation $\mathrm{Ha}_{\mathrm{t+z}}$ at times corresponding to those of the measurements. The blue and red dashed lines have slopes of 0.02 and $0.01\,\mathrm{K\,m^{-1}}$.

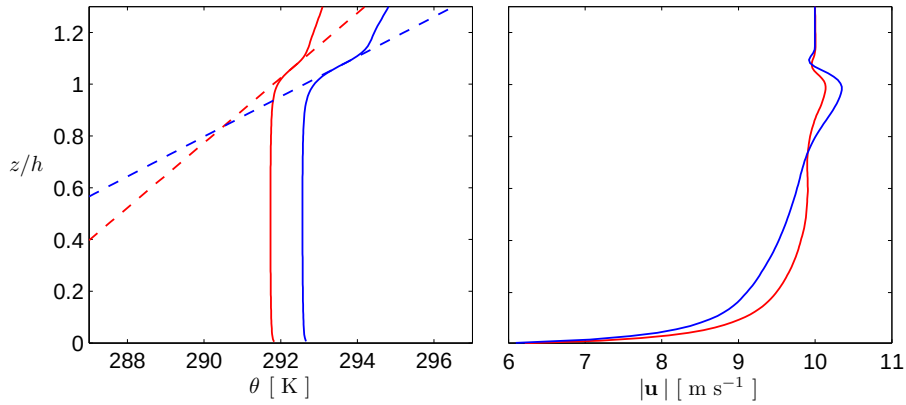

Figure 3.6: Simulated profiles of potential temperature (left) and wind speed (right). Red lines represent simulation n_{07} and blue lines simulation n_{09}. The red and blue dashed lines have slopes of 0.01 and $0.02\,\mathrm{K\,m^{-1}}$.

4

CONCLUDING REMARKS

The aim of the presented work has been to obtain a better understanding of the flow of air in the ABL through use of LES. The two papers forming the base of this thesis represent two quite different approaches for doing so; one is based on a combination of simulations and measurements and the other on simulations alone. General conclusions of the two papers, and of the discussion in chapter 3 joining the two, are summarized below. Please refer to the individual papers for more detailed conclusions.

Paper I consists of two case studies: One from the rural site of Høvsøre, Denmark and one from a suburban site in Hamburg, Germany. In the Høvsøre case study good agreement is found between measured and simulated wind speeds in the entire ABL, but only when the pressure gradient driving the flow is specified to vary with both time and height – in agreement with a pressure gradient estimated from measurements of the wind speed above the ABL. The method for determining the driving pressure gradient in the Høvsøre case study is based on the assumptions that the only forces acting on the flow above the ABL are due to the pressure gradient and rotation of the Earth, and that the observed acceleration of the flow is constant over the studied period. Furthermore, it assumed that the baroclinic shear observed above the ABL extends all the way to the surface. The good agreement between simulated and measured wind speeds throughout the ABL – especially towards the end of the studied period – suggests that these assumptions are accurate. However, the underestimation of the wind speed in the middle of the period is mainly due to the fact that the acceleration of the flow is not actually constant but decreases during the period. Furthermore, it seems the capping inversion of the assumed initial profile of potential temperature is too strong, which causes the sharp change in wind speed across the top of the boundary layer seen in figure 3 (b) of Paper I. Nevertheless, the case study demonstrates the ability of the LES code to accurately reproduce real-world wind profiles, and it provides confidence in results from other simulations as well, e.g. those presented in Paper II. Moreover, it clearly illustrates the consequence of neglecting baroclinicity and temporal variation of the driving pressure gradient, i.e. poor agreement with measured wind speeds throughout the studied period. The wind speed at the hub-height of a modern wind turbine is in the last part of the period underestimated by approximately 25% when assuming barotropic conditions, and by 40% when also assuming the pressure gradient to be constant in time.
The findings are less clear in the Hamburg case study. Nevertheless, based on the last part of the studied period, the conclusion is the same as in the Høvsøre case study: neither

temporal variation of the driving pressure gradient nor baroclinic effects can be neglected when aiming at best possible agreement between simulated and measured wind speeds. In the middle part of the period, however, wind speeds from the barotropic simulations agree better with measurements up to approximately 1 km than wind speeds from the baroclinic simulation. This indicates that the applied baroclinic shear $\left(\frac{\partial}{\partial z}\left(U_g^2+V_g^2\right)^{1/2}\right)$ is too high in the lower part of the domain, and it is concluded that the available measurements are insufficient for accurate estimation of the effective baroclinicity in the specific case. A more extensive network of pressure and/or temperature measurements – ideally at several heights throughout the ABL – would provide a better foundation for such an estimation.

More frequent temperature measurements from e.g. radio soundings would furthermore facilitate simulation of phenomena such as the large scale advection thought to be responsible for the observed difference between simulated and measured temperatures in the Hamburg case study. As the results from Paper II show (e.g. figure 3.6), a difference in the vertical temperature gradient above the ABL, similar to the difference between the measured and the simulated gradient in the Hamburg case study, leads to significantly different wind profiles. Thus it is not necessarily enough to apply accurate pressure forcing; large scale phenomena influencing the temperature field should also be taken into account.

From a wind-energy perspective, a case such as the one from Hamburg is interesting due to the low wind speeds varying around the cut-in wind speed of modern wind turbines; accurate day-to-day prediction of whether a wind farm can be expected to produce power or not, is important with respect to e.g. interaction with the electrical grid, regulation of the power produced by conventional power plants and energy trading. Cf. chapter 3, there is a growing interest in using LES for simulation of realistic conditions and forecasting of mean wind and turbulence, e.g. by nesting LES domains within larger domains of coarser resolution. The study presented in Paper I is a step in this direction, demonstrating the ability of the LES code to produce real-world wind profiles and the need for accurate representation of flow variations occurring over scales larger than the LES domain.

Paper II is based on simulations of more idealized conditions than those considered in Paper I. This enables a more transparent and meticulous study of the influence of changes in the free atmosphere Brunt Vaisala frequency N and the surface heat flux on the simulated wind profile. From a practical point of view, however, making use of the very idealized results is not straightforward. An original aim of the study was to improve upon the wind profile model of Gryning et al. (2007), by examining and appropriately including the effect N, but whereas the analytical model assumes the wind speed to smoothly adapt to the geostrophic wind at the top of the ABL, the steady-state wind speeds of the strictly conventionally neutral simulations are consistently super-geostrophic at the top of the ABL.

As demonstrated in figure 3.4 it is possible to make the analytical model agree with the simulated wind profile by fitting it to the super-geostrophic value at $z = h$ and applying an appropriate value of S. However, one has to question if this approach is of more than just academic interest. The simulated profiles are not considered to be inaccurate or wrong, but merely representative of rarely occurring conditions. A coming study of LIDAR measurements of wind speeds at the site of Station Nord (Batchvarova et al., 2013) located in the north-east part of Greenland will possibly confirm the credibility of the simulated wind profiles and the consistent development of a super-geostrophic jet in long-lived neutral and near-neutral conditions. Outside the polar regions and especially over land, diurnal variation in the solar radiation prevents the long periods of negligible or slightly positive surface heat flux required for the jet to develop as suggested by the simulations.

On the other hand, as illustrated by the wind profiles in figure 3.3, the applied surface heat flux does not have to be large, to cause the simulated profiles to adapt smoothly to the geostrophic wind; on the order of $0.005\,\mathrm{K\,m\,s^{-1}} \simeq 5\,\mathrm{W\,m^{-2}}$ in the simulation with $N = 0.01\,\mathrm{s^{-1}}$. Thus it is possible to obtain wind profiles without the super-geostrophic jet in simulations which based on the Obukhov length belong in the "neutral" category of the stability classification of Gryning et al. (2007). Such simulations are possibly of more practical use than the strictly neutral simulations. More work is, however, needed to fully understand the interaction between the surface heat flux and the influence of the free atmosphere Brunt Vaisala frequency.

Figure 10 in Paper II suggests a linear dependence between the size of the super-geostrophic jet and the heat flux integrated across the ABL. Combining this with the linear height-dependence of the heat flux shown in figure 9 and the model of Batchvarova and Gryning (1991) for the entrainment heat flux expressed in equation 14, an estimate of the jet size can be made based on the surface heat flux, the surface friction velocity and the height and temperature of the ABL. However, like the actual existence of the jet, these relations have to be more firmly verified, preferably by measurements.

Bibliography

Andren, A., Brown, A. R., Graf, J., Mason, P. J., Moeng, C.-H., Nieuwstadt, F. T. M., and Schumann, U. (1994). Large-eddy simulation of a neutrally stratified boundary layer: A comparison of four computer codes. *Quart. J. Roy. Meteor. Soc.*, 120:1457–1484.

Arya, S. P. S. and Wyngaard, J. C. (1975). Effect of baroclinicity on wind profiles and the geostrophic drag law for the convective planetary boundary layer. *J. Atmos. Sci.*, 32:767–778.

Basu, S., Vinuesa, J.-F., and Swift, A. (2008). Dynamic LES Modeling of a Diurnal Cycle. *J. Appl. Meteor. Climatol.*, 47:1156–1174.

Batchvarova, E. and Gryning, S.-E. (1991). Applied model for the growth of the daytime mixed layer. *Bound.-Layer Meteor.*, 56:261–274.

Batchvarova, E., Gryning, S.-E., Skov, H., Sørensen, L. L., Kirova, H., and Münkel, C. (2013). Boundary-layer and air quality study at "Station Nord" in Greenland. In Steyn, D. G. and Mathur, R., editors, *Air pollution modeling and its application*, Dordrect. Springer Science + Business Media B. V. In press.

Beare, R. J., MacVean, M. K., Holtslag, A. A. M., Cuxart, J., Esau, I., Golaz, J.-C., Jimenez, M. A., Khairoutdinov, M., Kosović, B., Lewellen, D., Lund, T. S., Lundquist, J. K., McCabe, A., Moene, A. F., Noh, Y., Raasch, S., and Sullivan, P. (2006). An intercomparison of large-eddy simulations of the stable boundary layer. *Bound.-Layer Meteor.*, 118:247–272.

Blackadar, A. K. and Tennekes, H. (1968). Asymptotic similarity in neutral barotropic planetary boundary layers. *J. Atmos. Sci.*, 25:1015–1020.

Brasseur, J. G. and Wei, T. (2010). Designing large-eddy simulation of the turbulent boundary layer to capture law-of-the-wall scaling. *Phys. Fluids*, 22. 021303.

Brown, A. R., Beljaars, A. C. M., and Hersbach, H. (2006). Errors in parametrizations of convective boundary-layer turbulent momentum mixing. *Quart. J. Roy. Meteor. Soc.*, 132:1859–1876.

Businger, J. A., Wyngaard, J. C., Izumi, Y., and Bradley, E. F. (1971). Flux-profile relataionships in the atmospheric surface layer. *J. Atmos Sci.*, 28:181–189.

Carl, D. M., Tarbell, T. C., and Panofsky, H. A. (1973). Profiles of wind and temperature from towers over homogeneous terrain. *J. Atmos. Sci.*, 30:788–794.

Deardorff, J. W. (1980). Stratocumulus-capped mixed layers derived from a three-dimensional model. *Bound.-Layer Meteor.*, 18:495–527.

Dyer, A. J. (1974). A review of flux-profile relationships. *Bound.-Layer Meteor.*, 7:363–372.

Eurostat (2013). Europe 2020 indicators. `http://epp.eurostat.ec.europa.eu/portal/page/portal/europe_2020_indicators/headline_indicators`. [Online; accessed 11-October-2013].

EWEA (2013). Wind in power, 2012 European statistics. `http://www.ewea.org/fileadmin/files/library/publications/statistics/Wind_in_power_annual_statistics_2012.pdf`. [Online; accessed 11-October-2013].

Floors, R., Vincent, C. L., Gryning, S.-E., Peña, A., and Batchvarova, E. (2013). The wind profile in the coastal boundary layer: Wind lidar measurements and numerical modelling. *Bound.-Layer Meteor.*, 147:469–491.

Gryning, S.-E., Batchvarova, E., Brümmer, B., Jørgensen, H., and Larsen, S. (2007). On the extension of the wind profile over homogeneous terrain beyond the surface boundary layer. *Bound.-Layer Meteor.*, 124:251–268.

GWEC (2013). Global wind statistics 2012. `http://www.gwec.net/wp-content/uploads/2013/02/GWEC-PRstats-2012_english.pdf`. [Online; accessed 11-October-2013].

Holton, J. R. (1992). *An introduction to dynamic meteorology*. Academic Press.

Holtslag, A. A. M. (1984). Estimates of diabatic wind speed profiles from near-surface weather observations. *Bound.-Layer Meteor.*, 29:225–250.

Kelly, M. and Gryning, S.-E. (2010). Long-term mean wind profiles based on similarity theory. *Bound.-Layer Meteor.*, 136:377–390.

Klemp, J. B. and Durran, D. R. (1983). An upper boundary condition permitting internal gravity wave radiation in numerical mesoscale models. *Mon. Wea. Rev.*, 111:430–444.

Koren, B. (1993). A robust upwind discretization method for advection, diffusion and source terms. *Notes on Numerical Fluid Mechanics*, 45:117–138.

Kristensen, L. and Jensen, G. (1999). Geostrophic winds in Denmark: A preliminary study. *Risø report*.

Kumar, V., Svensson, G., Holtslag, A. A. M., Meneveau, C., and Parlange, M. B. (2010). Impact of Surface Flux Formulations and Geostrophic Forcing on Large-Eddy Simulations of Diurnal Atmospheric Boundary Layer Flow. *J. Appl. Meteor. Climatol.*, 49:1496–1516.

Liu, Y., Warner, T., Liu, Y., Vincent, C., Wu, W., Mahoney, B., Swerdlin, S., Parks, K., and Boehnert, J. (2011). Simultaneous nested modeling from the synoptic scale to the LES scale for wind energy applications. *J. Wind Eng. Ind. Aerodyn.*, 99:308–319.

Mirocha, J., Kirkil, G., Bou-Zeid, E., Chow, F. K., and Kosović, B. (2013). Transition and Equilibration of Neutral Atmospheric Boundary Layer Flow in One-Way Nested Large-Eddy Simulations Using the Weather Research and Forecasting Model. *Mon. Weather Rev.*, 141:918–940.

Moeng, C.-H. (1984). A Large-Eddy-Simulation Model for the Study of Planetary Boundary-Layer Turbulence. *J. Atmos. Sci.*, 41:2052–2062.

Moeng, C.-H., Dudhia, J., Klemp, J., and Sullivan, P. (2007). Examining two-way grid nesting for large eddy simulation of the PBL using the WRF model. *Mon. Weather Rev.*, 135:2295–2311.

Moeng, C.-H. and Sullivan, P. P. (1994). A Comparison of Shear- and Buoyancy-Driven Planetary Boundary Layer Flows. *J. Atmos. Sci.*, 51:999–1022.

Orszag, S. A. (1971). On the elimination of aliasing in finite-difference schemes by filtering high-wavenumber components. *J. Atmos. Sci.*, 28:1074.

Otte, M. J. and Wyngaard, J. C. (2001). Stably Stratified Interfacial-Layer Turbulence from Large-Eddy Simulation. *J. Atmos. Sci.*, 58:3424–3442.

Paulson, C. A. (1970). The Mathematical representation of wind speed and temperature profiles in the unstable atmospheric surface layer. *J. Appl. Meteor.*, 9:857–861.

Pope, S. B. (2000). *Turbulent Flows*. Cambridge University Press.

Prandtl, L. (1925). Bericht über untersuchungen zur ausgebildeten turbulenz. *Z. angew. Math. Mech.*, 5:136–139.

Rizza, U., Miglietta, M. M., Acevedo, O. C., Anabor, V., Degrazia, G. A., Goulart, A. G., and Zimmerman, H. R. (2013). Large-eddy simulation of the planetary boundary layer under baroclinic conditions during daytime and sunset turbulence. *Meteorol. Appl.*, 20:56–71.

Rossby, C. G. and Montgomery, R. B. (1935). The layer of frictional influence in wind and ocean currents. *Pap. Phys. Oceanogr. Meteorol.*, 3:1–101.

Sathe, A., Mann, J., Gottschall, J., and Courtney, M. S. (2011). Can wind lidars measure turbulence? *J. Atmos. Ocean. Tech.*, 28:853–868.

Schmidt, H. and Schumann, U. (1989). Coherent structure of the convective boundary layer derived from large-eddy simulations. *J. Fluid Mech.*, 200:511–562.

Stull, R. B. (2009). *An introduction to boundary layer meteorology*. Springer Science + Business Media B. V.

Sullivan, P. P., McWilliams, J. C., and Moeng, C.-H. (1994). A subgrid-scale model for large-eddy simulation of planetary boundary-layer flows. *Bound.-Layer Meteor.*, 71:247–276.

Sullivan, P. P., McWilliams, J. C., and Moeng, C.-H. (1996). A grid nesting method for large-eddy simulation of planetary boundary-layer flows. *Bound.-Layer Meteor.*, 80:167–202.

Sullivan, P. P. and Patton, E. G. (2011). The effect of mesh resolution on convective boundary layer statistics and structures generated by large-eddy simulation. *J. Atmos. Sci.*, 68:2395–2415.

Talbot, C., Bou-Zeid, E., and Smith, J. (2012). Nested mesoscale large-eddy simulations with WRF: Performance in real test cases. *J. Hydrometeor.*, 13:1421–1441.

Wyngaard, J. C. (2004). Toward numerical modeling in the "Terra Incognita". *J. Atmos. Sci.*, 61:1816–1826.

Wyngaard, J. C. (2010). *Turbulence in the atmosphere*. Cambridge University Press.

Zilitinkevich, S. and Esau, I. (2002). On integral measures of the neutral barotropic planetary boundary layer. *Bound.-Layer Meteor.*, 104:371–379.

Zilitinkevich, S. S. and Esau, I. N. (2005). Resistance and heat-transfer laws for stable and neutral planetary boundary layers: Old theory advanced and re-evaluated. *Quart. J. Roy. Meteor. Soc.*, 131:1863–1982.

Zilitinkevich, S. S., Tyuryakov, S. A., Troitskaya, Y. I., and Mareev, E. A. (2012). Theoretical models of the height of the atmospheric boundary layer and turbulent entrainment at its upper boundary. *Izv. Atmos. Ocean Phys.*, 48:133–142.

PAPER I:
THE EFFECT OF UNSTEADY AND BAROCLINIC FORCING ON PREDICTED WIND PROFILES IN LARGE EDDY SIMULATIONS: TWO CASE STUDIES OF THE DAYTIME ATMOSPHERIC BOUNDARY LAYER

The effect of unsteady and baroclinic forcing on predicted wind profiles in Large Eddy Simulations: Two case studies of the daytime atmospheric boundary layer

Jesper Grønnegaard Pedersen, Mark Kelly, Sven-Erik Gryning

DTU Wind Energy, Risø Campus, Technical University of Denmark, DK-4000 Roskilde, Denmark

Burghard Brümmer

Meteorological Institute, University of Hamburg, Germany

Accepted for publication in Meteorologische Zeitschrift

Abstract

Due to its fine-resolution requirement and subsequent computational demand, Large Eddy Simulation of the atmospheric boundary layer is limited in most cases to computational domains extending only a few kilometers in both the vertical and horizontal directions. Variations in the flow and in relevant atmospheric fields (e.g. temperature) that occur at larger scales must be imposed through boundary conditions or as external forcing. In this work we study the influence of such variations on the wind profile in Large Eddy Simulations of daytime atmospheric boundary layers, by comparing observations with simulations that use progressively more realistic forcing relative to observed large-scale pressure gradients.

Two case studies are presented. One is based on measurements from the rural site of Høvsøre in Denmark, and the other on measurements from a suburban site in Hamburg, Germany. The applied domain-scale pressure gradient and its height- and time-dependence are estimated from LIDAR measurements of the wind speed above the atmospheric boundary layer in the Høvsøre case, and from radio soundings and a network of ground-based pressure sensors in the Hamburg case.

In the two case studies, LIDAR measurements of the wind speed up to heights between 900 and 1600 m and tower-based measurements up to 100 and 250 m are used to evaluate the performance of the variably-driven Large Eddy Simulations. We find in both case studies that including height- and time-variations in the applied pressure gradient has a significant influence on simulated wind speeds, and improves agreement with measured wind speeds, especially in the Høvsøre case. In the Hamburg

case, an overly simplified specification of the height dependence of the forcing, as well as the influence of phenomena such as large-scale subsidence and advection, tend to reduce agreement with measurements, relative to the Høvsøre case. The Hamburg case illustrates that measurements of the surface pressure gradient and relatively infrequent radio soundings alone are not sufficient for accurate estimation of a height- and time-dependent pressure gradient.

1 Introduction

Since the method was introduced with the work of Deardorff (1970) and Deardorff (1972), Large Eddy Simulation (LES) has become a widely used tool for studying the turbulent flow of the atmospheric boundary layer (ABL). While the general increase in available computer power over the last four decades has made way for simulations of yet finer resolution, the size of the computational domain used in most LES studies has not changed as much. A domain twice as high as the ABL with horizontal dimensions two or three times the vertical extent is often assumed to be sufficiently large, to accommodate most flow structures expected to develop during the simulation time. Thus the size of a typical high-resolution atmospheric LES domain is on the order of $400 \times 400 \times 400\,\mathrm{m}^3$ (Beare et al., 2006) for cases with stable stratification and $5 \times 5 \times 2\,\mathrm{km}^3$ (Sullivan and Patton, 2011) for convective conditions.

It is, however, also well known that the atmosphere contains motions of air varying over spatial and temporal scales larger than a few kilometers and hours, i.e. meso- and synoptic-scale phenomena. Due to the high computational expense, it is generally not feasible to perform high-accuracy LES covering these motions; consequently, if they are to be included in an LES, they must be imposed through boundary conditions or as external forcing. The purpose of this paper is to investigate how simulated wind speeds are affected by application of pressure gradients having time- and height-variations estimated from multiple measurements: LIDAR observations of the wind speed above the ABL, as well as radio soundings and a network of ground-based pressure sensors.

In the case of a balance between a pressure gradient driving the wind and the Coriolis force due to the rotation of the Earth, the wind is geostrophic and directly proportional to the pressure gradient. Such a balance can only exist above the ABL where the flow is non-turbulent and decoupled from surface influences. Even there, however, it is often disturbed by e.g. movements of synoptic high and low pressure systems and phenomena such as sea breezes with associated temporal variations in the pressure field. Exact geostrophic balance furthermore requires equispaced, parallel and straight isobars (Arya, 2001). Thus, even above the ABL the observed wind is rarely geostrophic and care has to be taken when relating it to the driving pressure gradient. In addition, variation with height of the pressure gradient caused by large scale horizontal temperature gradients – also known as baroclinity – is often observed and affects the wind profile, as modeled by e.g. Zilitinkevich and Esau (2005); Gryning et al. (2007); Kelly and Gryning (2010).

In many applications of LES it is, however, adequate and even desirable to use idealized assumptions regarding the pressure gradient driving the mean flow. For instance, prescribing a forcing which is constant with both time and height provides an attractive framework

for research of specific ABL phenomena with a minimum of complications (e.g. Schmidt and Schumann, 1989; Moeng and Sullivan, 1994; Sullivan et al., 1998; Kosović and Curry, 2000; Beare et al., 2006).

On the other hand, if the ambition is to use an LES to simulate a realistic atmospheric flow for e.g. prediction of wind speed or model validation through comparison of simulated wind speeds with atmospheric measurements, then appropriately modelled variations in the driving force are necessary. Deardorff (1974) used a height-dependent pressure gradient roughly estimated from observational data from day 33 of the Wangara experiment (Clarke et al., 1971) to force an LES of the unstable ABL, but – despite the applied height dependence – concludes that variations in the forcing must be modeled more accurately to achieve satisfying agreement between simulated and measured wind speeds. Basu et al. (2008) use data from the same experiment in an LES study of the diurnal cycle, with forcing as a function of height applied via parabolic profiles fitted to surface measurements of geostrophic and thermal winds (Clarke et al., 1971), and temporal variations derived through linear interpolation between measurements. The simulation reproduces prominent features of the observed flow, but significant differences are observed between simulated and measured wind speed and direction, particularly during the afternoon of day 33. Basu et al. (2008) attribute part of the disagreement to inaccuracy in the applied pressure gradient, but the relative importance of this source of error is not clear.

Kumar et al. (2010) addresses this issue by performing a set of six LESs of two subsequent diurnal cycles with different assumptions for the forcing and surface boundary conditions, based on data from the CASES 99 campaign. Using geostrophic forcings derived from a mesoscale simulation, they show in this case that a simulation with constant pressure gradient gives better agreement with measured wind speed profiles in the surface layer (up to 55 m) than simulations with time- and/or height-dependent forcing. However, when comparing to radio soundings covering the entire ABL, the LES driven with temporally and spatially varying forcing are reported to give the best agreement.

In this paper, we continue along the lines of Kumar et al. (2010) and compare measured wind speeds to simulated wind speeds from LESs driven by pressure gradients derived from measurements; this includes forcings which are constant, temporally varying, and functions of both time and height. Two case studies are presented. One is based on a set of measurements from the Danish National Test Station for wind turbines at Høvsøre (Denmark), and the other is based on measurements from a site in Hamburg (Germany).

Continuous Doppler LIDAR measurements of the wind speed – covering most of the ABL in the Hamburg case study and the entire ABL and a region above it in the Høvsøre case study – set the two datasets apart from e.g. the Wangara and CASES-99 datasets, and provide an outstanding opportunity for comparison between simulated and measured wind speeds. Tower-based measurements accompany the LIDAR measurements at both sites, and the Hamburg case study furthermore includes radio soundings and measurements of the surface pressure at three locations around the city.

Further details of the two sites and of the measurements are given in section 2. The case studies are described in section 3, and the LES model and the setup of the simulations in section 4. Results are presented and discussed in sections 5 and 6. Section 7 provides a conclusion of our findings.

2 Sites and measurements

Maps of the areas surrounding the Høvsøre and Hamburg sites are shown in figure 1.

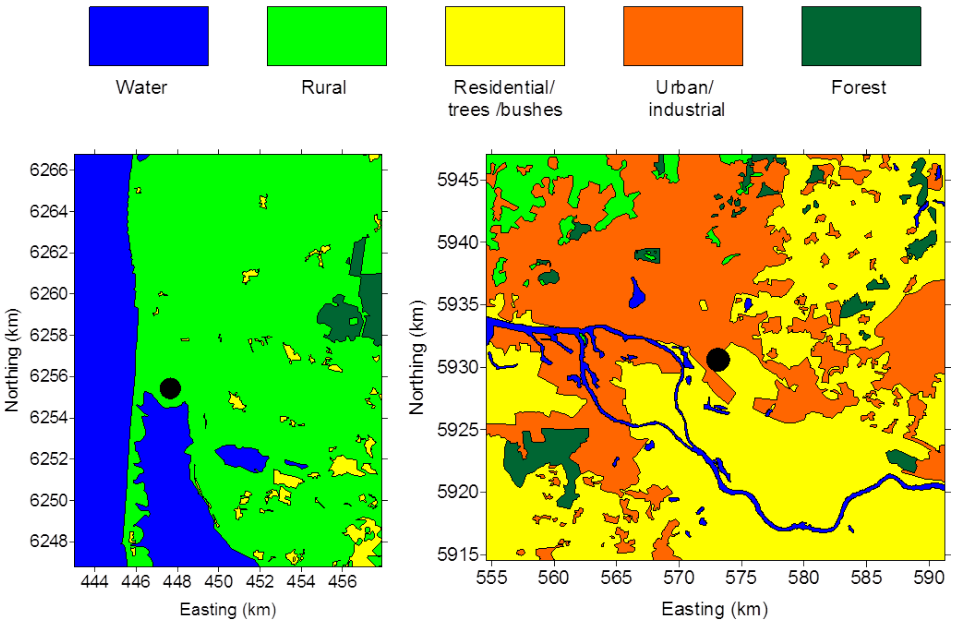

Figure 1: Maps of the areas around the Høvsøre site (left) and the Hamburg site (right). The sites are marked by circles.

2.1 The Høvsøre site

The Høvsøre site is located in a rural area approximately 2 km inland from the west coast of Denmark. Sonic and cup anemometers mounted on a meteorological mast at the site (56° 26′ 26.0″ N;08° 09′ 03.1″ E) provide flux and wind speed measurements at multiple heights from 10 m above ground level up to 116.5 m; for details see Floors et al. (2013). Wind vanes provide the wind direction at 10, 60 and 100 m. In addition a Vaisala CL31 ceilometer was operating at the site during the period we study here.

2.2 The Hamburg site

The site in Hamburg is located in a suburban area approximately 8 km south-east of the city centre. A 12 m meteorological mast at (53° 31′ 11.7″ N;10° 06′ 18.5″ E) and a TV tower 170 m to the west-south-west at (53° 31′ 09.0″ N;10° 06′ 10.3″ E) are instrumented with sonic anemometers at 10 m and at 50, 110, 175, 250 and 280 m respectively (Brümmer et al., 2012). These provide measurements of wind speed, wind direction and

turbulent fluxes. Sensors measuring the surface pressure are positioned at the site and at two locations 37 km north and 27 km north-west of it. Furthermore, as a supplement to the ground- and tower-based measurements, radiosondes were released from the Hamburg site approximately every two hours between 15 June and 20 June 2011 as part of an intensive measuring campaign. Various ceilometers at the Hamburg site provide estimates of the ABL height.

2.3 Wind LIDAR

A pulsed long-range wind LIDAR (WindCube^{TM} WLS70 by LEOSPHERE) was operating at the Høvsøre site between April 2010 and March 2011 and in Hamburg between April 2011 and April 2012. At both sites it was set up to do conical scans at an angle of 15° to zenith. Measurements of the radial wind speed were performed at four azimuth angles separated by 90° and at heights separated by 50 m. The maximum measuring height of the LIDAR depends on the atmospheric conditions and can be up to 2 km.
Time- and space-averaged values of the horizontal and vertical wind speed components are derived from the measured radial wind speeds. The transmitted pulse length is approximately 200 ns corresponding to a vertical sampling length of 50 m, and a full 360° conical scan takes around 30 s. Due to the conical scanning pattern the horizontal distance over which averages are made increases with height. For a somewhat similar LIDAR system (WindCube^{TM} WLR7 by LEOSPHERE) scanning at angle of 30° to zenith, Mikkelsen (2009) predicts the relative error on the measured wind speed induced by the spatial averaging to be around 0.5% at a height of 300 m.

3 Case studies

The two case studies presented here are based on data selected from one year of LIDAR measurements at the Høvsøre site and one week of simultaneous LIDAR and radiosonde measurements at the Hamburg site. For the large eddy simulations we use a code developed at the National Center for Atmospheric Research (NCAR) based on assumptions of a dry atmosphere and a horizontally homogeneous flow. Thus, we focus on periods with predominately clear skies and no precipitation. The homogeneity of the flow in the two case studies is discussed in the following subsections. Furthermore, we have sorted the data to find periods with positive heat flux near the surface, since convective conditions are typically handled well by LES – even at moderate grid resolution.

3.1 Høvsøre case study

In the Høvsøre case study we focus on the period between 08:00 and 13:00 CET on 6 May 2010. Figure 2 displays a weather analysis map (courtesy UK Met Office, http://www.wetterzentrale.de/archive/2010/brack/bracka20100506.gif) valid for 01:00 CET, which shows a high pressure system centered above Latvia causing easterly winds across Denmark. This agrees well with the wind direction observed at the site. A warm front located over Central and Eastern Europe is moving towards Denmark, but is presumably

too far from Høvsøre to influence the conditions at the site during the period of this case study. By choosing a case with easterly winds, we avoid the influence of the coastline west of the site. The terrain east of the site is flat and covered mainly by grass and various agricultural crops. The flow at the site can to a large extent be assumed to be horizontal homogeneous.

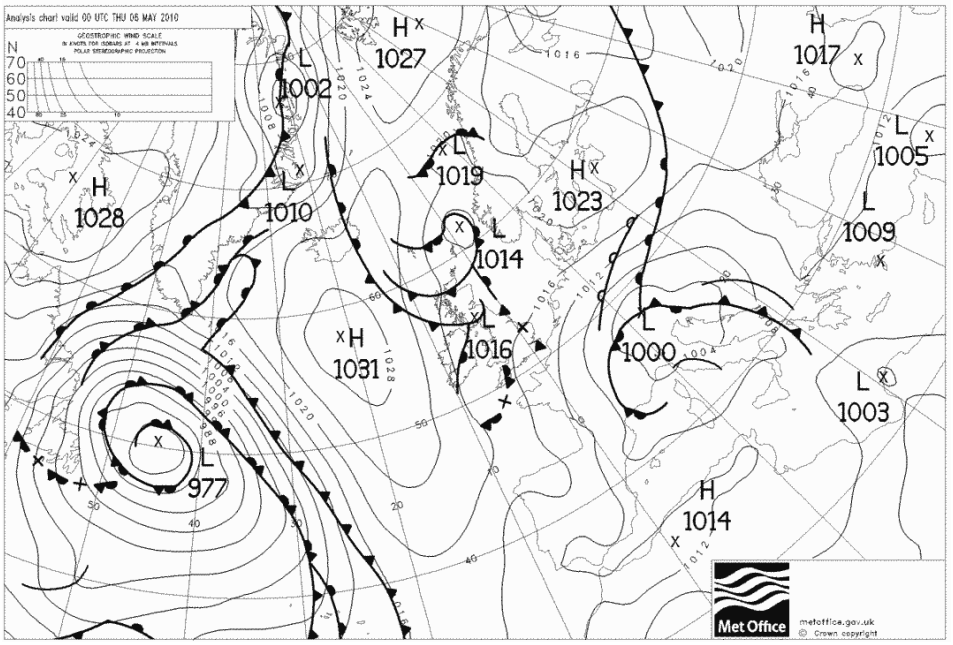

Figure 2: Met Office weather analysis chart valid at 01:00 CET on 6 May 2010 (Høvsøre case study).

The ABL height estimated from onsite ceilometer measurements increased from 600 m in the morning to 900 m in the afternoon. As the maximum measuring height of the LIDAR during the same period varied between 900 and 1600 m, we have continuous measurements of the wind speed above the ABL from which we estimate the driving pressure gradient. These measurements show a general increase of the mean wind speed during the period studied here (see figure 3). Consequently the observed wind above the ABL is not simply geostrophic, and cannot directly be translated into a pressure gradient. However, by approximating the acceleration and assuming that the only forces acting on the wind above the ABL are those arising from the pressure gradient and the rotation of the Earth (i.e. Coriolis force), we are able to estimate the effective pressure gradient and its time dependence. Moreover, a decrease with height of the observed wind speed above the ABL (see figure 3) indicates a decrease of the driving pressure gradient, suggesting baroclinic conditions. We use this information to define the domain-scale pressure gradient applied in the LESs of the Høvsøre case described in the following sections. Time series

of the measured wind speed at 250 and 750 m are shown in figure 4.

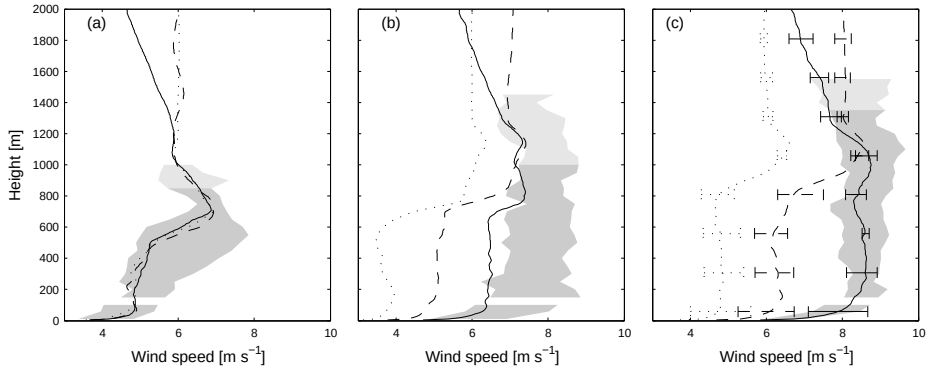

Figure 3: Simulated and measured wind speeds from the periods 8:00-9:00 (a), 10:00-11:00 (b) and 12:00-13:00 (c) of the Høvsøre case. Profiles from simulations $H\emptyset_{const}$, $H\emptyset_{t}$ and $H\emptyset_{t+z}$ are represented by dotted, dashed and solid lines. The grey areas cover wind speeds measured by LIDAR and cup anemometers.

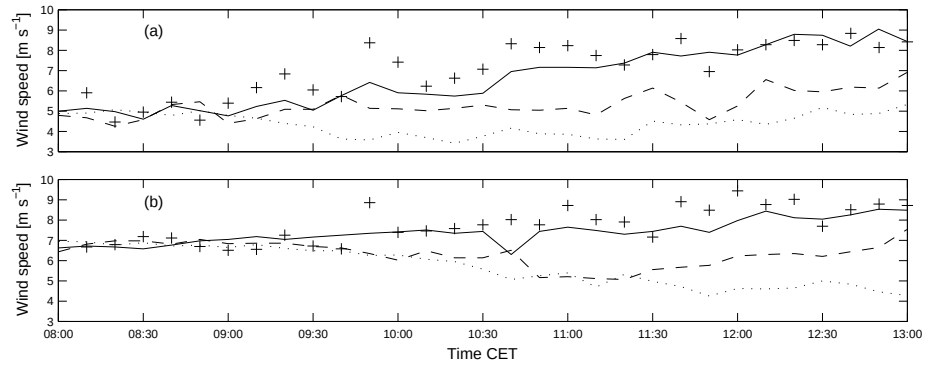

Figure 4: Time series of the wind speed at (a) 250 m and (b) 750 m from the Høvsøre case. LIDAR measurements are represented by crosses and simulated wind speed from $H\emptyset_{const}$, $H\emptyset_{t}$ and $H\emptyset_{t+z}$ by dotted, dashed and solid lines.

3.2 Hamburg case study

In the Hamburg case study we use measurements from the period between 9:00 and 15:30 CET on 15 June 2011. The UK Met Office weather analysis chart from 01:00 CET on this day (figure 5, http://www.wetterzentrale.de/archive/2011/brack/bracka20110615.gif) shows several fronts approaching Hamburg from the south-west. The two nearest are warm fronts which might have affected the conditions at the site during the period of this

case study. The observed cloud cover does, however, remain sparse during most of the period.

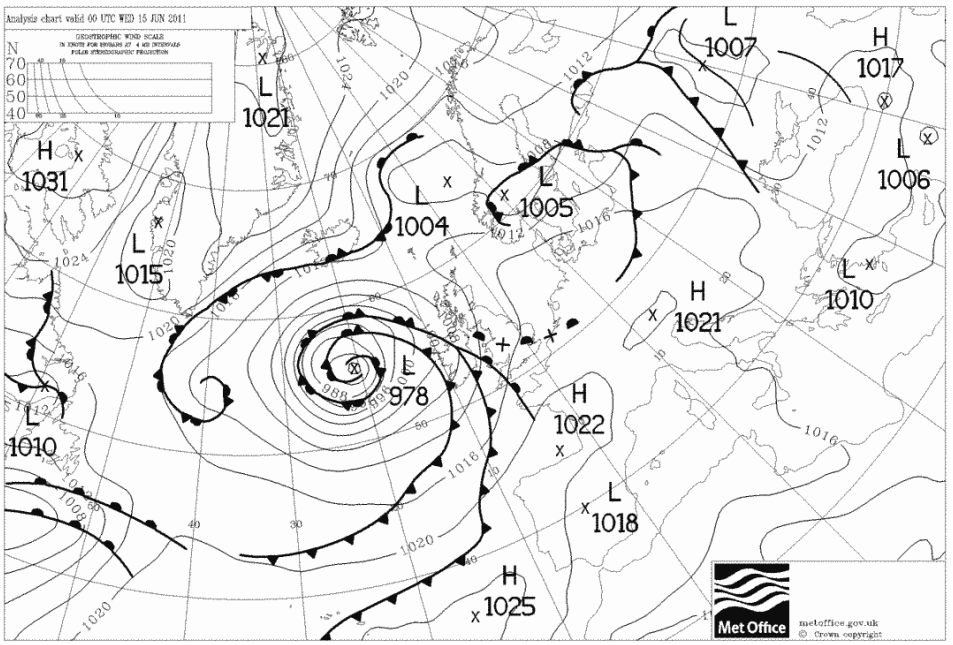

Figure 5: Met Office weather analysis chart valid at 01:00 CET on 15 June 2011 (Hamburg case study).

The chart shows an extensive area of uniform surface pressure surrounding the city of Hamburg. This is consistent with the weak pressure gradient and varying wind direction observed at the site. The mean direction of the wind at 10 m changes from 150° in the morning to 250° in the afternoon. With this change in wind direction, the area upstream of the site changes from light residential/rural to more industrial/urban (see figure 1).
The assumption of horizontal homogeneity is not as closely fulfilled as in the Høvsøre case. However, the urban/industrial sections of the upstream area consist mainly of low buildings on the order of 10 m and are less dense than the urban section north of the site. With a blending height of 1.5 to 5 times the mean obstacle height (Christen, 2005; Batchvarova and Gryning, 2006), we can assume that the individual buildings only influence the flow up to around 50 m. Detailed simulation of the urban roughness sublayer as described by e.g. Letzel et al. (2008) and Nakayama et al. (2012) is beyond the scope of this case study. We attempt to use one average roughness length for the entire upstream area.
The measured boundary layer height increased from a few hundred meters at 9:00 to 1500 m at 11:00 and 1800 m at 15:00. The relatively deep boundary layer means we have few

LIDAR measurements above it. Thus, the driving pressure gradient cannot be estimated in the same way as in the Høvsøre case. Instead we use pressure measurements from the three ground-based sensors placed around the city of Hamburg, and wind speed measurements from three radio soundings performed during the studied period.
From the network of surface pressure measurements, we derive a pressure gradient across the city, which we assume drives the flow at the site. This type of surface measurement does, however, not reveal how the pressure gradient depends on height. To address this issue, we use data from radio soundings started at 9:30, 11:05 and 13:15 CET at the Hamburg site. As the sondes reach above the ABL, they can in principle provide information about the pressure gradient in the same way as the LIDAR measurements in the Høvsøre case. The horizontal components of the wind speed inferred from the three radio soundings are shown in figure 6. Applying the same assumptions as in the Høvsøre

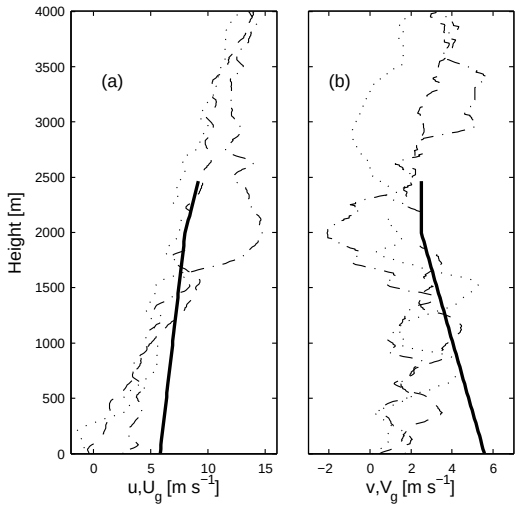

Figure 6: Initial profiles of U_g and V_g used in simulation $\mathrm{Ha}_{\mathrm{t+z}}$ (solid lines), and profiles of u and v from radio soundings at 9:30, 11:05 and 13:15 (dotted, dash-dot and dashed lines).

case, and furthermore noting that the observed wind speed above 3000 m only changes little with time, we consider it to be effectively geostrophic (directly translatable to a pressure gradient) at these heights. Combining the information from the radio soundings and the surface pressure measurements, we estimate profiles of the pressure gradient for application in the LESs of the Hamburg case described in the following sections. LIDAR measurements from the Hamburg site are shown in figure 7 and 8.

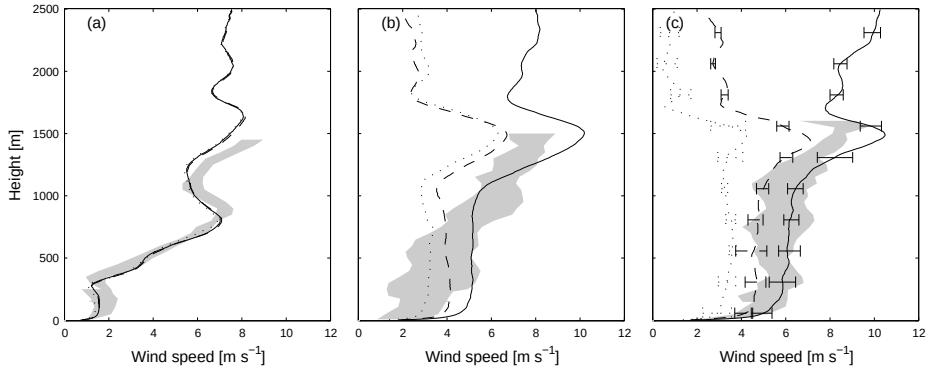

Figure 7: Simulated and measured wind speeds from the periods 9:00-10:00 (a), 12:30-13:30 (b) and 14:30-15:30 (c) of the Hamburg case. Profiles from simulations $\mathrm{Ha_{const}}$, $\mathrm{Ha_t}$, $\mathrm{Ha_{t+z}}$ are represented by dotted, dashed and solid lines. The grey areas cover wind speeds measured by LIDAR and sonic anemometers.

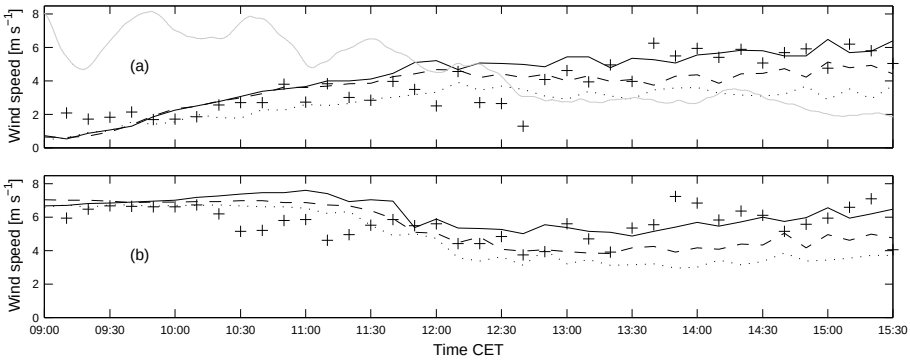

Figure 8: Time series of the wind speed at (a) 250 m and (b) 750 m from the Hamburg case. LIDAR measurements are represented by crosses and simulated wind speeds from $\mathrm{Ha_{const}}$, $\mathrm{Ha_t}$ and $\mathrm{Ha_{t+z}}$ by dotted, dashed and solid black lines. The solid grey line in (a) marks the surface value of $\left(U_g^2+V_g^2\right)^{1/2}$ applied in $\mathrm{Ha_t}$ and $\mathrm{Ha_{t+z}}$.

4 The NCAR LES code and setup of simulations

The NCAR LES code is based on Moeng (1984) and Sullivan and Patton (2011) and employs the subfilter scale model of Sullivan et al. (1994). It is pseudo spectral and surface inhomogeneities cannot be simulated.

The simulated flow is driven by a pressure gradient composed of $\left\langle \frac{\partial p}{\partial x} \right\rangle$ and $\left\langle \frac{\partial p}{\partial y} \right\rangle$. The angular brackets denote horizontal averages across the computational domain orientated with the x-axis in the west-east direction and the y-axis in the south-north direction. The

Table 1: Overview of Høvsøre (Hø) and Hamburg (Ha) simulations.

Simulation	Pressure gradient	Domain size	Grid points	Simulation period including spin-up
Hø_{const}	Constant	$6 \times 6 \times 2\,\text{km}^3$	256^3	7:30 to 13:00
Hø_{t}	Function of t	$6 \times 6 \times 2\,\text{km}^3$	256^3	7:30 to 13:00
$\text{Hø}_{\text{t+z}}$	Function of t and z	$6 \times 6 \times 2\,\text{km}^3$	256^3	7:30 to 13:00
Ha_{const}	Constant	$7.5 \times 7.5 \times 2.5\,\text{km}^3$	320^3	8:00 to 15:30
Ha_{t}	Function of t	$7.5 \times 7.5 \times 2.5\,\text{km}^3$	320^3	8:00 to 15:30
$\text{Ha}_{\text{t+z}}$	Function of t and z	$7.5 \times 7.5 \times 2.5\,\text{km}^3$	320^3	8:00 to 15:30

pressure gradient is applied as an external forcing in terms of $U_g = -\frac{1}{f\rho}\left\langle \frac{\partial p}{\partial y} \right\rangle$ and $V_g = \frac{1}{f\rho}\left\langle \frac{\partial p}{\partial x} \right\rangle$, where f is the Coriolis parameter and ρ is the air density. We will hereafter use this description of the pressure gradient. U_g and V_g can be specified as constant values or as functions of time t and/or height z.
A heat flux imposed at the lower boundary of the domain is used to calculate the surface value of the potential temperature through its value at the first grid level and Monin-Obukhov similarity.
The radiative boundary condition of Klemp and Durran (1983) is used at the top of the computational domain. A third-order Runge-Kutta scheme is used for time stepping.

4.1 Setup of simulations

For each of the two sites, Høvsøre and Hamburg, we carry out three simulations with progressively more realistic assumptions for the driving pressure gradient. Table 1 provides an overview of all the simulations.
Each simulation is initialized with specified fields of the horizontal (west-east and south-north) and vertical velocity components u, v and w and the potential temperature θ. Random divergenceless small perturbations are added to the initial fields at grid points within 50 m of the surface to help initialize the turbulent motions. The process of going from the initially non-turbulent flow to a flow with quasi-steady turbulent fluxes is called spin-up (Patton et al., 1998). In the Høvsøre and Hamburg case studies we find 0.5 and 1 hour of spin-up to be sufficient, based on the time it takes for the surface friction velocity to reach a quasi-steady state in simulations with constant forcing.
The observed humidity is in both cases generally low and the potential temperature is close to the virtual potential temperature. The influence of moisture on the wind speed is considered small and was not included in the simulations. However, intermittent appearance of clouds might have had effects which are neglected; for instance on the entrainment of air from above the ABL.

4.1.1 Høvsøre LES setup

All three Høvsøre simulations are performed in a domain of 6 km extent in the horizontal directions and 2 km in the vertical direction. This corresponds approximately to 6 and 2 times the expected maximum boundary layer height. The computational grid consists of 256 points in all three directions giving a vertical resolution of 8 m and a horizontal resolution of 23 m. The grid resolution test of Sullivan and Patton (2011) suggests that this number of grid points is sufficiently high to get accurate results. It should however be noted that the simulated ABL of Sullivan and Patton (2011) was more unstable than the one we study here, and the computational domain slightly smaller in the horizontal directions.

We apply a pressure gradient determined from observed wind speeds at altitudes above the boundary layer. From ceilometer backscatter measurements the ABL height is estimated to grow from 600 m in the morning to 900 m in the afternoon. Assuming the flow above the boundary layer is non-turbulent and horizontally homogenous, the averaged horizontal momentum equations can be reduced to:

$$\begin{aligned} \frac{\partial \langle u \rangle}{\partial t} &= f\left(\langle v \rangle - V_g\right) \\ \frac{\partial \langle v \rangle}{\partial t} &= f\left(U_g - \langle u \rangle\right). \end{aligned} \tag{1}$$

In the $\text{H}\emptyset_{\text{const}}$ simulation we furthermore assume the flow in the free atmosphere above the ABL to be stationary, i.e. $\frac{\partial \langle u \rangle}{\partial t} = \frac{\partial \langle v \rangle}{\partial t} = 0$, and we set:

$$\begin{aligned} U_g &= \langle u \rangle_0 = -6\,\text{ms}^{-1} \\ V_g &= \langle v \rangle_0 = 0\,\text{ms}^{-1}. \end{aligned}$$

$\langle u \rangle_0$ and $\langle v \rangle_0$ represent the mean wind speed components around the time 8:30 corresponding to $t = 0$, where t is the simulation time minus one hour. All three Høvsøre simulations are in effect started at 7:30 to allow for a 0.5 hour spin-up period and for subsequent averaging over the period between 8:00 and 9:00. The used values for $\langle u \rangle_0$ and $\langle v \rangle_0$ are based on the observed mean wind speed above 600 m taken as an hourly average of the LIDAR measurements between 8:00 and 9:00 shown in figure 3 (a). The pressure gradient is in this simulation assumed to be constant with height representing barotropic conditions.

In general, however, the forces driving the flow of the ABL cannot be assumed to be stationary, and during the period studied here we do in fact also see variation of the observed mean wind speed above the ABL. More specifically, the u-component is observed to decrease from $-6\,\text{ms}^{-1}$ in the morning to $-8\,\text{ms}^{-1}$ in the afternoon (see figure 3 (a) and (c)). The v-component remains close to $0\,\text{ms}^{-1}$. In the $\text{H}\emptyset_{\text{t}}$ and $\text{H}\emptyset_{\text{t+z}}$ simulations we take this into account by assuming that above the ABL, $\langle u \rangle$ decreases linearly at a rate of $1.4 \cdot 10^{-4}\,\text{ms}^{-2}$ and $\langle v \rangle$ stays constant. Based on equation 1 this leads to:

$$\begin{aligned} U_g &= \langle u \rangle_0 - 1.4 \cdot 10^{-4}\,\text{ms}^{-2} \cdot t \\ V_g &= \langle v \rangle_0 + 1.4 \cdot 10^{-4}\,\text{ms}^{-2} \cdot f^{-1}. \end{aligned}$$

In the Hø_t simulation we assume barotropic conditions with U_g and V_g being constant with height, and as in the Hø_const simulation we use $\langle u \rangle_0 = -6\,\text{ms}^{-1}$ and $\langle v \rangle_0 = 0\,\text{ms}^{-1}$.
In the $\text{Hø}_{\text{t+z}}$ simulation we assume baroclinic conditions with both U_g and V_g varying with height. The height variation is like the time variation estimated from the observed mean wind above the ABL. The estimated tendency above the ABL is extended to the surface and we use:

$$\langle u \rangle_0 = -8\,\text{ms}^{-1} + z \cdot 0.002\,\text{s}^{-1}$$
$$\langle v \rangle_0 = \begin{cases} 3\,\text{ms}^{-1} - z \cdot 0.003\,\text{s}^{-1} & \text{for } z < 1000\text{ m} \\ 0\,\text{ms}^{-1} & \text{for } z > 1000\text{ m} \end{cases}$$

The height dependence of U_g and V_g is kept constant during the simulation period in approximate agreement with LIDAR measurements. We do not show measured profiles of the individual wind speed components, but since the wind was mainly from the east and the direction only changed little with height, the height dependence of U_g can to a large extent be derived from the measurements of the wind speed shown in figure 3. The applied height dependence of V_g is most clearly seen from measurements between 8:00 and 9:00, but for simplicity we maintain it throughout the simulation.
In all three Høvsøre simulations we use an initial profile of the potential temperature given by:

$$\theta = \begin{cases} 280\,\text{K} & \text{for } z < 550\text{ m} \\ 280\,\text{K} + (z - 550\,\text{m}) \cdot 0.025\,\text{Km}^{-1} & \text{for } 550\,\text{m} < z < 650\,\text{m} \\ 282.5\,\text{K} + (z - 650\,\text{m}) \cdot 0.0034\,\text{Km}^{-1} & \text{for } z > 650\text{ m} \end{cases}$$

We have no measurements of either temperature or pressure above 100 m, so the chosen profile is merely based on an assumption of a perfectly mixed layer up to 550 m capped by an inversion of 2.5 K between 550 and 650 m. Above the inversion we assume the potential temperature to increase at $0.0034\,\text{Km}^{-1}$ which is considered as a typical value in the free atmosphere.
The initial profiles of u and v are chosen such that the averaged profiles between 0.5 and 1.5 hours of simulation time match the observed wind speed components averaged between 8:00 and 9:00. At heights above the range of the LIDAR, the averaged profiles of u and v match the specified values of $\langle u \rangle_0$ and $\langle v \rangle_0$.
The heat flux applied at the lower boundary is set to follow the heat flux measured at 10 m which varies around $0.075\,\text{Kms}^{-1}$ during the whole period as seen in figure 9. It is updated every time step using linear interpolation between measurements. The surface roughness length is set to 0.02 m (Gryning et al., 2007) and the Coriolis parameter to $1.21 \cdot 10^{-4}\,\text{s}^{-1}$.

4.1.2 Hamburg LES setup

For the Hamburg simulations, we use a computational domain of $7.5 \times 7.5 \times 2.5\,\text{km}^3$ with 320 grid points in each direction. This gives the same resolution as in the Høvsøre simulations. A deeper boundary layer necessitates the bigger domain.
We apply a surface heat flux inferred from the measurements at 10 m shown in figure 9,

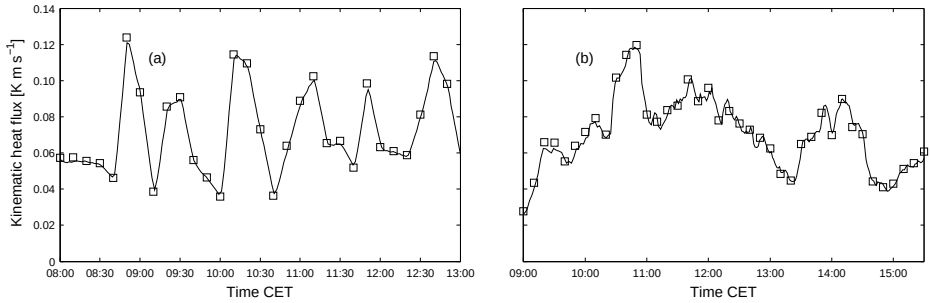

Figure 9: Kinematic heat flux measured at 10 m (squares) at the Høvsøre (a) and Hamburg (b) sites. The lines represent heat flux extracted from the lowest level of grid points in simulations $\mathrm{Hø_{t+z}}$ (a) and $\mathrm{Ha_{t+z}}$ (b).

and use a roughness length of 0.6 m (Gryning et al., 2007). The Coriolis parameter is set to $1.16 \cdot 10^{-4}\,\mathrm{s}^{-1}$. As for the Høvsøre case, we perform three simulations with the applied pressure gradient being constant ($\mathrm{Ha_{const}}$), time dependent ($\mathrm{Ha_t}$) and time and height dependent ($\mathrm{Ha_{t+z}}$).

In the $\mathrm{Ha_{const}}$ simulation we assume, that the pressure gradient is equal to its surface value at all heights, and keep it constant with time. It is specified to match the mean of the observed pressure gradient across the city between 9:00 and 15:30. This leads to $U_g = 3.5\,\mathrm{ms}^{-1}$ and $V_g = 2.4\,\mathrm{ms}^{-1}$.

In the $\mathrm{Ha_t}$ simulation we keep the pressure gradient constant with height, but let it change with time as shown in figure 8 (a). It is updated every time step following the observed pressure gradient.

In the $\mathrm{Ha_{t+z}}$ simulation we assume baroclinic conditions. The pressure gradient is kept constant with time in the top part of the domain with U_g and V_g based on values of u and v from radio soundings started at 9:30, 11:05 and 13:15. We use observations from heights above 3000 m where the wind speed varies only little with time, and we can assume geostrophic balance. U_g is set to increase linearly from $8\,\mathrm{ms}^{-1}$ at 2000 m to $9.25\,\mathrm{ms}^{-1}$ at 2500 m. V_g is kept constant at $2.5\,\mathrm{ms}^{-1}$ in the same region. From 2000 m to the surface U_g and V_g are set to vary linearly to the time-varying values of the pressure gradient used in the $\mathrm{Ha_t}$ simulation. Figure 6 shows wind speed components from the three radio soundings and the profiles of U_g and V_g at the beginning of simulation $\mathrm{Ha_{t+z}}$.

The initial profiles of u, v and θ of the Hamburg LES runs are chosen, such that the profiles averaged between 1 and 2 hours of simulation time approximately match values from the radio sounding started at 9:30.

5 Results

In this section we present results of the LESs described in section 4 and compare them to measurements. The simulated wind speeds shown here are taken from a vertical column of grid points in the centre of the computational domain. As the measured wind speeds,

they are averaged over 10 minute periods.
From the Høvsøre site we use cup anemometer measurements up to 100 m, and from the Hamburg site sonic anemometer measurements up to 250 m. We present wind LIDAR measurements up to heights between 900 and 1600 m. LIDAR measurements with data availability less than 70% are discarded.

5.1 Høvsøre results

Figure 3 shows wind speeds from simulations Hø_{const} (dotted lines), Hø_{t} (dashed lines) and $\text{Hø}_{\text{t+z}}$ (solid lines) from the periods between 0.5 and 1.5, 2.5 and 3.5, and 4.5 and 5.5 hours of simulation time. The lines are 1-hour averaged profiles composed by six 10-minute profiles. The error bars in figure 3 (c) indicate the minimum and maximum 10-minute values at selected heights. These are left out in figure 3 (a) and (b) to give a more clear view of the mean profiles.
The grey areas cover the range of 10-minute averaged wind speeds measured by cup anemometers and LIDAR during the hours between 8:00 and 9:00, 10:00 and 11:00, and 12:00 and 13:00. We only show LIDAR measurements up to heights, where six 10-minute values are available per hour. The accuracy of wind speeds measured by LIDAR decreases with the Carrier to Noise ratio (CNR). Measurements with CNR higher than -30 dB are shown in dark grey, while measurements with CNR between -30 and -40 dB are shown in light grey. Cup anemometers provide the scalar wind speed. For consistency, we also present LIDAR measurements and LES wind speeds in terms of scalar averages. That is, averages over series of instantaneous or nearly instantaneous observations of the wind speed. This type of average differs from the vector average which consists of averaged values of the individual horizontal wind speed components (Brower, 2012). In cases like this one, however, with only little variance in the wind direction the two types of averages will be quite close. Figure 4 shows time series of measured and simulated wind speeds at heights of 250 and 750 m during the period between 8:00 and 13:00.
The Hø_{const}-simulation generally agrees poorly with measurements, and underestimates the wind speed by up to $4\,\text{ms}^{-1}$ ($\sim 50\%$) after 5 hours of simulation time. The agreement is improved by the time-dependence of the pressure gradient included in the Hø_{t} simulation. In particular, we see fair agreement between simulated and measured wind speeds above the ABL. This is, however, expected since the simulated wind speed in this region is almost directly proportional to the applied pressure gradient, which was determined from the observed wind. Within the ABL, the wind speed is still clearly underestimated.
The observed wind speed above the ABL decreases with height, as seen in figure 3 (a) above 600 m and in figure 3 (b) and (c) above 1000 m. Adding a height dependence to the pressure gradient, corresponding to what is observed, further improves the agreement between simulation ($\text{Hø}_{\text{t+z}}$) and measurements. In the period between 12:00 and 13:00 (figure 3 (c)) the agreement is good at nearly all heights. Before 11:00, too little vertical mixing and too slow of an increase of the pressure gradient seem to cause an underestimation of the wind speed in the ABL. This is indicated both by the shape of the simulated wind speed profile in figure 3 (b) and the time series of the wind speed at 250 m in figure 4 (a). The wind speed at 750 m (figure 4 (b)) from simulation $\text{Hø}_{\text{t+z}}$ follows the general trend of the measured wind speed, but with less variation. The surface friction velocity u_*

Table 2: Mean absolute errors and root-mean-square errors between LIDAR measurements and simulation results shown in figure 4 (Høvsøre case study).

	$H\emptyset_{const}$		$H\emptyset_{t}$		$H\emptyset_{t+z}$	
Height [m]	250	750	250	750	250	750
MAE [ms^{-1}]	2.8	2.2	1.8	1.5	0.7	0.6
RMSE [ms^{-1}]	3.1	2.7	2.1	1.9	0.8	0.7

is shown in figure 10, and it is in all three simulations within the scatter of the measured values.
The mean absolute error (MAE) and the root-mean-square error (RMSE) between the simulated data points in figure 4 and the equivalent measurements are given in table 2. The MAE and RMSE are calculated as:

$$MAE = N^{-1} \sum_{i=1}^{N} |LIDAR_i - LES_i|$$

$$RMSE = \left(N^{-1} \sum_{i=1}^{N} (LIDAR_i - LES_i)^2 \right)^{0.5},$$

where N is the number of data points and $LIDAR_i$ and LES_i are wind speeds from the LIDAR and LES respectively.

5.2 Hamburg results

Figure 7 shows wind speeds from simulations Ha_{const} (dotted lines), Ha_{t} (dashed lines) and Ha_{t+z} (solid lines) from the periods between 1 and 2, 4.5 and 5.5, and 6.5 and 7.5 hours of simulation time. As in figure 3, the lines are 1-hour averaged profiles composed by six 10-minute profiles. The grey areas cover wind speeds measured by sonic anemometers and LIDAR during the hours between 9:00 and 10:00, 12:30 and 13:30, and 14:30 and 15:30. The LIDAR measurements have a CNR above –30 dB.
In this case, the measured wind direction exhibits high variance due to the low wind speed and complex surroundings. Consequently we see a significant difference between scalar and vector averages of the measured wind speed. With this in mind, the following results are presented in terms of vector averages. Figure 8 shows time series of measured and simulated wind speeds at heights of 250 and 750 m during the period between 9:00 and 15:30.
The results from the Hamburg case are not as clear as those from the Høvsøre case. The importance of including variations in time of the driving pressure gradient is, however, illustrated by the difference between the simulated profiles in figure 7 (c). The Ha_{const}-simulation clearly underestimates the wind speed, while the profile from the Ha_{t}-simulation almost falls within the range measured profiles. Simulation Ha_{t+z} shows the best agreement with measurements in the period between 14:30 and 15:30, which suggests that baroclinity also plays an important role in this case. However, as evident from

Table 3: Mean absolute errors and root-mean-square errors between LIDAR measurements and simulation results shown in figure 8 (Hamburg case study).

	Ha_{const}		Ha_t		Ha_{t+z}	
Height [m]	250	750	250	750	250	750
MAE [ms^{-1}]	1.3	1.4	0.9	1.0	0.9	1.0
RMSE [ms^{-1}]	1.5	1.8	1.2	1.3	1.2	1.2

both figure 7 (b) and figure 8 (a) and (b), the Ha_{t+z}-simulation generally overestimates the wind speed in the lowest part of the domain – especially between 11:00 and 13:30. Values of the MAE and the RMSE between the simulated data points in figure 8 and the equivalent measurements are shown in table 3.

We suspect the specified vertical gradient of the forcing is too large near the surface. In fact we do not have any information about how the pressure gradient varies with height through the ABL. Assuming $\frac{\partial\left(\left\langle\frac{\partial p}{\partial x}\right\rangle,\left\langle\frac{\partial p}{\partial y}\right\rangle\right)}{\partial z}$ itself changes with height, measurements of either the horizontal temperature gradient or the horizontal pressure gradient as function of height are needed.

The surface friction velocity shown in figure 10 is in all three simulations quite close to the measured values, but especially in Ha_{t+z} somewhat overestimated.

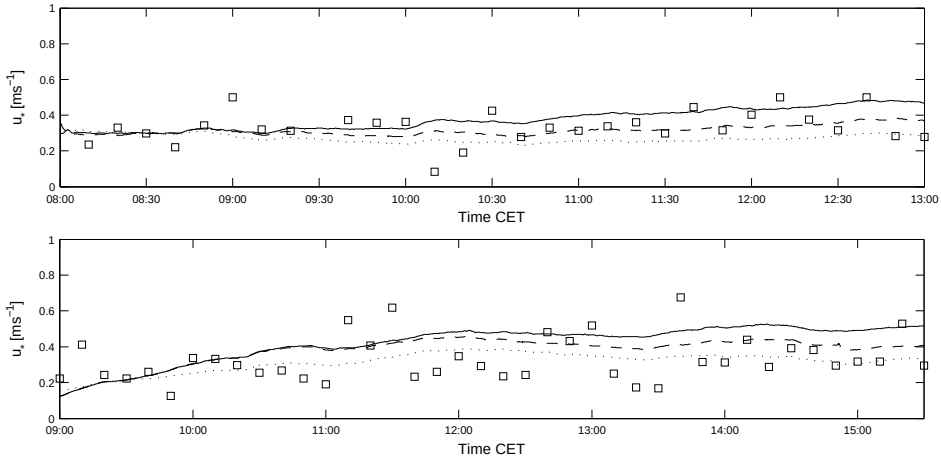

Figure 10: Time series of the measured and simulated friction velocities from the Høvsøre case (top) and Hamburg case (bottom). Tower measurements at 10 m are represented by squares and simulated values from $Hø_{const}$/Ha_{const}, $Hø_t$/Ha_t and $Hø_{t+z}$/Ha_{t+z} at the grid levels closest to 10 m by dotted, dashed and solid black lines.

5.3 Temperature effects

Figure 11 shows measurements of potential temperature acquired by radiosondes started at 9:30, 11:05 and 13:15 from the Hamburg site and corresponding profiles from simulation Ha_{t+z}.

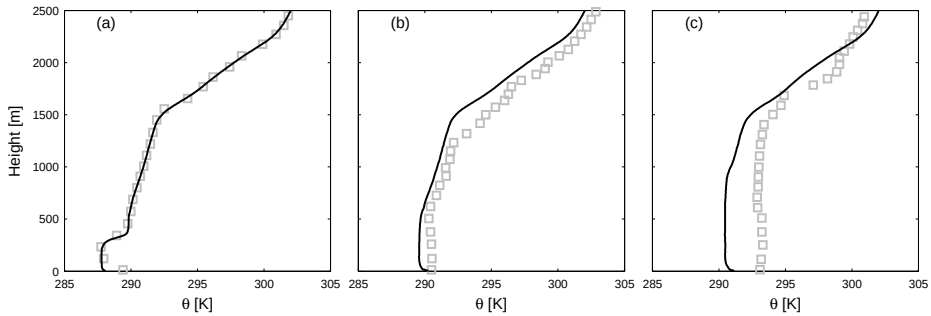

Figure 11: Potential temperature profiles from the Hamburg case. Markers represent radio soundings started at 9:30 (a), 11:05 (b) and 13:15 (c). The solid lines are ten-minute profiles from simulation Ha_{t+z} at corresponding times.

Due to the choice of initial conditions, the simulated temperature at 9:30 matches the radio sounding quite well, but at 11:05 the LES temperatures are too cold above the ABL (i.e. above 1500 m). Moreover, the ceilometer measurements show a decrease in the ABL height between 10:00 and 12:00 which points toward a lack of large scale subsidence in the LES. As described by e.g. Batchvarova and Gryning (1994) and Mirocha and Kosović (2010) subsidence can reduce or even counteract the growth of the ABL.
During most of the period studied here, the tower-based temperature measurements show a faster increase than the simulated temperature even though the surface heat flux applied in the LES matches the measured heat flux, and compared to the radio sounding at 13:15 the simulated temperature is a few degrees too low throughout the ABL. This suggests advection of warm air, not included in the LES. Moreover, the vertical gradient of the simulated temperature above the ABL also agrees poorly with the radio sounding. The influence of the ABL height and the free atmosphere temperature gradient on the wind speed within the ABL is discussed in the papers of Gryning et al. (2007) and Zilitinkevich and Esau (2005). However, the lengthy periods between the available radio soundings, and the apparently transient nature of the phenomena causing the observed temperature discrepancies, make them difficult to quantify and simulate.
In the Høvsøre case the simulated temperatures generally follow the tower-based measurements quite well. Unfortunately we have no measurements above 100 m in this case. The height dependence of the driving pressure gradient is related to large-scale horizontal temperature gradients through the thermal wind equations. In simulations $\mathrm{Hø}_{t+z}$ and Ha_{t+z}, the applied baroclinic shear corresponds to a horizontal temperature gradient on the order of $1 \cdot 10^{-5}\,\mathrm{Km}^{-1}$, which is a typical value (Arya and Wyngaard, 1975). The associated advection of cold or warm air across the domain was not included in the sim-

ulations, since the effect on the simulated temperature would be small compared to e.g. the observed differences between the simulated temperature profiles and radio soundings in the Hamburg case.

6 Discussion

In the two case studies from Høvsøre and Hamburg we use LIDAR and radiosonde measurements, respectively, of the wind speed above the ABL to estimate the driving pressure gradient; in the Hamburg case as a supplement to ground-based measurements of the surface pressure gradient.
However, whereas the LIDAR provide measurements every 10 seconds from which a mean value over a longer period can be calculated, the radio soundings only provide nearly instantaneous measurements 1.5 and 2 hours apart. The mean ascent rates of the sondes are between 4 and 5 ms^{-1}, which means that the obtained wind profiles plotted in figure 6 essentially cover 800-1000 second periods. They can nevertheless not be considered as average profiles, since the sondes only spend an instant at each measuring height. Thus, the pressure gradient inferred from these in the Hamburg case is associated with higher uncertainty than that inferred from the averaged LIDAR profiles in the Høvsøre case.
An alternative approach to gain information about the pressure gradient for driving a realistic LES, is to use data from a mesoscale model such as WRF (Skamarock et al., 2008). This approach is used by e.g. Lundquist et al. (2010); Talbot et al. (2012); Rizza et al. (2013) and was considered for the Hamburg case study. However, since the surface pressure gradient derived from the pressure fields of the available WRF forecast fits poorly with the observed surface pressure gradient, we chose not to use the WRF pressure gradient

7 Conclusion

At present, LES of the ABL is in most cases still confined to computational domains of only a few kilometers extent in each direction, with constant forcing. This means that phenomena acting on larger scales are not modelled. In the simulations presented here we account for such phenomena by including temporal and spatial variations of the external forcing applied in terms of a mean pressure gradient across the computational domain.
In two case studies from Høvsøre and Hamburg, we have estimated the pressure gradient from measurements of the wind speed above the ABL and from measurements of surface air pressure. At both sites we see variations in the pressure gradient with both time and height.
The effect on the wind speed of these variations is investigated by performing simulations with the forcing being constant ($\mathrm{Hø}_{\mathrm{const}}$ and $\mathrm{Ha}_{\mathrm{const}}$), time-dependent ($\mathrm{Hø}_{\mathrm{t}}$ and Ha_{t}) and both time- and height-dependent ($\mathrm{Hø}_{\mathrm{t+z}}$ and $\mathrm{Ha}_{\mathrm{t+z}}$).
In the Høvsøre case study we find that accurate specification of both height- and time-dependence of the pressure gradient driving the flow is necessary to obtain good agree-

ment between measured and simulated wind profiles.
In the Hamburg case, the effect of including the time dependence alone in the LES only improves the agreement between simulated and measured wind speeds towards the end of the simulation period. Including also the assumed height dependence generally improves the agreement above 1000 m, but causes an overestimation of the wind speed below. We take this as an indication that the vertical gradient of the pressure gradient within the ABL is not constant with height, but decreases near the surface. However, it must be concluded that the measurements available in this case study are not sufficient to accurately estimate the effective baroclinicity.
In the Hamburg case, we furthermore see differences between measured and simulated profiles of potential temperature, caused by large scale subsidence and advection not accounted for in the LES. More frequent radio soundings would help us to include such phenomena and study their influence on the wind speed.
With increasing computer power LES of realistic atmospheric flows is likely to become more common in the future with applications including assessment of wind resources and turbulence characteristics at potential sites for energy production (Emeis, 2012) and prediction of pollutant dispersion in cities. As the work presented here illustrates, careful treatment of spatially and temporally varying forcing can be essential for obtaining accurate results.

Acknowledgements

The study was supported by the Danish Council for Strategic Research, project number 2104-08-0025 named “Tall Wind”. We would like to thank the Test and Measurements section of DTU Wind Energy for the maintenance of the Høvsøre database.

References

Arya, S. P. (2001). *Introduction to micrometeorology*. Academic Press, San Diego.

Arya, S. P. S. and Wyngaard, J. C. (1975). Effect of baroclinicity on wind profiles and the geostrophic drag law for the convective planetary boundary layer. *J. Atmos. Sci.*, 32:767–778.

Basu, S., Vinuesa, J.-F., and Swift, A. (2008). Dynamic LES Modeling of a Diurnal Cycle. *J. Appl. Meteor. Climatol.*, 47:1156–1174.

Batchvarova, E. and Gryning, S.-E. (1994). An applied model for the height of the daytime mixed layer and the entrainment zone. *Bound.-Layer Meteor.*, 71:311–323.

Batchvarova, E. and Gryning, S.-E. (2006). Progress in urban dispersion studies. *Theor. Appl. Climatol.*, 84:57–67.

Beare, R. J., MacVean, M. K., Holtslag, A. A. M., Cuxart, J., Esau, I., Golaz, J.-C., Jimenez, M. A., Khairoutdinov, M., Kosović, B., Lewellen, D., Lund, T. S., Lundquist,

J. K., McCabe, A., Moene, A. F., Noh, Y., Raasch, S., and Sullivan, P. (2006). An intercomparison of large-eddy simulations of the stable boundary layer. *Bound.-Layer Meteor.*, 118:247–272.

Brower, M. C. (2012). *Wind resource assessment: A practical guide to developing a wind project*. Wiley.

Brümmer, B., Lange, I., and Konow, H. (2012). Atmospheric boundary layer measurements at the 280 m high hamburg weather mast 1995-2011: mean annual and diurnal cycles. *Meteorol. Z.*, 21:319–335.

Christen, A. (2005). *Atmospheric turbulence and surface energy exchange in urban environments - Results from the Basel Urban Boundary Layer Experiment (BUBBLE)*. University of Basel.

Clarke, R. H., Brook, R. R., Reid, D. G., and Troup, A. J. (1971). *The Wangara experiment: Boundary layer data*. C.S.I.R.O, Melbourne.

Deardorff, J. W. (1970). Preliminary results from numerical integrations of the unstable planetary boundary layer. *J. Atmos. Sci.*, 27:1209–1211.

Deardorff, J. W. (1972). Numerical investigation of neutral and unstable planetary boundary layers. *J. Atmos. Sci.*, 29:91–115.

Deardorff, J. W. (1974). Three-dimensional numerical study of the height and mean structure of a heated planetary boundary layer. *Bound.-Layer Meteor.*, 7:81–106.

Emeis, S. (2012). *Wind energy meteorology*. Springer-Verlag Berlin Heidelberg, Berlin.

Floors, R., Vincent, C. L., Gryning, S.-E., Peña, A., and Batchvarova, E. (2013). The wind profile in the coastal boundary layer: Wind lidar measurements and numerical modelling. *Bound.-Layer Meteor.*, 147:469–491.

Gryning, S.-E., Batchvarova, E., Brümmer, B., Jørgensen, H., and Larsen, S. (2007). On the extension of the wind profile over homogeneous terrain beyond the surface boundary layer. *Bound.-Layer Meteor.*, 124:251–268.

Kelly, M. and Gryning, S.-E. (2010). Long-term mean wind profiles based on similarity theory. *Bound.-Layer Meteor.*, 136:377–390.

Klemp, J. B. and Durran, D. R. (1983). An upper boundary condition permitting internal gravity wave radiation in numerical mesoscale models. *Mon. Wea. Rev.*, 111:430–444.

Kosović, B. and Curry, J. A. (2000). A large eddy simulation study of a quasi-steady, stably stratified atmospheric boundary layer. *J. Atmos. Sci.*, 57:1052–1068.

Kumar, V., Svensson, G., Holtslag, A. A. M., Meneveau, C., and Parlange, M. B. (2010). Impact of Surface Flux Formulations and Geostrophic Forcing on Large-Eddy Simulations of Diurnal Atmospheric Boundary Layer Flow. *J. Appl. Meteor. Climatol.*, 49:1496–1516.

Letzel, M. O., Krane, M., and Raasch, S. (2008). High resolution urban large-eddy simulation studies from street canyon to neighbourhood scale. *Atmos. Environ.*, 42:8770–8784.

Lundquist, J. K., Mirocha, J. D., and Kosović, B. (2010). Nesting large-eddy simulations within mesoscale simulations in WRF for wind energy applications. In *Proceedings of the Fifth International Symposium on Computational Wind Engineering*, Chapel Hill, NC.

Mikkelsen, T. (2009). On mean wind and turbulence profile measurements from ground-based wind lidars: limitations in time and space resolution with continuous wave and pulsed lidar systems. In *European Wind Energy Conference and Exhibition*, Marseille, FR.

Mirocha, J. D. and Kosović, B. (2010). A large-eddy simulation study of the influence of subsidence on the stably stratified atmospheric boundary layer. *Bound.-Layer. Meteor.*, 134:1–21.

Moeng, C.-H. (1984). A Large-Eddy-Simulation Model for the Study of Planetary Boundary-Layer Turbulence. *J. Atmos. Sci.*, 41:2052–2062.

Moeng, C.-H. and Sullivan, P. P. (1994). A Comparison of Shear- and Buoyancy-Driven Planetary Boundary Layer Flows. *J. Atmos. Sci.*, 51:999–1022.

Nakayama, H., Takemi, T., and Nagai, H. (2012). Large-eddy simulation of urban boundary-layer flows by generating turbulent inflows from mesoscale meteorological simulations. *Atmos. Sci. Lett.*, 13:180–186.

Patton, E. G., Shaw, R. H., Judd, M. J., and Raupach, M. R. (1998). Large-eddy simulation of windbreak flow. *Bound.-Layer Meteor.*, 87:275–306.

Rizza, U., Miglietta, M. M., Acevedo, O. C., Anabor, V., Degrazia, G. A., Goulart, A. G., and Zimmerman, H. R. (2013). Large-eddy simulation of the planetary boundary layer under baroclinic conditions during daytime and sunset turbulence. *Meteorol. Appl.*, 20:56–71.

Schmidt, H. and Schumann, U. (1989). Coherent structure of the convective boundary layer derived from large-eddy simulations. *J. Fluid Mech.*, 200:511–562.

Skamarock, W., Klemp, J. B., Dudhia, J., Gill, D. O., Barker, D. M., Duda, M. G., Huang, X.-Y., and Wang, W. (2008). *A description of the Advanced Research WRF Version 3*. University Corporation for Atmospheric Research, Boulder.

Sullivan, P. P., McWilliams, J. C., and Moeng, C.-H. (1994). A subgrid-scale model for large-eddy simulation of planetary boundary-layer flows. *Bound.-Layer Meteor.*, 71:247–276.

Sullivan, P. P., Moeng, C. H., Stevens, B., Lenschow, D. H., and Mayor, S. D. (1998). Structure of the entrainment zone capping the convective atmospheric boundary layer. *J. atmos. Sci.*, 55:3042–3064.

Sullivan, P. P. and Patton, E. G. (2011). The effect of mesh resolution on convective boundary layer statistics and structures generated by large-eddy simulation. *J. Atmos. Sci.*, 68:2395–2415.

Talbot, C., Bou-Zeid, E., and Smith, J. (2012). Nested mesoscale large-eddy simulations with WRF: Performance in real test cases. *J. Hydrometeor.*, 13:1421–1441.

Zilitinkevich, S. S. and Esau, I. N. (2005). Resistance and heat-transfer laws for stable and neutral planetary boundary layers: Old theory advanced and re-evaluated. *Quart. J. Roy. Meteor. Soc.*, 131:1863–1982.

PAPER II:
ON THE STRUCTURE AND DEVELOPMENT OF INVERSION-CAPPED NEUTRAL ATMOSPHERIC BOUNDARY LAYERS: A LARGE-EDDY SIMULATION STUDY

On the structure and development of inversion-capped neutral atmospheric boundary layers: A large-eddy simulation study

Jesper Grønnegaard Pedersen, Sven-Erik Gryning, Mark Kelly

DTU Wind Energy, Risø Campus, Technical University of Denmark, DK-4000 Roskilde, Denmark

Submitted to Boundary-Layer Meteorology

Abstract

A range of large-eddy simulations, with differing free-atmosphere stratification and zero or slightly positive surface heat flux, is investigated to improve understanding of the neutral and near-neutral, inversion-capped, horizontally homogeneous, barotropic atmospheric boundary layer, especially the upper part. We find that an adjustment time of at least 16 hours, corresponding to the period of the inertial oscillation, is needed for the simulated flow to reach a quasi-steady state. The boundary layer continues to grow, but at a slow rate which changes little after 8 hours of simulation time. A common feature of the neutral simulations is the development a super-geostrophic jet near the top of the boundary layer. The analytical wind shear models included in this study do not account for such a jet, and the best agreement with simulated wind shear is seen in cases with weak stratification above the boundary layer. Increasing the surface heat flux decreases the jet size and leads to better agreement between analytical and simulated wind speed profiles. Over a range of different inversion strengths and surface heat fluxes, we also find good agreement between the performed simulations and models of the equilibrium boundary-layer height, and of the budget of turbulent kinetic energy integrated across the boundary layer.

1 Introduction

As pointed out by Hess (2004), today there are few experimental observations available to investigate the flow of the inversion-capped, steady-state, horizontally homogeneous, neutrally stratified, barotropic atmospheric boundary layer (ABL). The strict requirement of a non-accelerating mean flow with no advection effects or surface heat flux—and a driving pressure gradient which is constant in both time and height—is rarely fulfilled. In this paper, we continue along the lines of e.g. Moeng and Sullivan (1994) and Zilitinkevich and Esau (2005), utilizing large-eddy simulation (LES) to improve our understanding of

the upper part of such an idealized ABL, also referred to as the "conventionally neutral" (CN) ABL (Zilitinkevich and Esau, 2005). For comparison, the "truly neutral" ABL, i.e. the neutral ABL developing against a neutrally stratified free atmosphere (Zilitinkevich and Esau, 2005) was simulated by Mason and Thomson (1987). They obtained a wind profile which is significantly different from that of Moeng and Sullivan (1994). Other LES studies of the neutral ABL include Andren et al. (1994), Kosović (1997), Otte and Wyngaard (2001) and Mirocha et al. (2013).
The study presented here is to a large extent motivated by the prospect of extending the use of LES to still more realistic applications as discussed by Sullivan and Patton (2011). In such applications, potentially also including the influence of diurnal variations (Basu et al., 2008; Kumar et al., 2010), a clear understanding of the LES "spin-up" process is important. To determine when an LES is adequately developed, we examine the adjustment to statistically steady fully turbulent ABL flow in a horizontally homogeneous computational domain with periodic lateral boundary conditions. The height of the fully developed CN ABL is compared to the model of Zilitinkevich et al. (2012).
Furthermore, we look at the competing influences of the free-atmosphere stratification and of applying a small positive heat flux at the surface on the flow within the ABL. We consider an ABL which is influenced by both the negative heat flux associated with a capping inversion and the positive heat flux from heating of the surface, to be more realistic than the strictly CN ABL with no surface heat flux. Finally, simulated profiles of wind shear and wind speed are compared to models of Zilitinkevich and Esau (2005) and Gryning et al. (2007).

2 Simulations

A total of 10 simulations (Table 1) are included in this study. The LES code used for the simulations is described in section 2.1 and the setup of the simulations is described in section 2.2. In section 2.3 we examine resolution sensitivity and accuracy of the simulations.

2.1 The NCAR LES code

We use the pseudo-spectral LES code developed at the National Center for Atmospheric Research (NCAR) based on Moeng (1984) and Sullivan and Patton (2011). It solves the filtered momentum equations in a Cartesian coordinate system following the rotation of the Earth:

$$\frac{\partial \overline{u_i}}{\partial t} + \varepsilon_{ijk}\overline{\omega_j}\,\overline{u_k} = -\frac{\partial P^*}{\partial x_i} - \frac{1}{\langle\rho\rangle}\frac{\partial p_0}{\partial x_i} + \varepsilon_{ij3} f \overline{u_j} + g\frac{\overline{\theta'}}{\langle\theta\rangle}\delta_{i3} - \frac{\partial \tau_{ij}}{\partial x_j} \tag{1}$$

where the horizontal directions are denoted by $(x_1, x_2) = (x, y)$ and the vertical by $x_3 = z$. $(u_1, u_2) = (u, v)$ are the horizontal velocity components, $u_3 = w$ denotes deviations from the horizontally-averaged vertical velocity, t is time, $\omega_i = \varepsilon_{ijk}\frac{\partial u_k}{\partial x_j}$ is the vorticity, f is the Coriolis parameter, g is acceleration due to gravity and

$$\tau_{ij} = \overline{u_i u_j} - \overline{u_i}\,\overline{u_j} - \frac{\delta_{ij}}{3}\left(\overline{u_k u_k} - \overline{u_k}\,\overline{u_k}\right) \tag{2}$$

is the deviatoric subfilter stress tensor. Repeated indices imply summation. Overbars indicate filtered (resolved) quantities. The flow variables are in general divided into mean and fluctuating parts, e.g. $u = \langle u \rangle + u'$, where the angular brackets $\langle\rangle$ denote a horizontal average. The pressure $p = p_0 + \langle p \rangle + p'$ furthermore includes the base state pressure p_0, which is constant in height but varies linearly in x and y.

$$P^* = \frac{\overline{p'}}{\langle \rho \rangle} + \frac{1}{3}\left(\overline{u_k u_k} - \overline{u_k}\,\overline{u_k}\right) + \frac{1}{2}\overline{u_i}\,\overline{u_i} \tag{3}$$

is a modified pressure accounting for the normal subfilter stress components and the rotational form of the advection terms (Moeng, 1984). The mean state is assumed to be in hydrostatic balance

$$-\frac{1}{\langle \rho \rangle}\frac{\partial \langle p \rangle}{\partial z} = g \tag{4}$$

with the mean density $\langle \rho \rangle$ being constant.

The horizontal gradient of the base-state pressure $\left(\frac{\partial p_0}{\partial x}, \frac{\partial p_0}{\partial y}\right)$ is applied as an external forcing, and P^* is found by solving the Poisson equation formed by taking the divergence of Eq. 1 and applying continuity, i.e. $\frac{\partial u_i}{\partial x_i} = 0$.

The subfilter stresses are determined using the model of Sullivan et al. (1994) and a wave-cutoff filter (Moeng and Wyngaard, 1988) is applied in the horizontal directions. To avoid aliasing, the filter width is $3/2$ times the grid spacing. The potential temperature θ is treated as a conserved scalar:

$$\frac{\partial \overline{\theta}}{\partial t} + \overline{u_i}\frac{\partial \overline{\theta}}{\partial x_i} = -\frac{\partial \tau_{\theta i}}{\partial x_i} \tag{5}$$

with the subfilter fluxes $\tau_{\theta i}$ determined as originally described by Moeng (1984).

At the top of the domain we use the radiative boundary condition of Klemp and Durran (1983). A third-order Runge-Kutta scheme is used for integration in time.

2.2 Setup of simulations

All simulations are initialized with the potential temperature increasing linearly with height throughout the domain from 290 K at the surface ($z = 0$), and with a wind speed of $10\,\mathrm{m\,s^{-1}}$ at all heights, i.e. $\mathbf{u} = (u, v) = (10, 0)\,\mathrm{m\,s^{-1}}$. The vertical velocity is initially set to zero at all grid points.

A constant horizontal pressure gradient across the domain drives the flow; it is specified in terms of $\mathbf{G} = (U_g, V_g) = \left(-\frac{1}{f\langle\rho\rangle}\frac{\partial p_0}{\partial y}, \frac{1}{f\langle\rho\rangle}\frac{\partial p_0}{\partial x}\right) = (10, 0)\,\mathrm{m\,s^{-1}}$. Small random divergence-free perturbations are added to the initial fields of u, v and θ near the surface (for $z < 50$ m) to initialize turbulence (as in Otte and Wyngaard, 2001). We use a domain extending 3, 3 and 2 km in the x-, y- and z-direction with 256 grid points in all three directions. The surface roughness length z_0 is set to 0.01 m, the mean state density to 1 kg $\mathrm{m^{-3}}$ and the Coriolis parameter to $10^{-4}\,\mathrm{s^{-1}}$.

The heat flux $\langle w'\theta' \rangle_s$ applied at the bottom surface of the domain and the vertical gradient of the initial temperature profile $\frac{\partial \theta_i}{\partial z}$, i.e. the inversion strength, is varied between

simulations as shown in Table 1. The table also shows the Brunt Vaisala frequency $N = \left(\frac{\partial \theta}{\partial z}\frac{g}{\theta}\right)^{0.5}$ based on mean values from above the ABL. Simulations n_{01} to n_{04} are referred to as neutral cases and n_{05} to n_{10} as near-neutral cases.
All simulations cover 24 hours, except n_{02} which covers 32 hours. Horizontal averages of selected flow parameters are stored at intervals of 500 time steps, which corresponds to approximately 460 seconds.

Table 1: Vertical gradient of the initial temperature profile, applied surface heat flux and free atmosphere Brunt Vaisala frequency of the performed simulations.

	$\frac{\partial \theta_i}{\partial z}$ [K m^{-1}]	$\langle w'\theta' \rangle_s$ [K m s^{-1}]	N [s^{-1}]
n_{01}	0.001	0	0.006
n_{02}	0.003	0	0.010
n_{03}	0.006	0	0.014
n_{04}	0.010	0	0.018
n_{05}	0.003	0.001	0.010
n_{06}	0.003	0.003	0.010
n_{07}	0.003	0.005	0.010
n_{08}	0.006	0.001	0.014
n_{09}	0.006	0.005	0.014
n_{10}	0.006	0.007	0.014

2.3 Resolution sensitivity and accuracy of simulations

A measure of the accuracy of an LES is the ratio between the resolved and subfilter stresses,

$$R = \left(\frac{\langle u'w' \rangle_{res}^2 + \langle v'w' \rangle_{res}^2}{\langle u'w' \rangle_{sub}^2 + \langle v'w' \rangle_{sub}^2} \right)^{1/2}. \quad (6)$$

Brasseur and Wei (2010) found that R should be of order 1 or more at the lowest grid level for accurate simulation of the ABL flow. R-values from simulation n_{02} are shown in Fig. 1.
At the first grid level R remains around 0.6 throughout the simulation. In the stably stratified entrainment zone marking the top of the ABL, R-values as low as 1 occur, but mainly in the first part of the simulation. The threshold for R suggested by Brasseur and Wei (2010) is based on a study of when spurious "overshoot" in the non-dimensional wind shear $\phi = \frac{\partial |\mathbf{u}|}{\partial z}\frac{z\kappa}{u_{*0}}$ near the surface disappears; κ is the von Karman constant and u_{*0} is the surface friction velocity. This overshoot-problem is to a large extent solved by using the subfilter-scale model of Sullivan et al. (1994) instead of e.g. the model of Deardorff (1980) and Moeng (1984). Some overshoot is, however, still observed. Simulation n_{02}

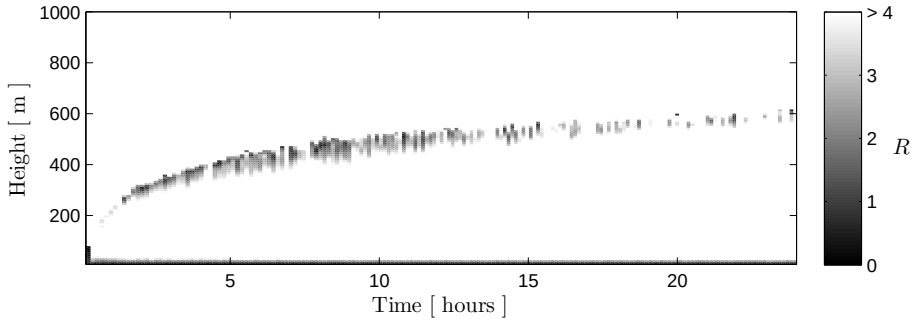

Figure 1: Ratio between the resolved and subfilter stresses from simulation n_{02}.

with 256^3 grid points is repeated with 64^3, 128^3 and 512^3 grid points, and averaging over the period between 23 and 24 hours of simulation time we find the maximum values of ϕ in the lowest 10% of the ABL to be 1.17, 1.14, 1.09 and 1.09 in order of increasing number of grid points. Thus, in this respect the 256^3 grid points used in n_{02} are sufficient to obtain a resolution-independent solution.

Regarding accurate simulation of the entrainment zone, Sullivan and Patton (2011) point to the growth rate of the ABL as a critical parameter for evaluation of grid-dependence. They show that after an initial adjustment period, the growth rate of the convective ABL decreases with finer resolution. The ABL growth rates of our 64^3-, 128^3-, 256^3- and 512^3-simulations averaged over the period between 8 and 24 hours of simulation time are 2.2, 2.2, 1.9 and 2.0 $\mathrm{mm\,s^{-1}}$. We take the small difference between the growth rates of the 256^3-simulation and the 512^3-simulation as an indication that 256^3 grid points are also sufficient in this respect. During the first approximately 8 hours where the mixed layer and capping inversion are still developing (see section 3.2), we find the growth rate to be more sensitive to changes in resolution.

Based on the sensitivity analysis presented here regarding the resolution of simulation n_{02}, we assume that 256^3 grid points provide adequate resolution in all the performed simulations. Otte and Wyngaard (2001) use the ratio between the vertical resolution Δz and the buoyancy length scale $l_b = 1.69 \langle w'w' \rangle^{0.5} \left(\frac{g}{\theta} \frac{\partial \theta}{\partial z} \right)^{-0.5}$ in the entrainment zone as a measure of how well this layer is resolved. They discard simulations where the ratio $\Delta z / l_b$ is close to one or above. In all simulations of the present study l_b at the top of the ABL is at least two times the vertical resolution. Finally, we find the influence of the domain size on the simulated flow to be small. This was examined by repeating simulation n_{07} in a domain twice as big, i.e. in a domain of 6x6x4 $\mathrm{km^3}$.

3 Spin-up and development of simulated ABL

3.1 Mean momentum and turbulent kinetic energy

The simulated flow is horizontally homogeneous, and the mean momentum equations can be written as:

$$\frac{\partial \langle u \rangle}{\partial t} = f(\langle v \rangle - V_g) - \frac{\partial \langle u'w' \rangle}{\partial z} \tag{7}$$

$$\frac{\partial \langle v \rangle}{\partial t} = f(U_g - \langle u \rangle) - \frac{\partial \langle v'w' \rangle}{\partial z}. \tag{8}$$

Thus, the acceleration of the mean flow depends on a balance between the Coriolis force, the pressure gradient, and the vertical gradient of the turbulent stresses.
Figure 2 shows the terms of equations 7 and 8 as they develop in simulation n_{02} with no surface heat flux and $N = 0.01\,\mathrm{s}^{-1}$. The values shown are one hour running means of horizontally averaged quantities.

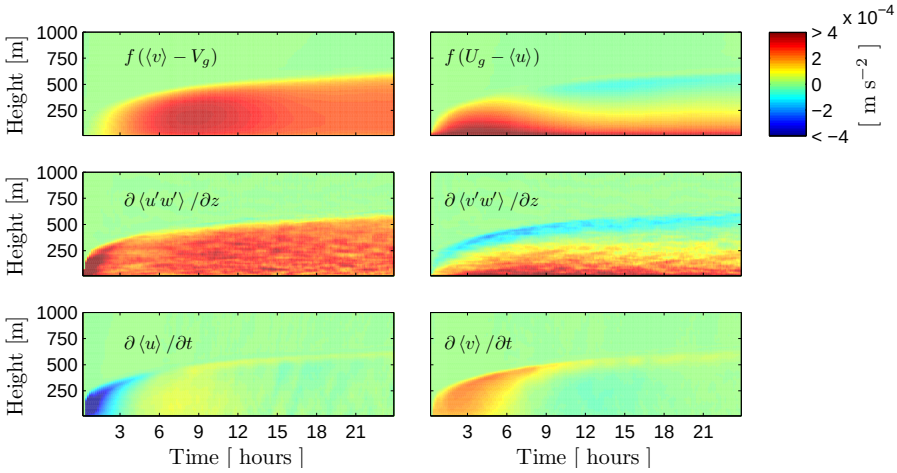

Figure 2: Terms of the mean momentum equations (7 and 8) from simulation n_{02}.

A no-slip boundary condition with the stresses determined from the specified roughness length (Moeng, 1984) is applied at the surface, and in the very early stages of the simulation, the $\langle u \rangle$-component has to decrease from the initial value of $10\,\mathrm{m\,s}^{-1}$. The resulting vertical shear leads to high values of $\frac{\partial \langle u'w' \rangle}{\partial z}$, and since $f\langle v \rangle$ is close to zero in the beginning of the simulation, $\frac{\partial \langle u \rangle}{\partial t}$ stays negative for approximately the first four hours of simulation time.
As $\langle u \rangle$ decreases, $f(U_g - \langle u \rangle)$ quickly exceeds $\frac{\partial \langle v'w' \rangle}{\partial z}$ and $\langle v \rangle$ starts to increase.
However, $\frac{\partial \langle v'w' \rangle}{\partial z}$ develops more gradually than $\frac{\partial \langle u'w' \rangle}{\partial z}$ and is generally of smaller amplitude, except in the lowest 10% of the ABL. The ABL height h is defined as the height

where the horizontally averaged stress $u_*^2 = \left(\langle u'w'\rangle^2 + \langle v'w'\rangle^2\right)^{1/2}$ is reduced to 5% of the surface value u_{*0}^2.

After four hours both stress divergence terms reach a nearly steady state where $\frac{\partial\langle u'w'\rangle}{\partial z}$ is almost constant with height up to $z/h \simeq 0.7$ (above which it decreases towards zero), and $\frac{\partial\langle v'w'\rangle}{\partial z}$ decreases with height from a positive value near the surface to a negative value just below the top of the ABL. At this point in time the decrease in $\langle u\rangle$ stops but $\langle v\rangle$ continues to increase.

After approximately 6 hours $f\langle v\rangle$ exceeds $\frac{\partial\langle u'w'\rangle}{\partial z}$ at all heights and $\langle u\rangle$ starts to increase throughout the boundary layer. In a layer just below the top of the ABL it exceeds U_g and the wind speed becomes super-geostrophic, i.e. $|\mathbf{u}| > |\mathbf{G}|$.

The increase of $\langle u\rangle$ brings $f(U_g - \langle u\rangle)$ closer to $\frac{\partial\langle v'w'\rangle}{\partial z}$ which stops and reverse the growth of $\langle v\rangle$ in most of the ABL.

After 16-17 hours the whole system reaches a seemingly steady balance including the super-geostrophic jet with its peak at $z/h \simeq 1$. The ABL continues to grow but at a slow rate. The observed equilibration period fits well with the length of the inertial period $\frac{2\pi}{f} \simeq 17$ hours suggested by Mason and Thomson (1987) as the time needed to reach a statistically steady state.

Figure 3 is similar to Fig. 2, but shows results from simulation n_{07} with a surface heat flux of $0.005\,\mathrm{K\,m\,s^{-1}}$.

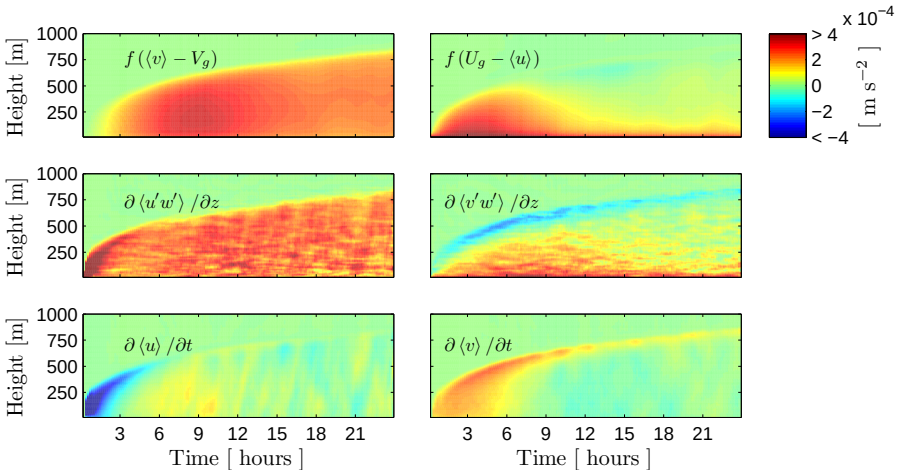

Figure 3: Terms of the mean momentum equations (7 and 8) from simulation n_{07}.

The near-neutral boundary layer grows faster than the neutral one, and especially the terms of Eq. 8 develop differently. In the bottom half of the ABL, the values of $\langle u\rangle$ are generally higher in the near-neutral case than in the neutral case, and vice versa in the top half. This results in a near-neutral wind speed profile, which is almost constant with height for $0.3 < z/h < 0.7$ after 17 hours of simulation time. A super-geostrophic jet also appears in

this case, but it dissolves towards the end of the simulation.
In Fig. 4 we compare the terms of the TKE-equation (9) extracted from simulations n_{02} and n_{07}.

$$\frac{1}{2}\frac{\langle \partial u_i' u_i' \rangle}{\partial t} =$$

$$\underbrace{-\frac{\langle u_j \rangle}{2}\frac{\partial \langle u_i' u_i' \rangle}{\partial x_j}}_{\text{A}} \underbrace{-\langle u_i' u_j' \rangle \frac{\partial \langle u_i \rangle}{\partial x_j}}_{\text{SP}} \underbrace{-\frac{1}{2}\frac{\partial \left\langle u_i' u_i' u_j' \right\rangle}{\partial x_j} - \frac{1}{\langle \rho \rangle}\frac{\partial \langle p' u_i' \rangle}{\partial x_i}}_{\text{T}} \underbrace{+\frac{g}{\langle \theta \rangle}\langle \theta' u_i' \rangle \delta_{3i}}_{\text{BP}} \underbrace{-\varepsilon}_{\text{D}} . \quad (9)$$

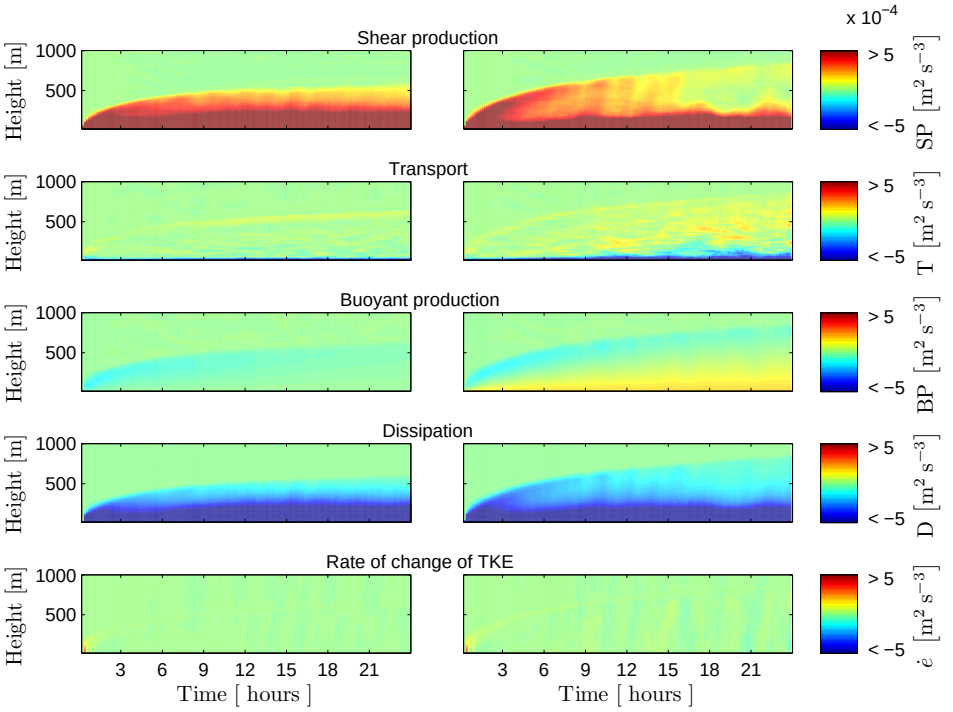

Figure 4: Terms of the TKE equation (9) from simulations n_{02} (left column) and n_{07} (right column).

Under horizontal homogeneity the mean advection term (the first term on the right-hand side) is zero. The second term is shear production (SP). Term three and four (turbulent transport and pressure transport) are combined into one transport term (T). Term five is buoyant production (BP) and term six represents viscous dissipation (D).
In both simulations, shear production and dissipation are the dominant terms in the lower part of the ABL; near the surface, however, turbulent and pressure transport also become

significant. In the upper part of the ABL buoyant destruction becomes important, especially in the beginning of the simulations where the ABL grows rapidly. The shear production remains almost constant with time in the neutral simulation, but is clearly diminished in the middle and upper parts of the near-neutral ABL as the jet is dissolved. It is to some extent replaced by turbulent- and pressure-transport. This change in the TKE budget underlines that an adjustment period of at least 16 hours is also necessary in the near-neutral case to get steady-state results.

3.2 Growth of the ABL

The stably stratified air above the ABL inhibits its growth through buoyant destruction of TKE. The initial stratification of the simulations presented here is, however, relatively weak compared to the capping inversion developing later in the simulations (see Fig. 5), and the boundary layer grows rapidly during early spin-up. Figure 5 shows the vertical gradient of potential temperature as it changes with time and height in simulations n_{02} and n_{07}. Within most of the ABL, it is close to zero due to turbulent mixing, and an interfacial layer (capping inversion) of strong stable stratification forms between this mixed layer and the free atmosphere.

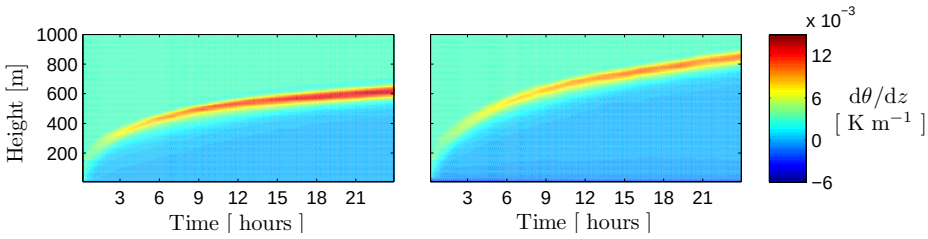

Figure 5: The vertical gradient of potential temperature as function of time and height in simulations n_{02} (left) and n_{07} (right).

The growth rate of the ABL decreases with time, partly as a consequence of the increasing strength of the capping inversion. Growth rates from simulations n_{01}, n_{02}, n_{03}, n_{04} and n_{07} are shown in Fig. 6 as functions of simulation time.
Initially the growth rate decreases with higher N, but after approximately 8 hours it reaches a constant level which seems to be nearly independent of the inversion strength, but rather tied to $\langle w'\theta' \rangle_s$. However, as shown in section 3.1, the flow does not become steady until after approximately 17 hours. The growth rates averaged over the period between 8 and 24 hours of simulation n_{01}, n_{02}, n_{03}, n_{04} and n_{07} with N-values of 0.006, 0.010 0.014, 0.018 and 0.01 s^{-1} are 1.8, 1.9, 1.2, 1.7 and 4.0 $mm\,s^{-1}$.
Establishment of the mixed layer and the capping inversion are central parts of the "spin-up" process in the simulations presented here. Other studies, e.g. Moeng and Sullivan (1994), include these features in the initial temperature field. However, we find that doing so has very little effect on the time needed for the momentum terms to reach a steady balance as well as on the shape of the steady-state wind profile. Only the growth rate of

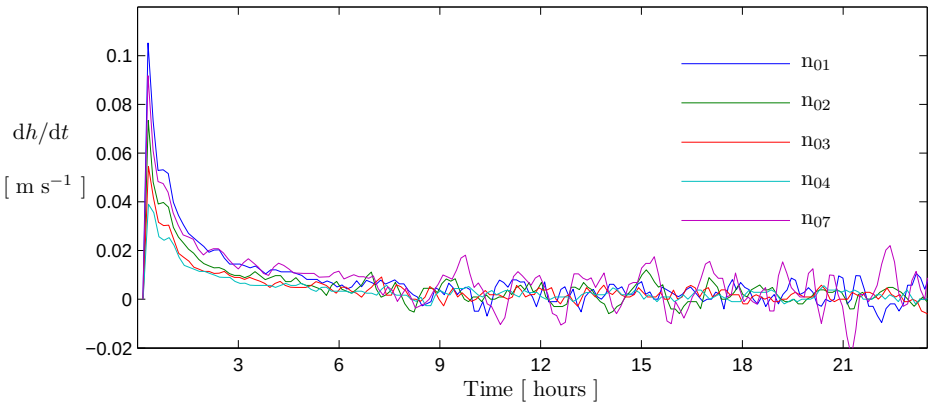

Figure 6: ABL growth rates from simulations n_{01}, n_{02}, n_{03}, n_{04} and n_{07}.

the ABL reaches a quasi-steady level earlier; after approximately two hours of simulation time. This was tested by repeating simulation n_{02} with an initial temperature profile corresponding to the 13-hour profile of the original simulation.
Based on the formula of Rossby and Montgomery (1935), Zilitinkevich et al. (2012) suggest the following expression for the equilibrium height of the conventionally neutral ABL (i.e. the ABL with $\langle w'\theta' \rangle_s = 0$ and $N > 0$):

$$h_e = C_h \frac{u_{*0}}{f} \tag{10}$$

where

$$C_h = C_{CN} \left(\frac{f}{N} \right)^{1/2} \tag{11}$$

They determine the value of $C_{CN} = 1.36$ based on LES results. Values of C_h from Eq. 11 are shown in Fig. 7 together with values based on our LES results; both axes are logarithmic. The agreement is generally good, but the continuous growth of the ABL makes C_h time-dependent. This is illustrated by the difference between the grey and black markers representing values based on results from the periods between 16 and 17 hours and 23 and 24 hours of simulation time. Based on these two sets of data points, we find C_{CN}-values of 1.4 and 1.5.

4 Steady state profiles

In this sections we presents result from the period between 23 and 24 hours of simulation time, when the flow of both the neutral and near-neutral simulations has reached a quasi-steady state.
Figure 8 shows wind profiles from neutral simulations with increasing values of N (n_{01},

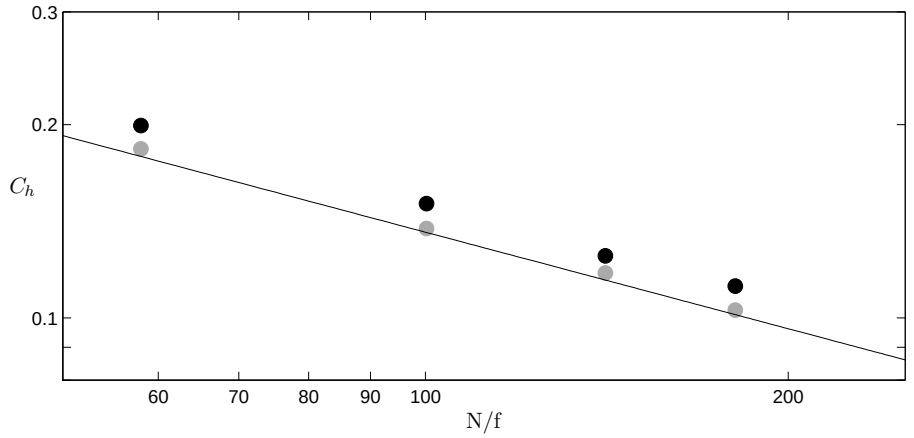

Figure 7: Values of C_h from Eq. 11 using C_{CN} from Zilitinkevich et al. (2012) (line) and from simulations n_{01}, n_{02}, n_{03} and n_{04} between 16 and 17 hours (grey markers) and 23 and 24 hours (black markers) of simulation time.

n_{02}, n_{03}, n_{04}) and from simulations with increasing surface heat flux but with the same values of N (n_{02}, n_{05}, n_{06}, n_{07}). Characteristic for all four neutral profiles in Fig. 8(a) is the wind speed maximum of approximately $1.07|\mathbf{G}|$ at $z/h \simeq 1$. Below the peak of this super-geostrophic jet, there is a general tendency of the wind speed to decrease as N is increased, and of the wind shear $\frac{\partial|\mathbf{u}|}{\partial z}$ to increase, most significantly in the middle part of the ABL. Increasing N also leads to more negative values of the entrainment heat flux $\langle w'\theta'\rangle_i$ which we define as the minimum heat flux observed just below the top of the boundary layer (see Fig. 9).

Figure 8(b) shows the effect on the wind profile of increasing the surface heat flux from 0 in simulation n_{02} to 0.001, 0.003 and 0.005 $\mathrm{K\,m\,s^{-1}}$ in simulations n_{05}, n_{06} and n_{07} respectively; the magnitude of the jet and the wind shear below is reduced, except near the surface where the shear increases. With a surface flux of 0.005 $\mathrm{K\,m\,s^{-1}}$, the wind speed maximum is reduced to $1.01|\mathbf{G}|$.

Defining the super-geostrophic jet as the height interval from z_{bottom} to z_{top} in which $|\mathbf{u}| > |\mathbf{G}|$, we determine its size relative to the boundary-layer height and $|\mathbf{G}|$ as:

$$\frac{1}{h}\int_{z_{\mathrm{bottom}}}^{z_{\mathrm{top}}} \frac{|\mathbf{u}|-|\mathbf{G}|}{|\mathbf{G}|}\mathrm{d}z\,. \tag{12}$$

Increasing either $\langle w'\theta'\rangle_{\mathrm{s}}$ or N and thereby $-\langle w'\theta'\rangle_i$, will decrease the size of the jet. In Fig. 10, the jet size is plotted against the absolute heat flux integrated across the ABL:

$$\int_0^h |\langle w'\theta'\rangle|\,\mathrm{d}z\,. \tag{13}$$

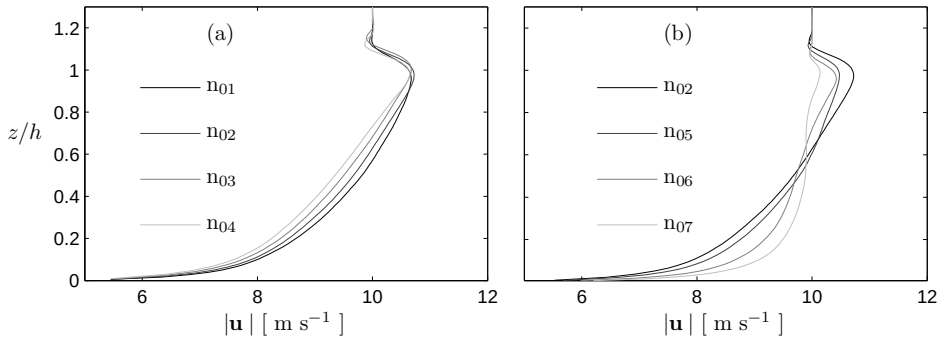

Figure 8: Wind profiles showing N-dependence (a) and surface heat flux dependence (b) after 23 hours of simulation time. N and $\langle w'\theta' \rangle_s$ increase with lighter colors.

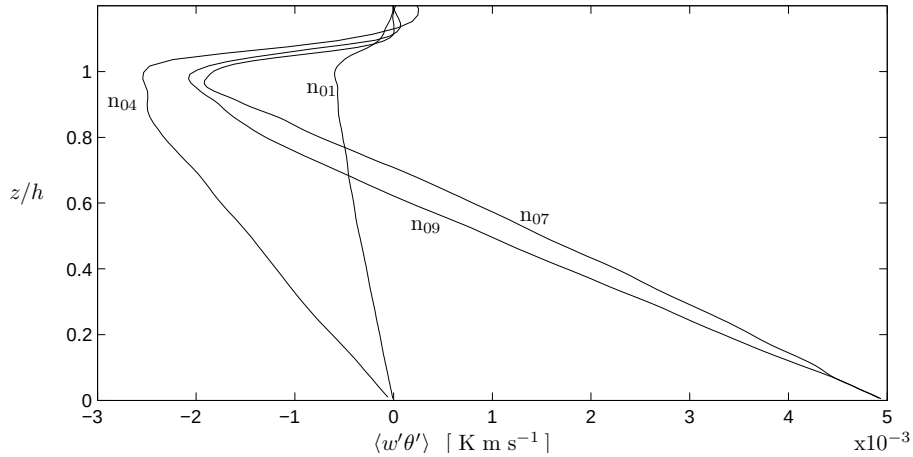

Figure 9: Profiles of kinematic heat flux averaged between 23 and 24 hours of simulation time.

Both for the neutral and near-neutral cases, the jet size decreases almost linearly with increasing integrated heat flux; however a little faster for the neutral cases than for the near-neutral cases.

The profiles in Fig. 9 show that the simulated heat flux between the specified surface value $\langle w'\theta' \rangle_s$ and the minimum value $\langle w'\theta' \rangle_i$ at $z/h \simeq 1$ is approximately a linear function of height which can be easily integrated. Based on integration of the TKE-budget over the daytime mixed layer, Batchvarova and Gryning (1991) suggested the following estimate

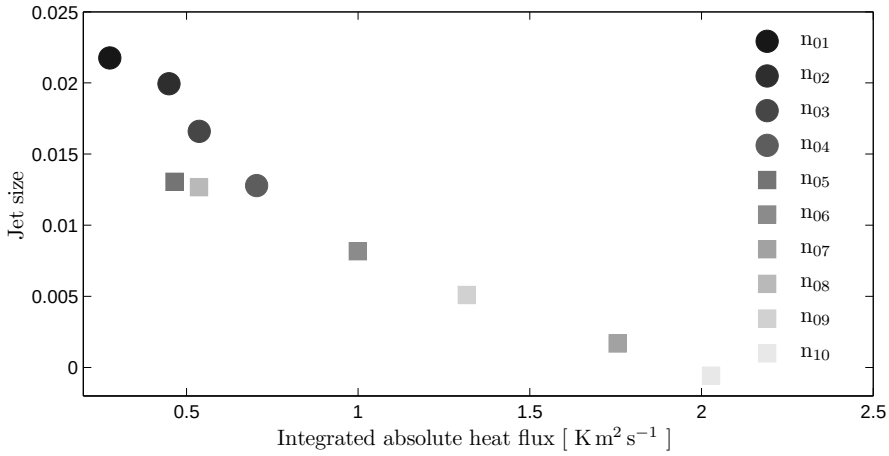

Figure 10: The jet size defined by Eq. 12 as function of the absolute heat flux integrated across the ABL.

of the entrainment heat flux:

$$-\frac{gh_\mathrm{m}}{\theta_\mathrm{m}}\left\langle w'\theta'\right\rangle_i = A\frac{gh_\mathrm{m}}{\theta_\mathrm{m}}\left\langle w'\theta'\right\rangle_\mathrm{s} + Bu_{*0}^3 - Cu_{*0}^2\frac{\mathrm{d}h_\mathrm{m}}{\mathrm{d}t} \tag{14}$$

where h_m is the height of the mixed layer, θ_m is the potential temperature of the mixed layer, and A, B and C are parametrization constants. We use the height of $\langle w'\theta'\rangle_i$ as a measure of h_m; it is typically a little smaller than h. Batchvarova and Gryning (1991) use $A = 0.2$, $B = 2.5$ and $C = 8$. Based on least-squares fitting to our LES result we find $A = 0.2$, $B = 0.4$ and $C = 3$. Estimates of $\langle w'\theta'\rangle_i$ from Eq. 14 using these values are compared to entrainment fluxes extracted directly from our simulations in Fig. 11. The marker size is proportional to the inversion strength (N) of each simulation. The estimates from Eq. 14 lie between -17 % and 9 % of the simulated values.
Due to the slow growth of the steady-state ABL, C can be set to zero without significant deterioration of these relative errors. With the used parametrization constants, the C-term is in most cases about an order of magnitude smaller than the remaining terms of Eq. 14. It represents the rate of change of TKE at the top of the mixed layer, which is indeed small as seen in Fig. 4.

5 Comparison with analytical models of the wind profile

The wind profile of the atmospheric surface layer is generally well described by Monin-Obukhov similarity theory, and in truly or conventionally neutral conditions by the logarithmic 'law-of-the-wall' profile. Recently Zilitinkevich and Esau (2005), Gryning et al. (2007) and Kelly and Gryning (2010) have extended the theory to make it valid above the surface layer as well.

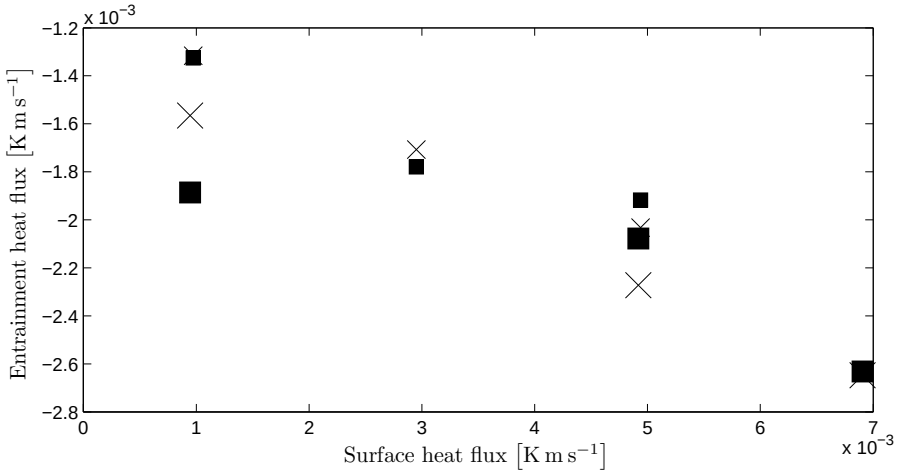

Figure 11: The entraiment flux predicted by Eq. 14 (crosses) compared to the actual entrainment fluxes (squares) from simulations n_{05}, n_{06}, n_{07}, n_{08}, n_{09} and n_{10}.

Zilitinkevich and Esau (2005) include the effects of the capping inversion and the rotation of the Earth through the combined turbulent length scale L_M:

$$\frac{1}{L_M} = \left(\left(\frac{1}{L}\right)^2 + \left(\frac{C_{NM}}{L_N}\right)^2 + \left(\frac{C_{fM}}{L_f}\right)^2 \right)^{1/2}, \tag{15}$$

where

$$L = -\frac{u_*^3}{(g/T)\langle w'\theta' \rangle},\ L_N = \frac{u_{*0}}{N},\ L_f = \frac{u_{*0}}{|f|}. \tag{16}$$

T is the temperature and C_{NM} and C_{fM} are dimensionless constants with suggested values of 0.1 and 1. This leads to the following formulation of the wind shear valid for stable, truly neutral and conventionally neutral ABLs:

$$\frac{\partial |\mathbf{u}|}{\partial z} = \frac{u_*}{\kappa z}\left(1 + C_u \frac{z}{L_M}\right), \tag{17}$$

where C_u is dimensionless constant with a suggested value of 2.5.
Gryning et al. (2007) use a length scale l modelled by inverse summation of L_{SL}, L_{MBL} and L_{UBL} representing the length scales in the surface layer, the middle part of the ABL and the upper part of the ABL:

$$\frac{1}{l} = \frac{1}{L_{SL}} + \frac{1}{L_{MBL}} + \frac{S}{L_{UBL}}. \tag{18}$$

Following Kelly and Gryning (2010) we have introduced the baroclinic shear $S = \kappa h \frac{\mathrm{d}|\mathbf{G}|/\mathrm{d}z}{u_{*0}}$ (note that the definition of S is misprinted in Kelly and Gryning (2010)). In the original

formulation of Eq. 18, Gryning et al. (2007) used $S = 1$. In all the large-eddy simulations presented here $S = 0$.
In neutral conditions $L_{SL} = z$ and $L_{UBL} = h - z$, and the wind shear is given by:

$$\frac{\partial |\mathbf{u}|}{\partial z} = \frac{u_{*0}}{\kappa}\left(1 - \frac{z}{h}\right)\left(\frac{1}{z} + \frac{1}{L_{MBL}} + \frac{S}{h-z}\right). \tag{19}$$

Integration of Eq. 19 leads to the wind profile formulation:

$$|\mathbf{u}| = \frac{u_{*0}}{\kappa}\left[\ln\left(\frac{z}{z_0}\right) + \frac{z}{L_{MBL}}\left(1 - \frac{z}{2h}\right) - \frac{z}{h}(1 - S)\right]. \tag{20}$$

The length scale of the middle ABL, L_{MBL}, is determined to make the wind speed at the top of ABL match the geostrophic wind speed $|\mathbf{G}|$.
In Fig. 12, we compare wind shear determined through equations 17 and 19, i.e. the models of Zilitinkevich and Esau (2005) and Gryning et al. (2007), to the wind shear of simulations n_{01}, n_{02}, n_{03} and n_{04} averaged between 23 and 24 hours of simulation time. The input parameters to the models are taken from the LESs. In Eq. 17 we use $\kappa = 0.47$ as suggested by Zilitinkevich and Esau (2005), and we show results based on both surface scaling ($L_M = L_N/C_{NM}$ for the CN ABL) and local scaling, i.e. with L_M being a function of the local stability parameter $L(z)$ (Eq. 15). We find the description of the model to be a little unclear in terms of which type of scaling to use in the CN ABL. In Eq. 19 we use $\kappa = 0.4$, and we show results with $S = 1$ and $S = 0$.

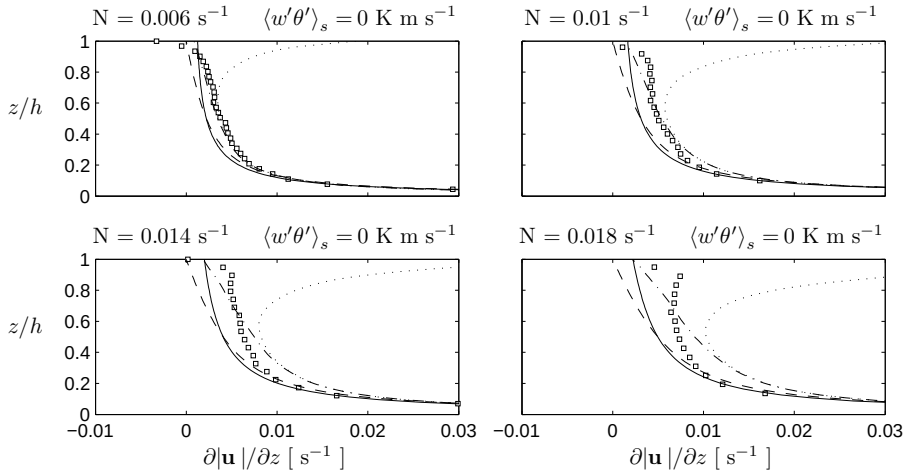

Figure 12: Wind shear from LES (n_{01}, n_{02}, n_{03} and n_{04}) and analytical models. Markers represent LES, dotted and dash-dotted lines represent Eq. 17 with $L_M = f(L(z), L_N, L_f)$ and $L_M = L_N/C_{NM}$ respectively, and dashed and solid lines represent Eq. 19 with $S = 0$ and $S = 1$ respectively.

The best agreement between the two models and the LES results is seen in the case of

$N = 0.006$ s^{-1}, where Eq. 17 with $L_M = L_N/C_{NM}$ agrees very well up to $z/h \simeq 0.9$; applying local scaling, i.e. $L_M = f(L(z), L_N, L_f)$, leads to an overestimation of the shear for $z/h > 0.7$. Equation 19 with both $S = 0$ and $S = 1$ agrees fairly well with the LES up to $z/h \simeq 0.9$. Neither of the models predicts the negative shear associated with the super-geostrophic jet.

As N is increased the agreement deteriorates, and Eq. 17 overestimates the shear above the surface layer; in the case of $N = 0.018$ s^{-1} up to $z/h \simeq 0.6$ with $L_M = L_N/C_{NM}$ and throughout the ABL with $L_M = f(L(z), L_N, L_f)$. Equation 19 agrees quite well with the simulated shear up to $z/h \simeq 0.3$ but underestimates it above. Using $S = 1$ instead of $S = 0$ leads to better agreement in the upper half of the ABL.

The wind speed profile model developed by Gryning et al. (2007), i.e. Eq. 20, is compared to wind speed profiles of simulations n_{01}, n_{04}, n_{07} and n_{09} in Fig. 13. The Obukhov length $L_s = -\frac{u_{*0}^3}{\kappa(g/T)\langle w'\theta'\rangle_s}$ of the two near-neutral simulations (n_{07} and n_{09}) is -1088 and -1039 m. Hence, they fall within the "neutral" category of the stability classification suggested by Gryning et al. (2007).

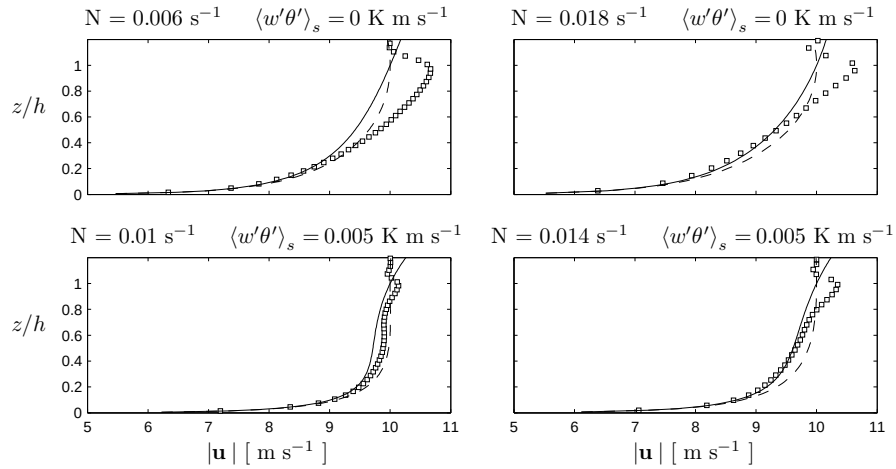

Figure 13: Wind speed profiles from simulation n_{01}, n_{04}, n_{07} and n_{09} (markers) and from Eq. 20 with $S = 0$ (dashed lines) and $S = 1$ (solid lines).

In the case of zero surface heat flux and $N = 0.006$ s^{-1}, the agreement is good up to $z/h \simeq 0.4$ when using $S = 0$ and up to $z/h \simeq 0.3$ when using $S = 1$. Above these heights the model underestimates the wind speed, especially for $z/h > 0.5$ where the wind speed is super-geostrophic. Increasing N to 0.018 s^{-1} makes the super-geostrophic jet more narrow, and there is fair agreement between Eq. 20 and the LES results up to $z/h \simeq 0.6$. The best agreement between the model and the simulated wind speed is in the near-neutral case with N =0.01 s^{-1} and $\langle w'\theta'\rangle_s = 0.005$ K m s^{-1}, where the simulated profile only has a very small jet, and the wind speed is nearly constant with height in the upper half of the ABL. The theoretical model captures this quite well, especially with $S = 0$ which

corresponds to the actual baroclinic shear of the LES. We do, however, note a closer resemblance between the shape of the simulated profile and that of the theoretical profile near the top of the ABL when using $S = 1$ rather than $S = 0$. Furthermore, with N =0.014 s^{-1} and $\langle w'\theta' \rangle_s = 0.005$, the best agreement is obtained with $S = 1$.

6 Concluding remarks

The LES results presented in this study show that the time required for a simulation of the neutral or near-neutral ABL to reach steady-state appears to depend on which parameter is examined. While the growth rate of both types of ABLs reaches a constant level after 8 hours, the terms of the mean momentum equations do not reach a steady balance before 16 hours of simulation time corresponding to the period of the inertial oscillation. We furthermore note that the general shape of the profiles of stress divergence $\left(\frac{\partial \langle u'w' \rangle}{\partial z} \text{ and } \frac{\partial \langle v'w' \rangle}{\partial z} \right)$ in the neutral ABL change little after 4 hours of simulation time.

During each of the performed simulations a jet of super-geostrophic wind speed develops close to the top of the ABL; typically in a period around 9 hours of simulation time, where the transverse component of the wind (v) multiplied by the Coriolis parameter continuously exceeds the divergence of the longitudinal stress just below the ABL top.

In the neutral cases, the jet remains throughout the rest of the simulation period while in the near-neutral cases, the heat flux applied at the surface diminish the size of the jet. With $N = 0.01$ s^{-1} which is a typical value in the free atmosphere, we find that a surface heat flux of only 0.005 K m s^{-1} is enough to obtain a steady-state wind profile with nearly no jet.

Furthermore, we find that increasing the temperature gradient above the ABL and thereby increasing the downward heat flux just below the top of the ABL, decreases the width of the jet.

A semi-empirical relationship is found between the integrated relative jet size, and the absolute heat flux integrated across the ABL. Moreover, from the near-neutral simulations we find that the integrated shear production of TKE approximated by the B-term in Eq. 14 can be described as a linear combination of the entrainment and surface heat fluxes. However, the value we find for B (0.4) is relatively small compared to what is found in earlier studies; e.g. Batchvarova and Gryning (1991) use $B = 2.5$ and Moeng and Sullivan (1994) find $B = 1$ based on LES.

The difference between our results and the results of Moeng and Sullivan (1994) is due to different inversion strengths. While Moeng and Sullivan (1994) used an initial temperature profile including a mixed layer capped by a strong inversion of approximately 8 K over 60 m, we simply specify a constant lapse rate throughout the computational domain. We find that an initial lapse rate of 0.003 K m^{-1} leads to a maximum inversion strength corresponding to just 1 K per 60 m. It is, however, not clear how much the initial capping inversion of the Moeng and Sullivan (1994) simulation weakens during the simulation period.

Simulated profiles of steady-state wind shear and wind speed are compared to theoretical models of Zilitinkevich and Esau (2005) and Gryning et al. (2007). Regarding the shear,

the best agreement between these models and LES is found in cases with low values of N. The model of Zilitinkevich and Esau (2005) is based on the combined length scale L_M, and in the cases presented here we find that applying surface scaling rather than local scaling when determining L_M, provides the best agreement with LES. The model of Gryning et al. (2007) does not include N explicitly but takes into account the boundary-layer height. It generally agrees well with the simulated shear in the lower part of the ABL but underestimates the shear in upper part in simulations with no or very little surface heat flux. This can to some extent be mitigated by applying a dimensionless baroclinic shear of $S = 1$ instead of the actual value of $S = 0$ used in the simulations. In near-neutral simulations with sufficient surface heat flux to dissolve the jet and not too high values of N, using $S = 0$ leads to good agreement with the simulated wind speed throughout the ABL.
As mentioned in the introduction, not much is known from field experiments about the flow in the upper part of the idealized ABL studied here. It does, however, seem unlikely that the simulated jet is a common phenomenon in the real atmosphere, where the conditions typically are near-neutral rather than neutral, and more unsteady than in the simulations presented here; both in terms of heat fluxes and the large scale pressure forcing (Pedersen et al., 2013). Over the ocean and in the high Arctic (Batchvarova et al., 2013), however, the absence of strong influence from the diurnal cycle (Zilitinkevich et al., 2012) could potentially allow a jet to develop in neutral or near-neutral conditions.
The resolution of the performed simulations is 12 m in the horizontal directions and 8 m in the vertical. At this resolution we find the ratio between resolved and subfilter stresses to be sufficiently high for accurate simulation of the ABL flow (Brasseur and Wei, 2010), and the growth rate of the ABL as well as the shape of the steady-state wind profile to be nearly independent of the resolution. We also note that Abkar and Porté-Agel (2013) recently obtained wind profiles similar to those presented here using an LES code employing the more advanced scale-dependent Lagrangian dynamic model of Stoll and Porté-Agel (2006) for computation of the subfilter fluxes.
Our simulations confirm that the height of the steady-state neutral ABL is proportional to u_{*0}/f with the constant of proportionality C_h depending on N as suggested by Zilitinkevich et al. (2012). We do, however, find that simulated ABL continues to grow throughout the 24-hour simulation period (32 hours in simulation n_{02}), which makes C_h a function of time as well as of N.

Acknowledgements

The study was supported by the Danish Council for Strategic Research, project number 2104-08-0025 named “Tall Wind”. We would like to thank Branko Kosović for valuable cooperation.

References

Abkar, M. and Porté-Agel, F. (2013). The Effect of Free-Atmosphere Stratification on Boundary-Layer Flow and Power Output from Very Large Wind Farms. *Energies*,

6:2338–2361.

Andren, A., Brown, A. R., Graf, J., Mason, P. J., Moeng, C.-H., Nieuwstadt, F. T. M., and Schumann, U. (1994). Large-eddy simulation of a neutrally stratified boundary layer: A comparison of four computer codes. *Quart. J. Roy. Meteor. Soc.*, 120:1457–1484.

Basu, S., Vinuesa, J.-F., and Swift, A. (2008). Dynamic LES Modeling of a Diurnal Cycle. *J. Appl. Meteor. Climatol.*, 47:1156–1174.

Batchvarova, E. and Gryning, S.-E. (1991). Applied model for the growth of the daytime mixed layer. *Bound.-Layer Meteor.*, 56:261–274.

Batchvarova, E., Gryning, S.-E., Skov, H., Sørensen, L. L., Kirova, H., and Münkel, C. (2013). Boundary-layer and air quality study at "Station Nord" in Greenland. In Steyn, D. G. and Mathur, R., editors, *Air pollution modeling and its application*, Dordrect. Springer Science + Business Media B. V. In press.

Brasseur, J. G. and Wei, T. (2010). Designing large-eddy simulation of the turbulent boundary layer to capture law-of-the-wall scaling. *Phys. Fluids*, 22. 021303.

Deardorff, J. W. (1980). Stratocumulus-capped mixed layers derived from a three-dimensional model. *Bound.-Layer Meteor.*, 18:495–527.

Gryning, S.-E., Batchvarova, E., Brümmer, B., Jørgensen, H., and Larsen, S. (2007). On the extension of the wind profile over homogeneous terrain beyond the surface boundary layer. *Bound.-Layer Meteor.*, 124:251–268.

Hess, G. D. (2004). The neutral, barotropic planetary boundary layer, capped by a low-level inversion. *Bound.-Layer Meteor.*, 110:319–355.

Kelly, M. and Gryning, S.-E. (2010). Long-term mean wind profiles based on similarity theory. *Bound.-Layer Meteor.*, 136:377–390.

Klemp, J. B. and Durran, D. R. (1983). An upper boundary condition permitting internal gravity wave radiation in numerical mesoscale models. *Mon. Wea. Rev.*, 111:430–444.

Kosović, B. (1997). Subgrid-scale modelling for the large-eddy simulation of high-Reynolds-number boundary layers. *J. Fluid Mech.*, 336:151–182.

Kumar, V., Svensson, G., Holtslag, A. A. M., Meneveau, C., and Parlange, M. B. (2010). Impact of Surface Flux Formulations and Geostrophic Forcing on Large-Eddy Simulations of Diurnal Atmospheric Boundary Layer Flow. *J. Appl. Meteor. Climatol.*, 49:1496–1516.

Mason, P. J. and Thomson, D. J. (1987). Large-eddy simulations of the neutral-static-stability planetary boundary layer. *Quart. J. Roy. Meteor. Soc.*, 113:413–443.

Mirocha, J., Kirkil, G., Bou-Zeid, E., Chow, F. K., and Kosović, B. (2013). Transition and Equilibration of Neutral Atmospheric Boundary Layer Flow in One-Way Nested Large-Eddy Simulations Using the Weather Research and Forecasting Model. *Mon. Weather Rev.*, 141:918–940.

Moeng, C.-H. (1984). A Large-Eddy-Simulation Model for the Study of Planetary Boundary-Layer Turbulence. *J. Atmos. Sci.*, 41:2052–2062.

Moeng, C.-H. and Sullivan, P. P. (1994). A Comparison of Shear- and Buoyancy-Driven Planetary Boundary Layer Flows. *J. Atmos. Sci.*, 51:999–1022.

Moeng, C.-H. and Wyngaard, J. C. (1988). Spectral analysis of Large-Eddy Simulations of the Convective Boundary Layer. *J. Atmos. Sci.*, 45:3573–3587.

Otte, M. J. and Wyngaard, J. C. (2001). Stably Stratified Interfacial-Layer Turbulence from Large-Eddy Simulation. *J. Atmos. Sci.*, 58:3424–3442.

Pedersen, J. G., Kelly, M., Gryning, S.-E., and Brümmer, B. (2013). The effect of unsteady and baroclinic forcing on predicted wind profiles in Large Eddy Simulations: Two case studies of the daytime atmospheric boundary layer. *Meteorol. Z.* In press.

Rossby, C. G. and Montgomery, R. B. (1935). The layer of frictional influence in wind and ocean currents. *Pap. Phys. Oceanogr. Meteorol.*, 3:1–101.

Stoll, R. and Porté-Agel, F. (2006). Dynamic subgrid-scale models for momentum and scalar fluxes in large-eddy simulations of neutrally stratified atmospheric boundary layers over heterogeneous terrain. *Water Resour. Res.*, 42.

Sullivan, P. P., McWilliams, J. C., and Moeng, C.-H. (1994). A subgrid-scale model for large-eddy simulation of planetary boundary-layer flows. *Bound.-Layer Meteor.*, 71:247–276.

Sullivan, P. P. and Patton, E. G. (2011). The effect of mesh resolution on convective boundary layer statistics and structures generated by large-eddy simulation. *J. Atmos. Sci.*, 68:2395–2415.

Zilitinkevich, S. S. and Esau, I. N. (2005). Resistance and heat-transfer laws for stable and neutral planetary boundary layers: Old theory advanced and re-evaluated. *Quart. J. Roy. Meteor. Soc.*, 131:1863–1982.

Zilitinkevich, S. S., Tyuryakov, S. A., Troitskaya, Y. I., and Mareev, E. A. (2012). Theoretical models of the height of the atmospheric boundary layer and turbulent entrainment at its upper boundary. *Izv. Atmos. Ocean Phys.*, 48:133–142.

This dissertation is submitted in partial fulfilment of the requirements for the degree of Doctor of Philosophy in Engineering at the Technical University of Denmark. The work was done at the Meteorology Section of the Department of Wind Energy and has been part of the Danish Research Council for Strategic Research Project 2104-08-0025 named "Tall wind".

Principal supervisor: Dr. Scient. Sven-Erik Gryning
Co supervisor: Dr. Mark Kelly
Examiners: Professor Søren Larsen (DTU Wind Energy), Professor Anna Owenius Rutgersson (Uppsala University) and Dr. Mark Zagar (Vestas Wind Systems)

DTU Wind Energy
Technical University of Denmark

Risø Campus, 118
Frederiksborgvej 399
DK-4000 Roskilde
http://www.vindenergi.dtu.dk/

ISBN 978-87-92896-70-4